Discussions on Cloud Feedbacks and Model Variability in CMIP6 Models

Mitchell Kay Kelleher

Charlottesville, Virginia

B.S. Meteorology, The University of Oklahoma, 2016

M.S. Environmental Sciences, University of Virginia, 2019

A Dissertation presented to the Graduate Faculty of the University of Virginia in Candidacy for the Degree of Doctor of Philosophy

Department of Environmental Sciences

University of Virginia

April, 2023

Table of Contents

Attribution iii

Abstract 1

Chapter 1: Introduction

1.1: Cloud Radiative Feedbacks 2

1.2: Types of Uncertainty in climate models 8

Chapter 2: Varied midlatitude shortwave cloud radiative responses to Southern Hemisphere circulation shifts

2.1: Introduction 12

2.2: Data and Methods 14

2.2a: Data 14

2.2b: Methods 15

2.3: Results 17

2.4: Summary and Discussion 22

2.5: Supplemental Information 26

Chapter 3: Variability in Projected North American Mean and Extreme Temperature and Precipitation Trends for the 21st Century: Model-to-model Differences vs. Internal Variability

3.1: Introduction 31

3.2: Data and Methods 35

3.3: Variability in 21st Century Mean and Extreme Temperature and Precipitation Trends for North America across CMIP6 Models 39

3.3a: Seasonal Mean Temperature and Precipitation 39

3.3b: Extreme Temperature and Precipitation 44

3.4: Dynamical Drivers of Variability in Mean and Extreme Temperature and Precipitation Trends for North America across CMIP6 Models 52

3.4a: Identifying the dynamical drivers 52

3.4b: Constructing Storylines 56

3.5: Conclusions 62

3.6: Supplemental Information 65

Chapter 4: Changes to the statistical moments of the Seasonal Distribution of Temperature Across North America

4.1: Introduction 79

4.2: Data and Methods 83

4.3: Projected Changes in the Seasonal Temperature Distributions across CMIP6 Models 86

4.4: Conclusions 94

4.5: Supplemental Information 97

Chapter 5: Summary and Conclusions 99

Acknowledgements 101

References 102

Attribution

Chapter 2 was previously published as:

Kelleher, M. K., & Grise, K. M. (2022). Varied midlatitude shortwave cloud radiative responses to Southern Hemisphere circulation shifts. *Atmospheric Science Letters*, *23*(1), e1068. https://doi.org/10.1002/asl.1068

Chapter 3 was previously published as:

Kelleher, M. K., Grise, K. M., & Schmidt, D. F. (2023). Variability in Projected North American Mean and Extreme Temperature and Precipitation Trends for the 21st Century: Model-To-Model Differences Versus Internal Variability. *Earth's Future*, *11*(3), e2022EF003161. https://doi.org/10.1029/2022EF003161

Abstract

While global climate models have improved over recent model generations, large uncertainty still remains that prevents confidence in future projections of climate change. Two such sources of uncertainty that remain include the role of clouds and their radiative feedbacks on climate and the role of internal variability. This dissertation examines selected aspects of these two sources in order to better understand the future projections of the models.

Changes in midlatitude clouds as a result of shifts in general circulation patterns are widely thought to be a potential source of radiative feedbacks onto the climate system. Previous work has suggested that two general circulation shifts anticipated to occur in a warming climate, poleward shifts in the midlatitude jet streams and a poleward expansion of the Hadley circulation, are associated with differing effects on midlatitude clouds. My study on this topic finds that, due to incorrectly placed dynamical features, models do not capture the observed cloud radiative effects for these circulation shifts, even when the observed sensitivities of clouds to dynamics are used in place of the models' sensitivities.

Climate change is expected to alter mean and extreme temperature and precipitation over the twenty-first century. However, regional changes in these fields remain difficult to project. By examining the range of possible trends in North American mean and extreme temperature and precipitation, I constructed storylines of plausible trends in these fields, and find that the majority of variance in the temperature trends is due to model-to-model differences the while precipitation trends vary largely due to internal variability. Furthermore, changes in the statistical moments of the winter temperature distribution are largely related to the degree of Arctic amplification present in the model, while changes in the summer temperature distribution can largely be described by shifts in the mean alone.

Chapter 1: Introduction

Anthropogenic emissions of greenhouse gases (GHGs) since the industrial revolution have acted to change the Earth's climate in ways that affect human lives and property. In an effort to best prepare for these changes, stakeholders have turned to global climate models (GCMs) to get estimates of how climate change will impact their region. These models show that emissions of GHGs not only impact the global temperature, but also impact circulation patterns across Earth, leading to expected regional shifts in clouds, precipitation, and other dynamical aspects of the climate system. However, while GCMs have generally improved over the generations of the Coupled Model Intercomparison Project (CMIP), there still remains large uncertainty within the models that makes projecting future trends in climate variables difficult. Two such aspects of uncertainty within GCMs are cloud radiative feedbacks to increased emissions and the role of internal variability within the climate system.

1.1 Cloud radiative feedbacks

Clouds are an important component of the Earth's planetary energy budget. Clouds act to affect the energy budget of the Earth in two major ways. First, clouds act to reflect incoming shortwave radiation away from the Earth's surface back into space, acting as a cooling effect on the planet (-47 W/m^{-2} in the global average). Second, clouds absorb longwave radiation emitted from the Earth's surface and re-emit this absorbed radiation back toward the surface and reduce the total longwave radiation emitted to space, acting as a warming effect on the planet (+26 W/m^{-2} in the global average). On average, in today's climate, clouds provide a net cooling effect on the planet (-21 W/m^{-2}; Hartmann 2016).

However, as the climate varies and changes, the effects of clouds on Earth's climate are not expected to remain constant. Given the complexity of clouds, which are affect by both

dynamic and thermodynamic factors, and the strong impact of clouds on Earth's radiative budget, clouds represent one of the largest sources of uncertainty in future climate projections. It is well known that, in response to an identical change in atmospheric CO_2 concentrations, GCMs produce a factor of 2 or greater difference in the global-mean surface temperature response (equilibrium climate sensitivity, ECS; Andrews et al. 2012; Forster et al. 2013), and this large spread in warming across models is attributable to clouds (Boucher et al. 2013; Vial et al. 2013; Zelinka et al. 2020). Recent studies have also shown that observational constraints on cloud feedbacks can be used to narrow the plausible range of ECS and consequently reduce the uncertainty in future global temperature projections (Sherwood et al. 2020; McCoy et al. 2022).

In a warming climate, the top-of-the-atmosphere (TOA) longwave (warming) effects of clouds are anticipated to increase. This is thought to be due to a robust positive longwave cloud feedback within the tropics caused by the tendency of tropical high clouds to rise in such a way as to maintain nearly the same cloud top temperature in a warming climate (fixed anvil temperature, FAT, hypothesis; Zelinka & Hartmann, 2010). However, shortwave cloud feedbacks in a warming climate remain varied across different models and additionally vary with latitude. For example, Myers and Norris (2016) found that, as a result of competing effects on subtropical low clouds by changes in global temperature and stability, there is thought to be a weak positive shortwave cloud radiative effect (CRE) that acts to warm the global climate. On the other hand, poleward of 45°, climate models project a robust increase in cloud optical depth (negative extratropical shortwave CRE) as the climate warms, hypothesized to be due to changes in the phase-partitioning in clouds from predominantly ice-dominated (which have a lower albedo) to liquid-dominated mixed phase clouds (which have a higher albedo) (Zelinka et al. 2012).

Recent studies have also shown that many current GCMs and reanalyses have large biases in TOA shortwave CRE, including over the Southern Ocean (Trenberth and Fasullo 2010; Ceppi et al. 2012). These biases potentially limit the ability of models to project changes in the climate under future anthropogenic forcing. For example, many GCMs indicate a large negative cloud feedback over the Southern Ocean in a warming climate (Trenberth and Fasullo 2010; Zelinka et al. 2012; Ceppi et al. 2016), which some studies have suggested is overestimated due to incorrect ice-liquid partitioning in Southern Ocean mixed-phase clouds (Gordon and Klein 2014; McCoy et al. 2016; Terai et al. 2016; Tan et al. 2016). This is a particular area of disagreement within models, as there is a 40K spread in model glaciation temperatures, or the temperature at which the model produces clouds that have an equal partitioning of ice and liquid based cloud drops (McCoy et al. 2016). Southern Ocean cloud biases within GCMs have also been linked to circulation and precipitation biases within both the extratropics (Ceppi et al. 2012; Ceppi et al. 2014) and the tropics (Hwang and Frierson 2013). It is thus important to understand and accurately simulate Southern Ocean and midlatitude clouds in order to better represent the climate system and improve future projections of Earth's climate.

One method by which to evaluate whether models are accurately representing observed cloud processes in the "cloud controlling factor" framework (see recent review by Klein et al 2017). This framework assumes that some measure of clouds ΔC relevant to radiative fluxes (e.g. shortwave CRE) can be represented by a first-order Taylor expansion in cloud-controlling factors x_i:

$$\Delta C = \sum_i \frac{\partial C}{\partial x_i} \Delta x_i \tag{1.1}$$

where the partial derivative $\frac{\partial C}{\partial x_i}$ represents the sensitivity of clouds to a cloud controlling factor. In this framework, observed sensitivities between clouds and these cloud-controlling factors are

diagnosed and compared to those in models to assess whether models are accurately simulating the relationships between clouds and their large-scale environment. While the cloud-controlling factor framework has been extensively applied in understanding tropical and subtropical clouds (e.g., Myers and Norris 2013, 2015, 2016; Qu et al. 2014, 2015; Seethala et al. 2015; McCoy et al. 2017; Klein et al. 2017), fewer studies have focused on the dynamic and thermodynamic factors controlling midlatitude clouds and their TOA radiative effects.

At midlatitudes, key cloud-controlling factors identified by previous studies include vertical velocity (e.g., Gordon et al. 2005; Norris and Iacobellis 2005; Li et al. 2014; Grise and Medeiros 2016, hereafter GM16; Wall et al. 2017; Kelleher and Grise 2019, hereafter KG19), lower tropospheric stability (Wood and Bretherton 2006; GM16; Naud et al. 2016; Wall et al. 2017; Zelinka et al. 2018; KG19), near-surface temperature advection (Norris and Iacobellis 2005; Wall et al. 2017; Zelinka et al. 2018), surface sensible heat fluxes (Miyamoto et al. 2018), sea surface temperature (Frey and Kay 2017), atmospheric temperature (Tselioudis et al. 1992; Gordon and Klein 2014; Terai et al. 2016; Ceppi et al. 2016), and downward longwave radiation by free-tropospheric clouds (Christensen et al. 2013). Upward vertical velocity anomalies in the midlatitudes are associated with the increased cloud fraction of mid- to high-clouds (e.g., Weaver and Ramanathan 1997; Li et al. 2014), as deep rising motion within the warm sector of extratropical cyclones drives nimbostratus and high-topped convective clouds (Lau and Crane 1995, 1997; Gordon et al. 2005). While downward vertical velocity anomalies inhibit the production of mid- to high-clouds, anomalous subsidence has been shown to be favorable for the formation of low clouds over the midlatitude oceans (Booth et al. 2013; Govekar et al. 2014; Li et al. 2014).

Additionally, enhanced subsidence above relatively low sea surface temperatures (SSTs) is conducive to the development of a strong boundary layer temperature inversion, which favors the development of low-cloud-typically in the form of marine stratocumulus (e.g. Klein and Hartmann 1993). A strong boundary layer inversion is particularly effective in coupling low clouds to their surface moisture source via turbulent mixing (e.g. Bretherton and Wyant 1997; Wood 2012), helping to develop and maintain low-cloud. Additionally, a strong boundary layer inversion acts to decouple the relatively moist boundary layer from the relatively dry free troposphere. This acts to inhibit dry air entrainment from the free troposphere, promoting the maintenance of low stratocumulus clouds within the boundary layer (e.g., Wood and Bretherton 2006). Cold-air advection near the surface in the midlatitudes has also been shown to increase low cloud cover as it enhances the turbulent fluxes from the relatively warm SSTs into the relatively cold and dry air above (Zelinka et al. 2018; Miyamoto et al. 2018). In contrast, higher SSTs strengthen the moisture gradient between the boundary layer and the free troposphere, enhancing the effectiveness of dry air entrainment into the boundary and consequently decreasing low-cloud amount and optical depth (Frey and Kay 2017).

GCMs often misrepresent the observed relationships among midlatitude clouds, their radiative properties, and cloud-controlling factors. Specifically, for Southern Ocean clouds, many models overestimate the dependence of shortwave CRE on vertical velocity (e.g., GM16; KG19), and underestimate the dependence of low-cloud fraction and shortwave CRE on lower tropospheric stability (GM16; Zelinka et al. 2018; KG19). Within CMIP5 models (Coupled Model Intercomparison Project 5; Taylor et al. 2012) two distinct model behaviors related to sensitivities of model Southern Ocean shortwave CRE to perturbations in lower tropospheric stability were found: those that underestimate the observed sensitivity (‘type I’ models) and

those that better simulate the observed sensitivity ('type II' models; Grise and Polvani 2014; GM16). As a result of this underestimation, a poleward shift of the midlatitude jet in type I models was found to be associated with a positive shortwave cloud radiative effect which would warm the climate as a result of a shift in the high- and mid-level clouds of the storm tracks and a reduction in the low-cloud within the Southern Ocean, a result not consistent with observations (Grise and Polvani 2014; GM16). Additionally, as the models underestimate the shortwave CRE sensitivity to lower tropospheric stability and overestimate shortwave CRE sensitivity to vertical velocity, they tend to create extratropical cyclones (associated with the midlatitude storm tracks) that contain clouds that are too bright (reflect more shortwave radiation to space than observations) and anticyclones that are too dim (KG19). These results further suggests that the accurate representation of model shortwave CRE sensitivities in the midlatitudes to cloud-controlling factors is important to estimating cloud feedbacks in a warming climate, as GCMs consistently predict a poleward shift of the midlatitude jet and extratropical storm tracks with increasing atmospheric CO_2 concentrations and/or global warming, particularly in the Southern Hemisphere (e.g., Kushner et al. 2001; Yin 2005; Barnes and Polvani 2013).

Recent studies have also suggested that, while dynamics may drive biases in model cloud simulation, clouds within models may also drive biases in simulated dynamical quantities (Bony et al. 2015). Clouds can alter temperature gradients in the atmosphere and cloud feedbacks depend on spatial warming patterns (Zhou et al. 2016) and thus depend on the temperature gradients that have been altered by the presence of clouds. As previous studies have shown that GCMs fail to accurately simulate the shortwave radiative effects of clouds over the Southern Ocean (Trenberth and Fasullo 2010), these biases in absorbed shortwave radiation have been

hypothesized to contribute to biases in the large-scale general circulation within GCMs via biases in the meridional surface temperature gradient (e.g., Ceppi et al. 2012).

Biases in the meridional surface temperature gradient are of particular importance to midlatitude dynamics because of the dependence of the midlatitude jet on thermal wind balance. Thermal wind balance indicates that the presence of a horizontal temperature gradient, such as the meridional equator-pole temperature gradient, is indicative of vertical wind shear, a change in speed and direction of the wind with height in the atmosphere. In the case of the equator-pole meridional temperature gradient, the resulting, balancing wind shear is the high-speed westerly winds of the midlatitude jet. As such, the midlatitude jet strength and position is associated with the strength and relative positioning of the meridional equator-pole temperature gradient. Additionally, from simple jet theory, regions of the jet are relevant to synoptic ascent and descent, which is the basis for the development, maintenance, and decay of synoptic weather systems such as the extratropical cyclones that make up the storm track. Thus, a bias in the meridional temperature gradient would suggest a jet with biases in its position and strength and a storm track with biases in its strength and position which would result in biases of associated cloud radiative effects. Southern Ocean shortwave cloud forcing biases have been proposed to be the primary driver of the jet latitude bias in the Southern Hemisphere, suggesting that reducing the shortwave cloud forcing biases in GCMs is critical to simulating the position of the jet and other large-scale dynamical features of the midlatitudes correctly in both the present (Ceppi et al. 2012) and future climate (Ceppi et al. 2014).

1.2 Types of Uncertainty in climate models

Uncertainty in future climate projections can be decomposed into three categories: scenario uncertainty, model uncertainty, and internal variability (Hawkins and Sutton 2009).

Scenario uncertainty refers to the incomplete knowledge of future climate forcings. These uncertainties in future anthropogenic emissions of GHGs and aerosols, stratospheric ozone concentrations, and land use changes are represented within CMIP6 (Coupled Model Intercomparison Project 6; Eyring et al. 2016) models by what are called 'Shared Socioeconomic Pathways' (SSPs). CMIP6 has five such pathways that vary in the level of increased anthropogenic emissions of aerosols and GHGs, from pathways with large reductions in emissions to pathways with continued large increases in emissions. As one cannot predict future policy related to the global emission of GHGs and aerosols, these pathways act to provide policymakers and stakeholders with a range of plausible outcomes resulting from climate change. Model uncertainty refers to differing model-to-model responses to the same external forcing. As discussed above, one notable aspect of model uncertainty relates to the uncertainty of future cloud radiative effects. Because these first two types of uncertainty refer to either incomplete information about future human behavior or varying model physics, they could potentially be reduced with better constraints on future emissions and improvements across climate models. Improvement, however, proves difficult to accomplish. Recent studies analyzing CMIP6 models have shown, for example, that the range in ECS has not narrowed between CMIP5 and CMIP6 and has increased instead (Meehl et al. 2020; Zelinka et al. 2020). Additionally, models continue to overestimate shortwave CRE sensitivity to vertical motion and underestimate shortwave CRE sensitivity to lower tropospheric stability (Grise and Kelleher 2021).

The third form of uncertainty, internal variability, can be defined as the variability present in the climate system in the absence of external forcing. Internal variability arises from the chaotic non-linear dynamical processes that are intrinsic to the atmosphere. This means that

solutions to the set of fluid dynamical equations are unstable to small modifications in their initial conditions and can thus evolve into largely different states (as in Lorenz 1963). Although internal variability is unforced, it can still manifest in the long-term trends in climate variables. For example, using an ensemble of a model forced with slightly differing initial conditions, Deser et al. (2014) show that winter temperature trends over the next half century across North America vary widely across the realizations as a result of internal variability. Additionally, trends in some variables are more sensitive to internal variability in the climate system than others. For example, North American precipitation trends are more related to internal variability than temperature trends. As a result, forced trends in precipitation may be masked out by internal variability in some future projections (Deser et al. 2012, 2014) and may not be distinguishable from internal variability until after 2100 (Giorgi and Bi 2009).

As the uncertainty driven by internal variability is inherent to the climate system and cannot be eliminated, and uncertainty driven by scenario uncertainty and model uncertainty has proven difficult to reduce across model generations, it is more accurate to communicate a range of possible future trends in climate variables rather than one specific value (usually the multi-model mean). One method to do this is through the use of a large initial-condition ensemble in which one model is run many times with identical external forcing and with miniscule variance in the initial conditions (see recent review by Deser et al. 2020). Through this, the mean response across the ensemble can be thought of as the forced response, and deviations around this response represent the internal variability within the climate system. By adding multiple models that have run initial-condition ensembles, one can then calculate estimates of both the internal variability within the climate system and the contribution of uncertainty driven by model-to-model differences.

Through these initial-condition ensembles, a plausible range in future climate trends can be acquired. It is thus worthwhile to understand the physical drivers that govern the model-to-model variability and internal variability in the trends. One such method is the "storylines" approach of Zappa and Shepherd (2017) (see also Schmidt and Grise 2021; Shepherd et al. 2018; Shepherd 2019; Zappa 2019). In this approach, physical drivers are first identified than can explain a large fraction of the variance in the future trends of a given climate variable. At mid and high latitudes, these physical drivers are usually related to either the annular modes of circulation variability or the attendant effects of coupled ocean-atmosphere variability via atmospheric teleconnections (Deser et al. 2012). Once the physical drivers are identified, various high and low impact storylines for each variable can be developed through the use of linear regression, creating a range of plausible future trends in the climate based on the plausible future trends in the physical drivers of the climate system.

In Chapter 2, I discuss the varied midlatitude shortwave cloud radiative responses to Southern Hemisphere shifts in the midlatitude jet and Hadley circulation and use this to illustrate why the cloud controlling framework may be problematic in estimating cloud feedbacks. In Chapter 3, I use the "storylines" approach to create storylines of North American mean and extreme temperature and precipitation trends and determine whether the variability in the trends is the result of internal variability. I find that internal variability plays a larger role in driving North American precipitation trends, and that constraints in ECS (such as from McCoy et al. 2022) can effectively constrain variability in future trends in annual maximum consecutive dry days. Motivated by the results of Chapter 3, in Chapter 4, I explore changes in the seasonal daily distribution of temperature as a result of climate change. Similar to previous studies, I find that the distribution of temperature during the winter is decreasing in variance and increasing in

skewness at mid-to-high latitudes due to the non-linear meridional warming due to climate change ('Arctic amplification'). Chapter 5 contains a brief summary, as well as potential future work motivated by these studies.

Chapter 2: Varied midlatitude shortwave cloud radiative responses to Southern Hemisphere circulation shifts

2.1 Introduction

In a changing climate, large-scale circulation features (such as the eddy-driven midlatitude jets and the poleward edges of the Hadley circulation) are expected to shift meridionally. While variability in positions of the jet and Hadley cell extent on subseasonal-to-seasonal time scales is primarily associated with internal variability in the climate system (Thompson and Wallace 2000; Nguyen et al. 2013), variability in their positions on longer time scales can be strongly affected by anthropogenic forcing. Climate models forced by stratospheric ozone depletion show a poleward shift of the summertime Southern Hemisphere (SH) midlatitude jet and Hadley cell edge (Thompson and Solomon 2002; Gillett and Thompson 2003; Polvani et al. 2011), and climate models forced by increased atmospheric greenhouse gases show poleward shifts in the midlatitude jets (e.g., Barnes and Polvani 2013) and the extent of the Hadley cell (e.g., Lu et al. 2007) in both hemispheres. As changes in clouds associated with shifts in large-scale circulation patterns are considered a potential source of radiative feedbacks on climate change (Boucher et al. 2013), it is important to understand how these circulation shifts impact clouds and what large-scale dynamical changes are responsible for altering the associated cloud radiative effects (CRE).

As the midlatitude jet shifts poleward, large-scale ascending motion and the high-topped clouds associated with the extratropical storm tracks closely follow (e.g., Grise et al. 2013),

suggesting a possible shortwave warming feedback as the clouds move to a higher latitude where they reflect less sunlight to space (e.g., Bender et al. 2012). However, several studies have documented little to no net shortwave warming response in SH midlatitudes associated with a poleward jet shift in observations and varied cloud radiative responses to poleward jet shifts across models (Grise and Polvani 2014; Grise and Medeiros 2016, hereafter GM16). This is because low clouds and their attendant shortwave CRE (SWCRE), which are closely related to boundary layer stability changes, often increase in the region vacated by the storm track clouds, a commonly underestimated effect in models (Ceppi and Hartmann 2015; GM16). Studies of dynamical controls on midlatitude clouds have mainly focused on the role of the midlatitude jet, but Tselioudis et al. (2016) found that shifts in the Hadley cell extent more strongly affect midlatitude clouds than shifts in the jet position, particularly at lower midlatitudes (30˚-40˚).

As the position of the SH eddy-driven jet and Hadley cell edge strongly co-vary (Kang and Polvani 2011), it is surprising that variability in the positions of the SH jet and Hadley cell edge are associated with different cloud responses. The purpose of this work is to reconcile the differing SWCRE responses to these two circulation feature shifts through the use of dynamical "cloud-controlling factors" [see review by Klein et al. (2017)]. This framework to connect large-scale dynamical variability to variability in cloud radiative effects has been widely used in understanding both tropical (Myers and Norris 2013; Qu et al. 2015) and midlatitude (Gordon et al. 2005; GM16; Kelleher and Grise 2019) environments.

In this chapter, following GM16, we consider two cloud-controlling factors to explain the midlatitude SWCRE anomalies associated with poleward circulation shifts: 500-hPa vertical velocity (ω_{500}) and estimated inversion strength (EIS), a metric for the strength of the marine boundary layer temperature inversion (Wood and Bretherton 2006). Upward vertical velocity

anomalies at midlatitudes are associated with increased mid-to-upper tropospheric cloud coverage (Weaver and Ramanathan 1997; Li et al. 2014), such as the high-topped clouds that occur in regions of deep rising motion within extratropical cyclones (Lau and Crane 1995, 1997; Gordon et al. 2005), whereas the development of a strong boundary layer temperature inversion acts to reduce dry-air entrainment from the free troposphere into the boundary layer, favoring the development of low-level stratocumulus clouds (e.g., Klein and Hartmann 1993). As a result, while "storm-track" clouds are likely to follow the jet poleward as it shifts (Grise et al. 2013), large-scale dynamical changes equatorward of the shifting jet act to compensate for this shift and increase low-level maritime clouds in those regions (GM16).

Through the use of this cloud-controlling factor framework, we will assess the relative impacts of large-scale dynamical changes on midlatitude SWCRE associated with meridional shifts in the SH midlatitude jet and Hadley cell edge. We find that, as in GM16, large-scale dynamical changes associated with a SH midlatitude jet shift occur at latitudes where the effects of changing EIS and mid-tropospheric vertical velocity on SWCRE are nearly balanced, leading to a near-zero net change in SWCRE associated with meridional shifts of the SH midlatitude jet. In contrast, we find that large-scale dynamical changes associated with a poleward extension of the SH Hadley cell occur at latitudes where the effects of vertical velocity anomalies on SWCRE dominate over those associated with changes in EIS. This difference leads to a small net shortwave warming effect at midlatitudes associated with a poleward shift of the SH Hadley cell extent.

2.2 Data and Methods

2.2a Data

To assess the relationships among circulation shifts, dynamical cloud-controlling factors, and SWCRE, we use two observation-based datasets. First, we use ERA-5 reanalysis (Hersbach et al. 2020) to obtain monthly-mean dynamical variables to compute ω_{500}, EIS, and the midlatitude jet and Hadley cell edge locations. Second, monthly-mean top-of-atmosphere (TOA) shortwave radiative fluxes from CERES EBAF-TOA version 4.1a (Loeb et al. 2018) are used to compute SWCRE.

To assess whether the current generation of global climate models (GCMs) is able to reproduce the relationships derived from observations, we use output from 39 models that participated in CMIP6 (Eyring et al. 2016; listed in Table 2.S1). For this study, we use the pre-industrial control (piControl) run of each model, which is a coupled atmosphere/ocean control run that imposes non-evolving pre-industrial conditions.

2.2b Methods

Following previous work (GM16), we consider two dynamical cloud-controlling factors: ω_{500} and EIS. EIS is defined as follows (Wood and Bretherton 2006):

$$EIS = LTS - \Gamma_m^{850}(z_{700} - LCL) \quad (2.1),$$

where lower tropospheric stability (LTS) is the difference between potential temperature at 700-hPa and the surface, Γ_m^{850} is the moist adiabatic lapse rate at 850-hPa, z_{700} is the height of the 700-hPa level, and LCL is the height of the lifted condensation level (as in Georgakakos and Bras 1984). While both LTS and EIS are measures of boundary layer stability, we focus on EIS which is more strongly correlated with low cloud amount in midlatitude low cloud regimes

(Wood and Bretherton 2006). Additionally, while other cloud-controlling factors impact midlatitude SWCRE (such as low-level temperature advection and sea surface temperature), they play a minor role in the observed SWCRE anomalies associated with a poleward shift in the SH midlatitude jet (Grise and Kelleher 2021), so we do not consider them here.

As in Grise and Polvani (2014), we calculate the position of the SH midlatitude jet by computing the latitude of the 850-hPa zonal-mean zonal wind maximum using a quadratic fit to the three grid points nearest the maximum gridded zonal-mean zonal wind. We calculate the latitude of the SH Hadley cell extent by computing the zero-crossing latitude of the meridional mass stream function at 500hPa using the Tropical-width Diagnostics (TropD) software package (Adam et al. 2018).

We calculate SWCRE as the difference in outgoing shortwave radiation at TOA between clear-sky and all-sky scenes (e.g., Ramanathan et al. 1989). We focus on SWCRE here, which is affected by both high and low clouds. In contrast, longwave CRE anomalies associated with poleward circulation shifts more closely follow the high clouds of the midlatitude storm track and are thus dominated by changes in ω_{500} (GM16).

We use a simple multiple linear regression model to predict SWCRE anomalies associated with shifts in the SH midlatitude jet and Hadley cell extent:

$$\Delta SWCRE = \frac{\partial(SWCRE)}{\partial \omega_{500}} \Delta\omega_{500} + \frac{\partial(SWCRE)}{\partial(\mathrm{EIS})} \Delta EIS \tag{2.2}$$

where $\Delta SWCRE$ is the predicted SWCRE anomaly, $\Delta\omega_{500}$ and ΔEIS are the changes in each cloud-controlling factor associated with a one standard deviation shift in the SH midlatitude jet

or SH Hadley cell extent, and $\frac{\partial(SWCRE)}{\partial\omega_{500}}$ and $\frac{\partial(SWCRE)}{\partial(\mathrm{EIS})}$ are the sensitivities of SWCRE to anomalies from the mean-state of each cloud-controlling factor.

2.3 Results

In order to assess whether there are differences in the SWCRE anomalies associated with shifts in the SH midlatitude jet and Hadley cell extent, we first separately regress monthly zonal-mean anomalies in SWCRE against monthly anomalies in the position of the SH jet and Hadley cell extent (Fig. 1.1). The results here (and in subsequent figures) are only for SH summer months (DJF) when incoming solar insolation is maximized, and the curves shown are for a one standard deviation shift in the circulation features poleward. Note that, while a one standard deviation poleward shift in the midlatitude jet (2.15°) is larger than a one standard deviation shift in the Hadley cell extent (1.26°), we plot results in terms of standard deviation as it represents a similar deviation from the norm for both circulation features.

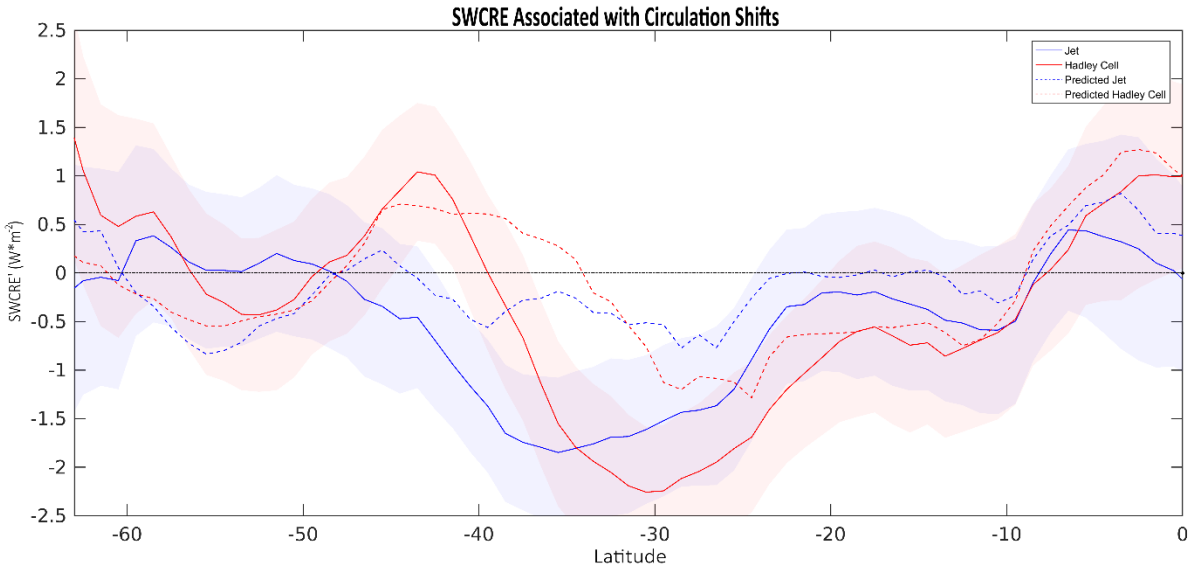

Figure 1.1 Zonal mean SWCRE response to a one standard deviation poleward shift of the SH midlatitude jet (blue lines) and extent of the SH Hadley cell (red lines). Solid lines represent the observed SWCRE response, and dashed

lines represent the predicted SWCRE response from equation 2. Shaded areas represent the 95% confidence interval related to a one standard deviation poleward shift in the circulation features.

While shifting each circulation feature poleward has similar impacts on SWCRE in the tropics, there are noteworthy differences at midlatitudes. For example, there is little SWCRE change for a poleward shift of the jet at midlatitudes (~45°S-55°S; solid blue line), but there is a positive SWCRE anomaly at similar latitudes for a shift in the Hadley cell extent (solid red line). Although the two circulation features strongly co-vary with one another during the SH summer season (Kang and Polvani 2011), there remains a substantial fraction of the variance of each circulation feature that is independent of the other, leading to different SWCRE anomalies for each circulation shift. A simple multiple linear regression model (equation 2.2) with only two dynamical predictors (EIS and ω_{500}) can approximately capture the differing SWCRE response between poleward shifts of the jet and Hadley cell extent (red and blue dashed lines; R^2 =0.23 and 0.52, respectively; see summary statistics in Table 2.S2). While this simple model is not able to fully capture the observed SWCRE responses (particularly to poleward jet shifts), it is able to capture distinct SWCRE responses at midlatitudes between jet shifts and Hadley cell extent changes, suggesting that EIS and ω_{500} may be helpful in explaining the differing SWCRE responses.

By regressing zonal-mean anomalies in the two dynamical cloud-controlling factors against anomalies in the position of the circulation features, we can investigate what dynamical differences exist between meridional shifts of the SH midlatitude jet (Fig. 2.2, blue lines) and Hadley cell extent (Fig. 2.2, red lines). The EIS anomalies associated with a poleward jet shift peak more strongly at SH midlatitudes near 50˚S, while the EIS anomalies associated with a poleward shift in the Hadley cell extent are spread out more broadly in latitude (Fig. 2.2a). The

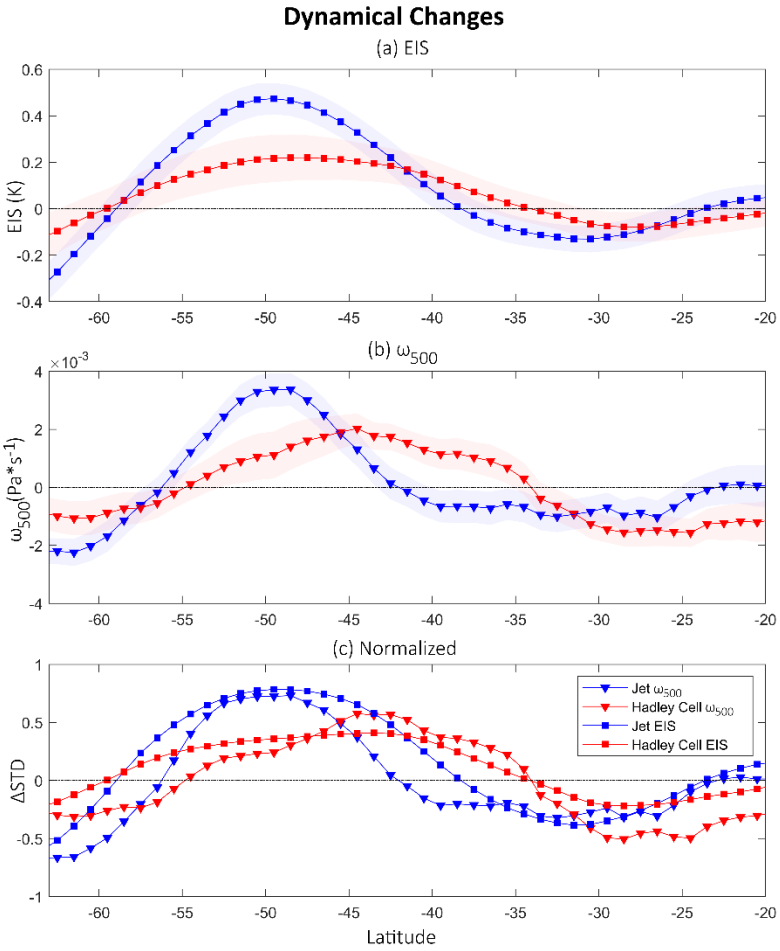

Figure 2.2 Response of zonal mean EIS (a, square markers) and ω_{500} (b, triangle markers) to a one standard deviation poleward shift in the SH midlatitude jet (blue lines) and extent of the SH Hadley cell (red lines). Panel c shows the dynamical changes for each circulation shift normalized by the standard deviation of the dynamical cloud-controlling factors. Shaded areas (a, b) represent the 95% confidence interval related to a one standard deviation poleward shift in the circulation features.

ω_{500} anomalies associated with a poleward jet shift similarly peak near 50˚S, but are offset from the ω_{500} anomalies associated with a poleward shift in the Hadley cell extent, which peak around 45˚S (Fig. 2.2b). While these differences are notable, in order to directly compare the dynamical changes associated with the shifting circulation features, we normalize the anomalies in the two cloud-controlling factors by their standard deviations (Fig. 2.2c). The results confirm that the

positive dynamical anomalies associated with a poleward shift in the SH Hadley cell extent (red lines, square markers for EIS and triangle markers for ω_{500}) are broader in latitudinal extent and peak equatorward of the dynamical anomalies associated with a poleward shift in the SH midlatitude jet (blue lines, square markers for EIS and triangle markers for ω_{500}). Furthermore, Fig. 2.2c shows that the maximum normalized anomalies of ω_{500} and EIS have similar magnitudes and positions both for the jet shift (~0.75 standard deviations near 50˚S) and the shift in Hadley cell extent (~0.5 standard deviations near 45˚S). Overall, Fig. 2.2 reveals that the latitude where a poleward shift in the SH jet most affects the dynamics is about five degrees poleward of the latitude where a poleward shift in the SH Hadley cell extent most impacts the dynamics.

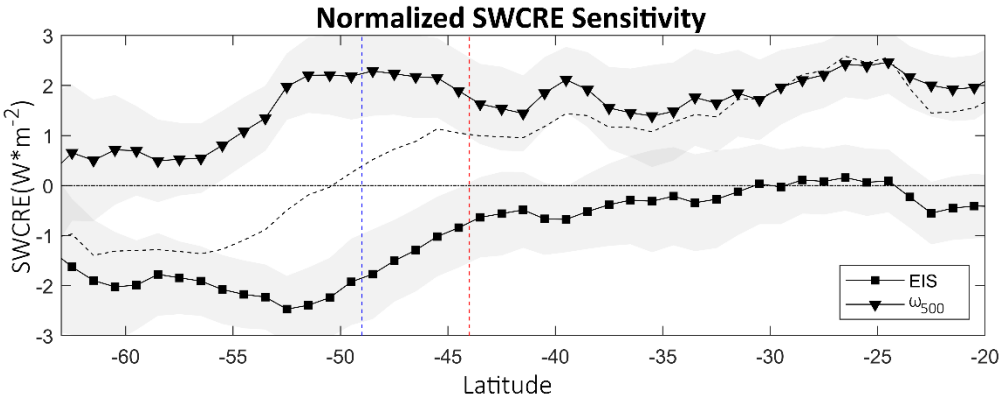

Figure 2.3 SWCRE sensitivity to a one standard deviation change in EIS (square markers) and ω_{500} (triangle markers). The dashed line represents the linear combination of the two sensitivities, and the vertical dashed lines represent the latitudes of maximum dynamical change for poleward shifts of the midlatitude jet (blue) and extent of the Hadley cell (red) (as shown in Fig. 2.2c). Shaded areas represent the 95% confidence interval of the SWCRE sensitivities.

As the latitude where dynamical changes occur as a result of the two circulation shifts differs (Fig. 2.2c), the SWCRE responses to the two circulation shifts (as shown in Fig. 2.1) may be distinct from one another because of differing SWCRE sensitivities to dynamics at the

differing latitudes. To assess this, we regress SWCRE on zonal-mean EIS and ω_{500} perturbations: i.e., ($\frac{\partial(SWCRE)}{\partial(\mathrm{EIS})}$ and $\frac{\partial(SWCRE)}{\partial\omega_{500}}$) as defined in equation 2.2. Figure 2.3 plots these regression coefficients as a function of latitude, with the regression coefficients normalized by the standard deviations in the dynamical cloud-controlling factors. The normalization allows us to directly compare the SWCRE sensitivities to EIS and ω_{500} on the same scale. As expected, in SH midlatitudes, increases in EIS are associated with decreased SWCRE (increased cloud reflection) (Fig. 2.3, square markers), consistent with the connection between boundary layer stability and low clouds. In contrast, increases in ω_{500} (anomalous descent) are associated with increased SWCRE (decreased cloud reflection) (Fig. 2.3, triangle markers), consistent with the connection between ascending motion and mid-to-high clouds and the connection between subsidence and reduced boundary layer cloudiness (e.g., Myers and Norris 2013).

As the magnitude of the changes in the two cloud-controlling factors are similar (in terms of standard deviations) for each circulation shift (Fig. 2.2c), a direct comparison of the two sensitivities may provide information about whether the changes in ω_{500} or EIS dominate the total SWCRE response. To this second point, we plot a linear combination of the two normalized sensitivities (Fig. 2.3, black dashed line). We find that in the tropics, subtropics, and lower midlatitudes, the sensitivity of SWCRE to changes in ω_{500} is larger in magnitude than the sensitivity to changes in EIS. In the upper midlatitudes, however, this relationship reverses with SWCRE sensitivity to EIS becoming larger in magnitude, with the transition occurring near 50°S.

As shown in Fig. 2.2, the peak anomalies in ω_{500} and EIS associated with a poleward shift in the SH midlatitude jet occur at 49˚S (Fig. 2.3, blue dashed line), whereas the peak anomalies in ω_{500} and EIS associated with a poleward shift in the SH Hadley cell extent occur at 44˚S (Fig.

2.3, red dashed line). For a poleward shift in the SH Hadley cell extent, the latitude of maximum dynamical changes occurs solidly within the ω_{500}-dominated regime (i.e., where the black dashed line in Fig. 2.3 is greater than zero). Consequently, for similar magnitude positive anomalies in ω_{500} and EIS (Fig. 2.2c, red), the impact of the ω_{500} anomalies on SWCRE is greater, consistent with the positive SWCRE response at this latitude observed in association with a poleward shift in the SH Hadley cell extent (Fig. 2.1, red). Conversely, for a poleward shift in the SH midlatitude jet, the latitude of maximum dynamical changes occurs close to the transition latitude between the ω_{500}- and EIS-dominated regimes (i.e., where the black dashed line in Fig. 2.3 crosses zero). So, for similar magnitude positive anomalies in ω_{500} and EIS (Fig. 2.2c, blue), the impact of the ω_{500} and EIS anomalies on SWCRE are roughly equal and opposite, consistent with a near-zero net SWCRE response at this latitude observed in association with a poleward shift in the SH midlatitude jet (Fig. 2.1, blue).

2.4 Summary and Discussion

Changes in clouds as a result of circulation shifts are thought to be a potential source of feedbacks onto the climate system (Boucher et al. 2013; Bony et al. 2015). Recent work has shown that, while the high-topped clouds associated with extratropical cyclones shift with the midlatitude jet stream, there is little to no net shortwave cloud radiative warming effect observed in conjunction with a poleward shift in the SH midlatitude jet, due to competing effects of poleward shifting high-topped extratropical storm-track clouds and increasing low clouds on the equatorward flank of the jet (GM16). Other recent work has suggested that the extent of the Hadley cell correlates more robustly with midlatitude cloud variations than the position of the midlatitude jet, particularly in the lower midlatitudes (Tselioudis et al. 2016). As the SH

summertime midlatitude eddy-driven jet and the Hadley cell extent strongly co-vary interannually (Kang and Polvani 2011), this work sought to reconcile the differences in SWCRE responses between the two circulation shifts and to comment on the potential dynamical reasons for any differences.

Our results confirm that there are differing SWCRE anomalies observed in association with poleward shifts in the SH jet and Hadley cell extent during the summer (DJF) season (Fig. 2.1). Using a cloud-controlling factor framework, we show that dynamical changes related to the shifting circulation features occur at different latitudes, with the largest dynamical changes associated with a poleward jet shift located about five degrees poleward of those associated with a poleward shift in the Hadley cell extent (Fig. 2.2c). The latitude of maximum dynamical changes observed in association with a poleward shift in the SH Hadley cell extent is within a dynamical regime where SWCRE anomalies are dominated by changes in ω_{500} (Fig. 2.3), such that anomalous subsidence near 45˚S leads to an increase in SWCRE at nearby latitudes (Fig. 2.1, red). Conversely, the latitude of maximum dynamical changes observed in association with a poleward shift in the SH midlatitude jet is within a dynamical regime where SWCRE anomalies are equally sensitive to changes in ω_{500} and EIS (Fig. 2.3), such that the competing effects of anomalous subsidence and positive EIS anomalies near 50˚S lead to little net SWCRE change at nearby latitudes (Fig. 2.1, blue).

How well do GCMs capture these observed relationships? The solid lines in Figs. 2.4a and 2.4b show the CMIP6 multi-model-mean zonal-mean SWCRE anomalies associated with a poleward shift in the SH midlatitude jet and Hadley cell extent. The models reproduce the positive SWCRE anomaly at SH midlatitudes associated with a poleward shift in the SH Hadley

cell extent (Fig. 2.4b, compare solid and dashed lines), although they overestimate its magnitude compared to observations (see also Lipat et al. 2017, 2018). In contrast, the models also produce

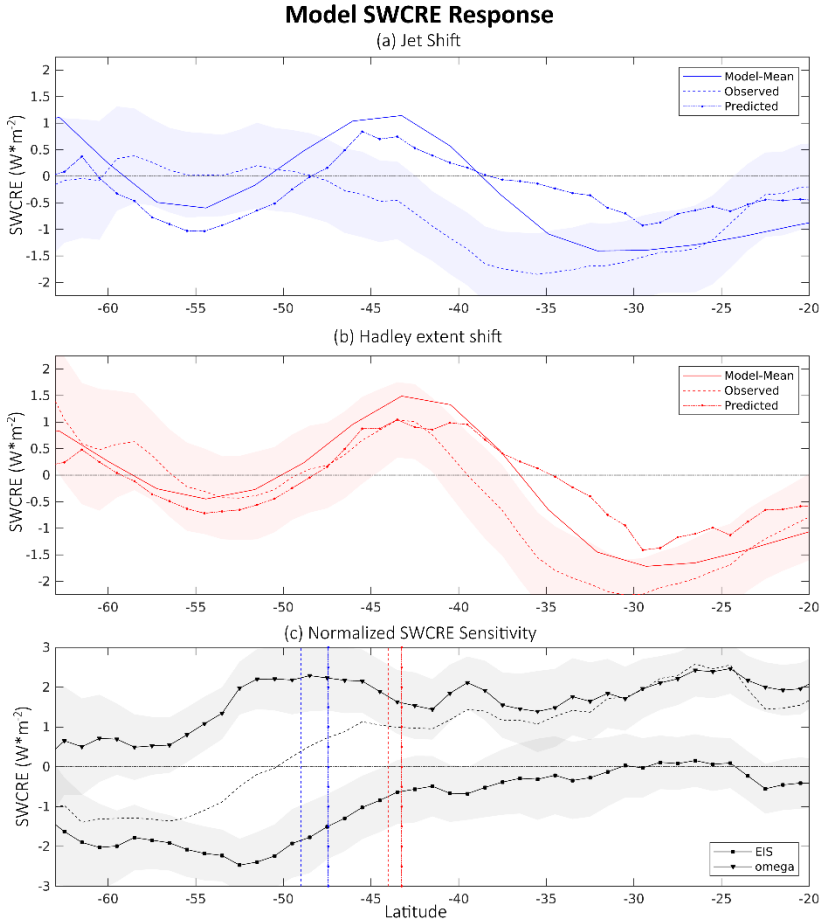

Figure 2.4 (a,b) CMIP6 model average zonal mean SWCRE response to a one standard deviation poleward shift in the SH midlatitude jet (a) and extent of the SH Hadley cell (b). The solid lines represent the model simulated shortwave CRE response, the dashed lines are the observed SWCRE response (as in solid lines in Fig. 2.1), and the dotted-dashed lines represent the predicted SWCRE response to the circulation shift using equation 2.2 with model average dynamical changes and observed SWCRE sensitivity to the dynamical cloud-controlling factors. The shaded areas in each panel represent the 95% confidence interval of observed SWCRE sensitivity to observed poleward shifts in the jet and Hadley cell extent (as in Fig. 2.1). (c) As in Fig. 2.3, but also including the CMIP6 model average latitudes of maximum dynamical change for poleward shifts in the SH midlatitude jet (blue dotted-dashed line) and extent of the SH Hadley cell (red dotted-dashed line).

a positive SWCRE anomaly at SH midlatitudes associated with a poleward shift in the SH midlatitude jet (Fig. 2.4a, compare solid and dashed lines), which does not occur in observations (Grise and Polvani 2014; GM16).

One may suppose that the model bias results from errors in the SWCRE sensitivity to the cloud-controlling factors, which is highly dependent on model cloud parameterizations. Presumably, if we constrain the models to have the same SWCRE sensitivity as observations, they should better replicate the observed response. To test this, we apply the same multiple linear regression model as we did for observations in Fig. 2.1 (equation 2.2), but instead we multiply the observed sensitivities of SWCRE to each cloud-controlling factor by the corresponding changes in the cloud-controlling factors from the CMIP6 multi-model mean. The results are shown in the dotted-dashed lines in Figs. 2.4a and 2.4b. We find that, by constraining the SWCRE sensitivities to observations, the model dynamics are able to recreate the observed SWCRE anomalies associated with a poleward shift in the SH Hadley cell extent at midlatitudes (Fig. 2.4b, compare dashed and dotted-dashed lines). However, even after constraining the SWCRE sensitivities to observations, the model dynamics are not able to recreate the observed SWCRE anomalies associated with a poleward SH jet shift (Fig. 2.4a, compare dashed and dotted-dashed lines; a scatter plot of individual models is shown in supplemental Fig. 2.S1). This occurs because the CMIP6 multi-model mean jet location is too far equatorward (Simpson et al. 2020), such that the peak changes in the cloud-controlling factors associated with a jet shift occur too far equatorward on average in models (Fig. 2.4c; compare blue dashed and dotted-dashed lines). While the peak changes in the cloud-controlling factors associated with a SH Hadley cell edge shift also occur too far equatorward in CMIP6 models compared to observations (Fig. 2.4c; compare red dashed and dotted-dashed lines), the equatorward model bias in jet latitude is more

consequential, as it shifts the model dynamical anomalies into a different regime from observations, where the SWCRE sensitivity is dominated by changes in ω_{500}. Consistent with this argument, most (but not all) models that have climatological jet positions similar to observations better simulate both the SWCRE and dynamical response to poleward shifts of the jet (not shown). Having both the correct jet position (as shown here) and the correct SWCRE sensitivity to cloud-controlling factors (as shown in GM16) is necessary for models to properly simulate SWCRE changes related to poleward jet shifts.

This result is similar to that of Lipat et al. (2017, 2018), who found that an equatorward-biased Hadley cell edge in models leads to incorrect radiative responses to poleward shifts of the circulation features as a result of climate change. Furthermore, the results in Fig. 2.4 provide a cautionary example of the limitations of combining sensitivities of cloud properties to dynamical cloud-controlling factors from observations with changes in those cloud-controlling factors from GCMs using a multiple linear regression model. Such a technique is commonly used to provide an observational constraint on cloud feedbacks (e.g., Klein et al. 2017). However, here we have shown that biases in the GCMs' mean state dynamics may inherently lead to incorrect results from such a procedure.

2.5 Supplemental Information

Table 2.S1 List of CMIP6 models used in this study.

Model name	Modeling Center
ACCESS-CM2	Commonwealth Scientific and Industrial Research Organisation, Australian Research Council Centre of Excellence for Climate System Science

ACCESS-ESM1-5	Commonwealth Scientific and Industrial Research Organisation, Australian Research Council Centre of Excellence for Climate System Science
AWI-CM-1-1-MR	Alfred Wegener Institute, Helmholtz Centre for Polar and Marine Research
AWI-ESM-1-1-LR	Alfred Wegener Institute, Helmholtz Centre for Polar and Marine Research
BCC-CSM2-MR	Beijing Climate Center, China Meteorological Administration
BCC-ESM1	Beijing Climate Center, China Meteorological Administration
CAMS-CSM1-0	Chinese Academy of Meteorological Sciences
CanESM5	Canadian Centre for Climate Modelling and Analysis
CESM2-FV2	National Center for Atmospheric Research, Climate and Global Dynamics Laboratory
CESM2	National Center for Atmospheric Research, Climate and Global Dynamics Laboratory
CESM2-WACCM-FV2	National Center for Atmospheric Research, Climate and Global Dynamics Laboratory
CESM2-WACCM	National Center for Atmospheric Research, Climate and Global Dynamics Laboratory
CNRM-CM6-1	Centre National de Recherches Météorologiques/Centre Européen de Recherche et de Formation Avancée en Calcul Scientifique

CNRM-ESM2-1	Centre National de Recherches Météorologiques/Centre Européen de Recherche et de Formation Avancée en Calcul Scientifique
E3SM-1-0	Lawrence Livermore National Laboratory
E3SM-1-1	Lawrence Livermore National Laboratory
EC-Earth3	European EC-Earth Consortium
EC-Earth3-Veg	European EC-Earth Consortium
FGOALS-f3-L	Chinese Academy of Sciences
FGOALS-g3	Chinese Academy of Sciences
GISS-E2-1-G	NASA Goddard Institute for Space Studies
GISS-E2-1-H	NASA Goddard Institute for Space Studies
GISS-E2-2-G	NASA Goddard Institute for Space Studies
HadGEM3-GC31-LL	Met Office Hadley Centre
HadGEM3-GC31-MM	Met Office Hadley Centre
INM-CM4-8	Institute for Numerical Mathematics, Russian Academy of Science
INM-CM5-0	Institute for Numerical Mathematics, Russian Academy of Science
IPSL-CM6A-LR	L'Institut Pierre-Simon Laplace
KACE-1-0-G	National Institute of Meteorological Sciences/Korea Meteorological Administration, Climate Research Division

MIROC6	Atmosphere and Ocean Research Institute (The University of Tokyo), National Institute for Environmental Studies, and Japan Agency for Marine-Earth Science and Technology
MIROC-ES2L	Atmosphere and Ocean Research Institute (The University of Tokyo), National Institute for Environmental Studies, and Japan Agency for Marine-Earth Science and Technology
MPI-ESM-1-2-HAM	Max Planck Institute for Meteorology
MPI-ESM1-2-HR	Max Planck Institute for Meteorology
MPI-ESM1-2-LR	Max Planck Institute for Meteorology
MRI-ESM2-0	Meteorological Research Institute
NorESM1-F	NorESM Climate modeling Consortium
SAM0-UNICON	Seoul National University
TaiESM1	Research Center for Environmental Changes, Academia Sinica
UKESM1-0-LL	Met Office Hadley Centre

Table 2.S2 Summary statistics comparing the observed zonal-mean SWCRE responses to poleward SH circulation shifts (as shown in Fig. 1, solid lines) with those from linear regression models based on EIS and ω_{500}. The top row shows the R^2 value and root mean square error (RMSE) for the multiple linear regression model based on both cloud controlling factors (Eq. 2, as shown in Fig. 1, dashed lines), and the bottom two rows show the R^2 value and RMSE for each of the two terms separately. For the R^2 values, asterisks signify significance at the 95% level.

	Jet shift	Hadley cell extent shift

	R^2	RMSE ($W*m^{-2}$)	R^2	RMSE ($W*m^{-2}$)
Multiple linear regression model (Eq. 2)	0.2296*	0.7122	0.5245*	0.7472
EIS term only	0.0834*	1.0849	0.0269	1.1180
ω_{500} term only	0.3766*	0.8381	0.5257*	0.8028

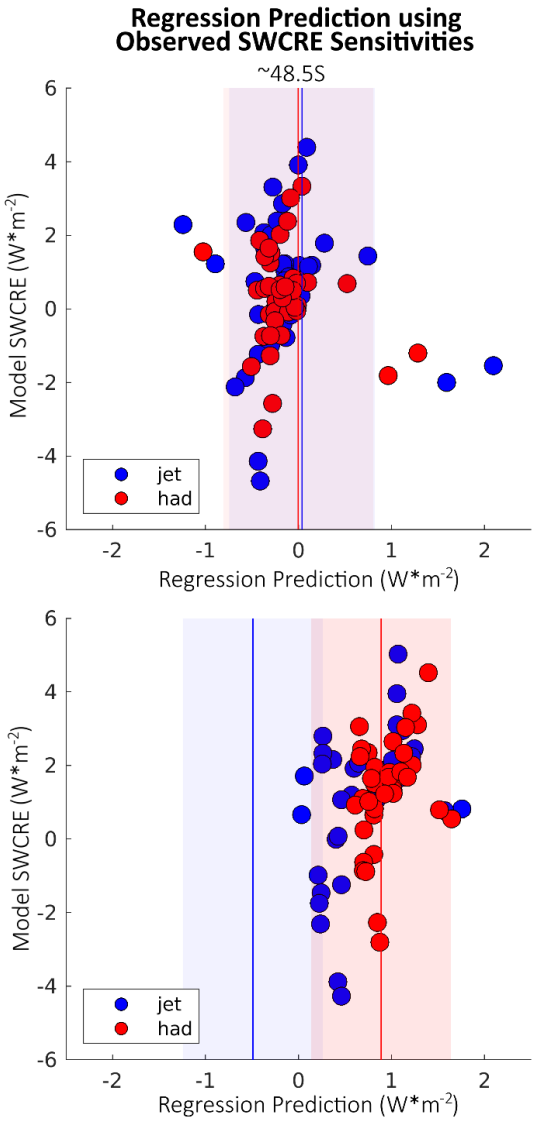

Figure 2.S1 Simple regression model using observed SWCRE sensitivities to EIS and ω_{500}. The top panel is for a 5° band around the latitude at which dynamics change the most for an observed jet shift and the bottom panel for the 5° band around the same location for a Hadley cell extent shift. Shaded regions and solid lines represent the observed SWCRE change and confidence interval for poleward shifts in the jet (blue) and Hadley cell (red). Each model is represented by a single point for both jet shifts (blue) and Hadley cell extent shifts (red). The y-axis represents the actual model SWCRE response to circulation shifts, and the x-axis represents the prediction from the regression model using observed swcre sensitivities to dynamical changes.

Chapter 3: Variability in Projected North American Mean and Extreme Temperature and Precipitation Trends for the 21st Century: Model-to-model Differences vs. Internal Variability

3.1 Introduction

Projecting future changes in climate variables, such as means and extremes in temperature and precipitation, as a result of anthropogenic climate change is a key focus of the global climate science community, as it allows governments and other stakeholders to assess, prepare for, and act to mitigate impacts on local communities. Understanding why global climate models predict future changes in temperature and precipitation, and why different models vary in their future projections, is necessary to help narrow the range of possible future climate scenarios communicated to policymakers.

In response to increasing greenhouse gases (GHGs), global climate models agree that near-surface air temperatures typically warm less over the oceans than over land (e.g., Sutton et al. 2007; Byrne and O'Gorman 2013) and experience amplified warming in the Arctic ("Arctic amplification"; Holland and Bitz 2003; Pithan and Mauritsen 2014). Similarly, models generally agree that zonal-mean precipitation will increase in the deep tropics, decrease in the subtropics, and increase at high latitudes (Held and Soden 2006; Seager et al. 2010; Scheff and Frierson

2012). However, the impacts of future temperature and precipitation changes will not be experienced at the global scale, but locally. At local scales, future temperature and precipitation trends are much more uncertain, particularly for precipitation trends across midlatitude land regions such as the contiguous United States (Deser et al. 2012; Schmidt and Grise 2021, hereafter SG21).

In terms of extremes, the frequency and intensity of extreme hot temperature events has increased, and the frequency and intensity of extreme cold temperature events has decreased in recent decades. Models project that these trends will continue with increasing greenhouse gases. This is true both globally and regionally (Sillmann et al. 2013; Seneviratne et al. 2021), including over the United States (Peterson et al. 2013; Wuebbles et al. 2014). However, multi-decadal trends of opposite sign can still occur at local scales (Fischer et al. 2013).

For precipitation extremes, models project that heavy precipitation events will become more frequent and intense in most regions globally in response to increasing greenhouse gases (Fischer et al. 2014; Pendergrass et al. 2017; Seneviratne et al. 2021). This is primarily due to increased water vapor in the atmosphere as a result of increased temperatures (e.g., Kunkel et al. 2013; Wehner 2013), as the increase in extreme precipitation with warming does not depend on the composition of the anthropogenic forcing causing that warming (e.g., Pendergrass et al. 2015; Li et al. 2021). There is greater agreement among models on this projection in the tropics and in mid-to-high latitudes, including over most of the contiguous United States (Janssen et al. 2014, 2016), and more uncertainty on the fringes of the subtropics, such as in southern North America (Sillmann et al. 2013). In terms of dry extremes, models project an increase in consecutive dry days in the subtropics, with much less model agreement elsewhere (Ukkola et al. 2020; Seneviratne et al. 2021). In North America, this is manifested as a lengthening of the dry

season in the southwestern United States and northern Mexico, with strong variability between extreme wet and dry periods (Pascale et al. 2016; Swain et al. 2018).

Uncertainty in future climate projections can be decomposed into three categories: scenario uncertainty, model uncertainty, and internal variability (Hawkins and Sutton 2009). Scenario uncertainty refers to the incomplete knowledge of future climate forcings, such as anthropogenic emissions of GHGs and aerosols, stratospheric ozone concentrations, and future land use changes. Model uncertainty refers to model-to-model differences in the responses to the same external forcing. These first two forms of uncertainty could potentially be reduced with better constraints on future emissions and improvements across climate models. This improvement, however, proves difficult in practice as, for instance, the range in equilibrium climate sensitivity (ECS) has not narrowed across model generations (Meehl et al. 2020; Zelinka et al. 2020).

The third type of uncertainty, internal variability, can be defined as the variability present in the climate system in the absence of external forcing. While internal variability is unforced, it can still manifest within long-term trends in climate variables. This long-term representation of internal variability can be thought as an 'irreducible' uncertainty that cannot be constrained through model improvements. Trends in some climate variables (such as precipitation) are much more sensitive to internal variability than others (such as temperature). As a result, forced trends in precipitation can be masked out by internal variability in future projections (Deser et al. 2012, 2014) and may not be distinguishable from internal variability until after 2100 in some regions of the United States (Giorgi and Bi 2009).

As the uncertainty driven by internal variability (intra-model variability) cannot be eliminated, and uncertainty driven by scenario uncertainty and model uncertainty (inter-model

variability) has not decreased across model generations, it is more accurate to communicate a range of possible future trends in a climate variable for a given region, rather than one specific value. One method by which to do this is a large initial-condition ensemble, in which one model is run many times with identical external forcing and with miniscule variance in initial conditions (see recent review by Deser et al. 2020). Through the use of this method, the mean response to the forcing across the ensemble can be thought of as the "forced response," while deviations from the mean response represent the internal variability within the ensemble. If multiple models run initial-condition ensembles, we can then get estimates of the uncertainty resulting from inter-model variability in the forced response (model uncertainty) as well as intra-model variability (represented through each model's internal variability). Likewise, varying the forcings within models would provide an estimate of scenario uncertainty.

Once the range of possible future trends in a climate variable is determined from global climate models, it is then worthwhile to understand the physical drivers that govern model-to-model variability and internal variability in the trends. One method by which to do this is the "storylines" approach of Zappa and Shepherd (2017) (see also Shepherd et al. 2018; Shepherd 2019; Zappa 2019; SG21). In this approach, physical drivers are first identified that can explain a large fraction of the variance in the future trends of a given climate variable. For example, Zappa and Shepherd (2017) identified the magnitude of tropical upper tropospheric warming and the strength of the stratospheric polar vortex as being key physical drivers that could explain inter-model variance in cold-season precipitation trends in the Mediterranean. Next, using linear regression, the sensitivity of the future trend of a given climate variable to the change in each physical driver is found. Finally, using these sensitivities, a regression model based upon various linear combinations of the physical drivers is used to construct possible high- and low-impact

future storylines for a given region (see section 3.4 for further details on this methodology). This method can be used to construct storylines based on physical drivers that are associated with scenario or model uncertainty (such as global mean near-surface air temperature [GMST] trends), physical drivers that are associated with common modes of internal variability (such as the Pacific–North America [PNA] pattern), or through a combination of both.

The purpose of this chapter is to document and understand the uncertainty in climate model projections of 21st century trends in mean and extreme temperature and precipitation for North America. The chapter is organized as follows. Section 3.2 describes the data and methods used in this study. Section 3.3 reviews the range of 21st century trends in mean and extreme temperature and precipitation indicated by climate models and assesses the relative roles of model uncertainty versus internal variability in the future trends. Section 3.4 then investigates the relevant physical drivers that contribute to the uncertainty in the future trends and uses the storylines approach to construct several high- and low-impact storylines for North America for the 21st century. Section 3.5 concludes with a summary and discussion of our results.

3.2 Data and Methods

The data source for this chapter is global climate model output from phase 6 of the Coupled Model Intercomparison Project (CMIP6; Eyring et al. 2016) under the SSP3-7.0 future emissions scenario (2015-2100). This scenario is a medium-to-high GHG emissions, high aerosol pathway that reaches a radiative forcing of 7.0 W m^{-2} greater than pre-industrial levels by the year 2100. We use this emissions scenario as it was requested to have the largest number of ensemble members per model of any 21st century scenario (O'Neill et al. 2016). For this chapter, we use all SSP3-7.0 ensemble members from models with at least five ensemble members. This

leads to a total of 248 simulations from 18 models for monthly-mean data and 192 simulations from 12 models for daily time-scale data (see list of all models in Table 3.S1). To assess trends in mean temperature and precipitation, we use monthly-mean data, and to assess trends in temperature and precipitation extremes, we use daily time-scale data.

We consider four measures of extreme temperature in this chapter: average heatwave duration, heatwave frequency, average cold snap duration, and cold snap frequency. We define heatwaves using the terrestrial heatwave definition from Perkins and Alexander (2013) as a period of time during which the daily maximum near-surface air temperature exceeds the climatological daily 90^{th} percentile for a minimum of 3 consecutive days. Here, we define the climatology using the first 30 years of each model simulation (2015–2044), as this climate is similar to the present climate and increases in heatwaves relative to this climate are thus societally relevant. The climatological 90^{th} percentile value for each calendar day is calculated using daily temperature within a 15-day window centered on that calendar day. This moving window allows a more robust estimate of percentile values as a result of an increased sample size within the climatology. Cold snaps are defined in the same manner as heatwaves, but for periods of time in which the daily minimum near-surface air temperature is less than the climatological 10^{th} percentile for at least 3 consecutive days. Note while terrestrial and marine heatwaves and cold snaps may co-occur, the physical processes governing them differ and thus must be considered separately (Pathmeswaran et al. 2022). In this chapter, we only consider terrestrial heatwaves and cold snaps.

We consider two measures of extreme precipitation in this chapter: annual 5-day maximum precipitation and maximum consecutive dry days. Annual 5-day maximum precipitation is defined as the largest 5-day sum of daily precipitation at each grid point during

each calendar year in each model simulation. Annual maximum consecutive dry days are defined as the most consecutive dry days (precipitation less than 1 mm day^{-1}) at each grid point during each calendar year in each model simulation.

After calculating 21st century mean and extreme temperature and precipitation trends for each model simulation, we decompose the variability in trends across model simulations using the method of SG21. Consider a quantity *X* (such as monthly-mean temperature) simulated by *m* different models, and let $\Delta X(m,n)$ be the 21st century (2015-2100) trend of the quantity *X* for ensemble member *n* of model *m*. We define the total forced trend in *X* for each model *m* as the mean trend in *X* across all ensemble members in model *m*, which we denote mathematically as $[\Delta X(m,:)]$. We linearly regress the total forced trend in *X*, $[\Delta X(m,:)]$, from all models onto the forced trends in GMST, $[\Delta GMST(m,:)]$, to obtain the component of the forced trend that scales linearly with GMST, $\Delta X_1(m,n)$, defined as:

$$\Delta X_1(m,n) = a + b * [\Delta GMST(m,:)] \quad (3.1)$$

where a and b are the y-intercept and slope of the regression, respectively.

The residual forced trend, or the component of the forced trend that does not scale linearly with GMST, is the full forced trend minus the quantity above:

$$\Delta X_2(m,n) = [\Delta X(m,:)] - \Delta X_1(m,n) \quad (3.2)$$

The component of the trend due to internal variability for each model simulation is thus the original trend, $\Delta X(m,n)$, minus the two components of the full forced trend:

$$\Delta X_{internal}(m,n) = \Delta X(m,n) - \Delta X_1(m,n) - \Delta X_2(m,n) \quad (3.3)$$

By taking the variance of these three quantities and comparing it to the total variance in the trend, we find the fraction of the variance that is attributed to each of these three quantities (see SG21 for further details).

Following the storyline approach applied in SG21, we also use a simple multiple linear regression model to assess if trends in common climatological modes of variability are physical drivers of 21st century trends in temperature and precipitation over North America. Following SG21, the indices we consider in this work are as follows:

1. El Niño –Southern Oscillation (ENSO), defined using the Niño-3.4 index: monthly mean sea-surface temperature averaged over 5°S-5°N, 120°W-170°W.
2. PNA, defined using the station-based index of Wallace and Gutzler (1981) based on the 500-hPa Z^* field (where Z^* is geopotential height with the zonal-mean removed)
3. East Pacific dipole (EP), defined using the station-based index of SG21 based on the difference in the 500-hPa Z^* field at two points (50°N, 140°W and 25°N, 122.5°W)
4. North Atlantic Oscillation (NAO), defined using the station-based index of Hurrell (1995) based on the sea-level pressure field.

While SG21 do not include the NAO, we include it here as we include eastern Canada in our analysis, which is a region in which the NAO has an established impact on temperature and precipitation (see Fig. 4c of Hurrell 1995 and Figs. 13, 16 of Hurrell et al. 2003).

In addition to these four indices, we also consider the role of inter-model differences in 21st century GMST trends (which are highly correlated with ECS) in driving variability in 21st century temperature and precipitation trends across model simulations. To ensure that trends in the four indices listed above are independent drivers and therefore uncorrelated with concurrent trends in GMST, we remove the component of the trend in each index that is linearly congruent with the GMST trend as follows:

$$\Delta y'(n) = \Delta y(n) - R * \Delta GMST(n) \tag{3.4}$$

where *n* represents each simulation in the analysis, $\Delta y'(n)$ is the residual trend in the index trend $\Delta y(n)$, and *R* is the slope of the linear regression of the full index trend onto the trend in GMST. Subsequently, the index trends $\Delta y'(n)$ can be decomposed into components associated with model-to-model differences (residual forced trends) and internal variability following Eq. 3.2 and 3.3.

3.3 Variability in 21st Century Mean and Extreme Temperature and Precipitation Trends for North America across CMIP6 Models

In this section, we document the range of 21st century trends in mean and extreme temperature and precipitation over North America from CMIP6 models and assess the relative roles of model uncertainty versus internal variability in the future trends. The purpose of this is twofold. First, it is worth knowing both the mean and variance of climate model projections, as the variance in these projections conveys uncertainty within the multi-model ensemble. Second, partitioning the variance via the method of SG21 (see section 3.2) allows one to know whether variability within the multi-model ensemble is the result of model-to-model differences (and therefore presumably constrainable), or due to internal variability (and therefore presumably irreducible).

3.3a Seasonal Mean Temperature and Precipitation

Figures 3.1c and 3.1d show the multi-model ensemble mean trend in seasonal-mean temperature over the 2015–2100 period for the SSP3-7.0 experiment for DJF and JJA, respectively. As expected, in the winter season, warming is maximized at high latitudes indicative of Arctic amplification as a result of increased GHG emissions. In summer, warming

is relatively weaker and more homogeneous across much of North America, with no Arctic amplification present.

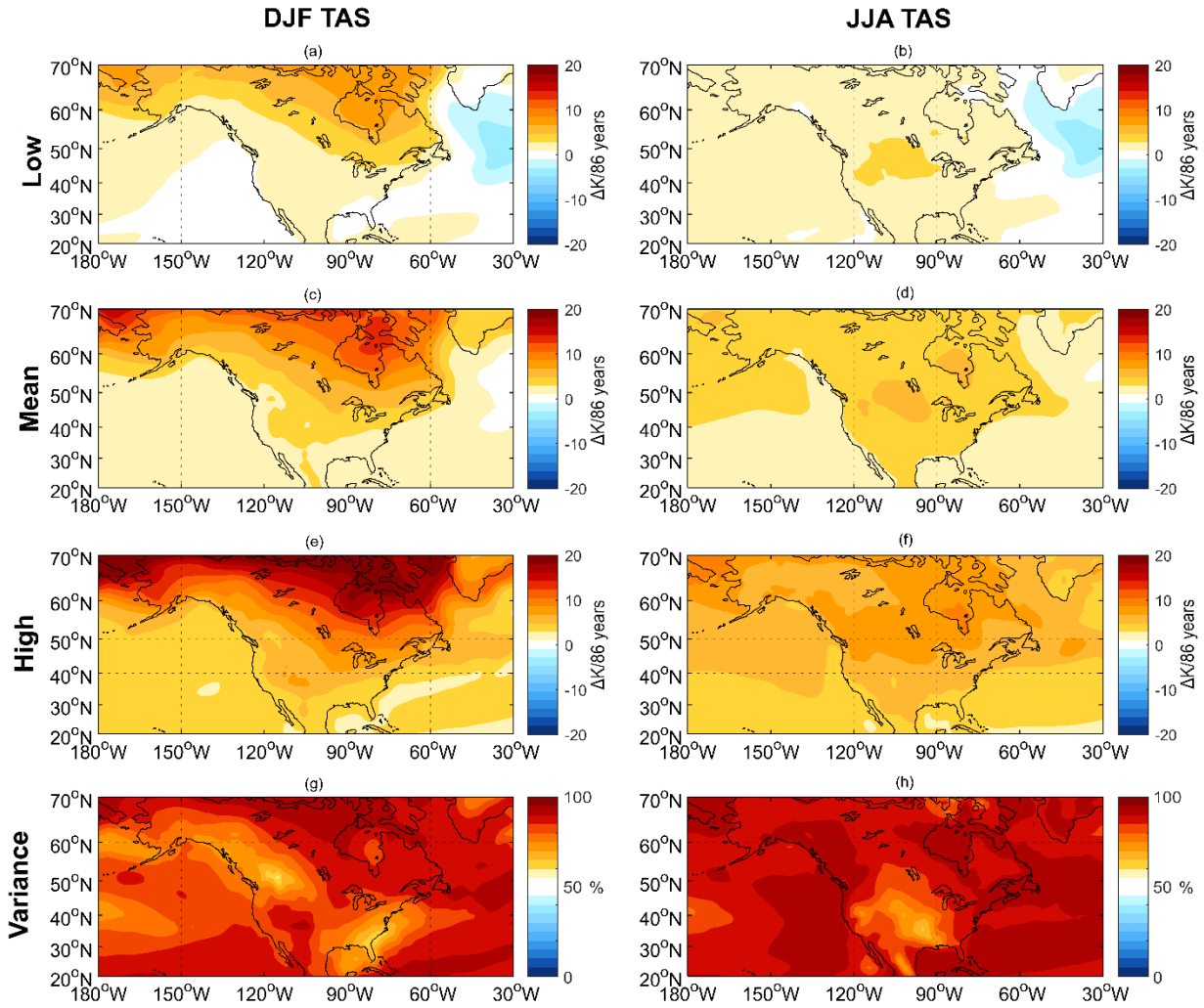

Figure 3.1 Trends in DJF (left column) and JJA (right column) seasonal-mean near-surface air temperature (TAS) for models under the SSP3-7.0 scenario from CMIP6. (c) and (d) show the multi-model ensemble mean TAS trends. (a) and (b) show the mean of the bottom 20% of modeled TAS trends on a grid point by grid point basis. (e) and (f) show the same as (a) and (b) but for the top 20% of modeled trends. (g) and (h) show the proportion of the variability in the modeled trends that is due to inter-model differences.

However, showing only the multi-model ensemble mean trends does not convey the range of 21st century trends displayed by individual model simulations. To do this, we show the

mean of the 0^{th}-20^{th} percentile of trends from individual model simulations (Figs. 3.1a-3.1b) and the mean of the 80^{th}-100^{th} percentile of trends from individual model simulations (Figs. 3.1e-3.1f) on a grid point by grid point basis. Note that because these figures are constructed on a grid point by grid point basis, the maps in these figure panels should *not* be seen as physical possibilities, as each individual grid point represents a potentially different subset of models. For reference, we also show the standard deviation of the trends across all model simulations in the supplementary material (Fig. 3.S1). It is important to note that, because of the differing number of ensemble members per model (Table 3.S1), our results could be skewed by a few models that have a greater number of ensemble members. However, we have repeated our analysis by limiting each model to only five members and confirmed that these (and subsequent) results are not sensitive to the varying number of ensemble members included for each model (not shown).

For winter mean temperature (Figs. 3.1a, 3.1e), the distribution in the trends across model simulations is primarily related to the degree of Arctic amplification (see also Fig. 3.S1a). The only location where the sign of the trend differs between the top and bottom 20^{th} percentiles of model simulations is in the North Atlantic, where different models possess different responses of the Atlantic Meridional Overturning Circulation (Bellomo et al. 2021). During summer months (Figs. 3.1b, 3.1f), the range in the trends across model simulations is smaller (see also Fig. 3.S1b).

Figures 3.1g and 3.1h show the proportion of the variance in trends across model simulations that can be attributed to model-to-model differences (see section 3.2 for methodology). Because the combination of the variance attributable to inter-model differences and intra-model differences (internal variability) by construction adds up to 100%, a grid point that is colored red can be thought of as a location where the variability in the trend across model

simulations is primarily the result of inter-model variability, and a grid point that is colored blue can be thought of as a location where the variability in the trend across model simulations is primarily the result of internal variability within models. Unsurprisingly, for both winter and summer, the majority of the variability in seasonal-mean temperature trends across simulations is related to inter-model variance, as the magnitude of seasonal-mean temperature trends in individual regions is generally larger in models with higher ECS. In DJF, while the variability in temperature trends at all locations in North America is dominated by inter-model differences, internal variability plays a relatively larger role in the Pacific Northwest and southeastern United States, two regions where the PNA is important in driving wintertime temperature variability both on monthly timescales (Leathers et al. 1991) and in terms of long-term trends (Deser et al. 2014). In JJA, internal variability plays a relatively larger role in temperature trends over the southern Great Plains (see also Fig. 6b of Deser et al. 2014).

In Fig. 3.2, we repeat the analysis from Fig. 3.1, but for the DJF and JJA trends in seasonal-mean precipitation. As expected, the multi-model ensemble mean shows wetting at high latitudes and drying in the subtropics. In DJF, meridional dipoles in precipitation trends, with wetting to the north and drying to the south, are evident over both the North Atlantic and North Pacific Oceans. The meridional dipole over the central Pacific is consistent with a poleward shift of the North Pacific extratropical storm track with climate change (e.g., Priestley and Catto, 2022). The meridional dipole over the North Atlantic is consistent with an increase in precipitation within North Atlantic extratropical cyclones (Michaelis et al. 2017; Sinclair et al, 2020), coupled with a reduction in extratropical storm track activity over the subtropical central North Atlantic (Priestley and Catto, 2022). Storm track precipitation trends are less evident in summer months, when the extratropical storm tracks are less active.

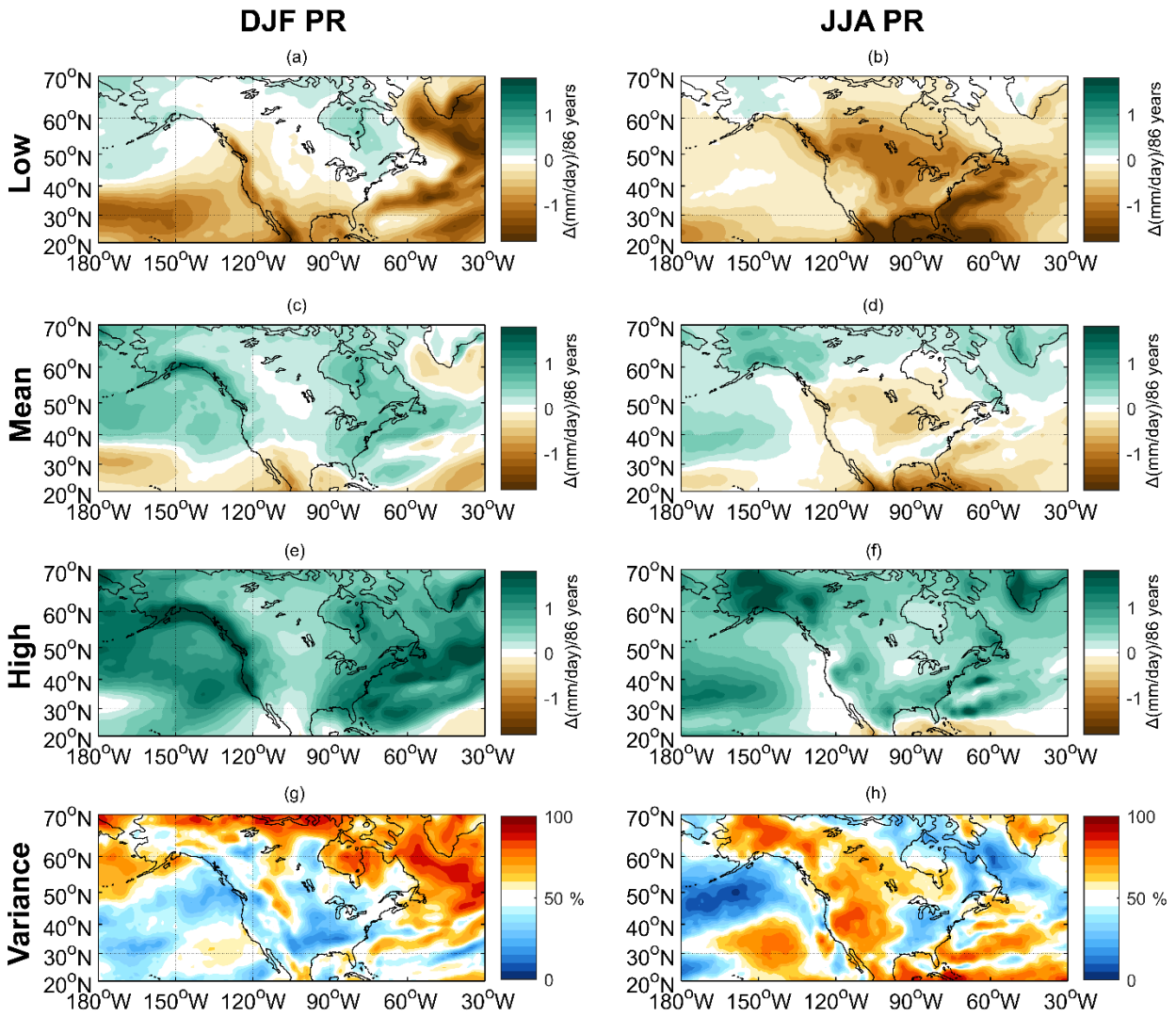

Figure 3.2 Same as Fig. 3.1, but for trends in seasonal mean precipitation (PR).

In contrast to the trends in seasonal-mean temperature where warming is projected by all simulations everywhere outside of the North Atlantic (Fig. 3.1), the seasonal-mean precipitation trends vary greatly among model simulations, such that 21st century drying and wetting trends are plausible throughout most of North America in both winter and summer (Fig. 3.2, first and third rows; see also Fig. 3.S2). For example, the models indicate that the southwestern United States, where future precipitation trends are particularly impactful due to its limited water resources, could experience large magnitude drying (Figs. 3.2a-b) or wetting (Figs. 3.2e-f) trends

over the 21st century, trends which are not evident from the relatively small multi-model ensemble mean trend (Figs. 3.2c-d). As for Fig. 3.1, the maps shown in the first and third rows of Fig. 3.2 should not be interpreted as physically consistent future scenarios, as they are intended to show the smallest and largest trends at each grid point.

In contrast to the range of trends in seasonal-mean temperature which is determined almost exclusively by model-to-model differences (Figs. 3.1g-h), much of the variability in seasonal-mean precipitation trends across model simulations is the result of internal variability (Figs. 3.2g-h). In DJF, the variability in precipitation trends across model simulations is dominated by internal variability over the North Pacific storm track and the contiguous United States and by inter-model differences over the North Atlantic storm track and Arctic (Fig. 3.2g). In JJA, the variability in precipitation trends across model simulations becomes more driven by model-to-model differences, particularly in the western United States and Canada (Fig. 3.2h). This is consistent with the recent finding of Grise (2022), who showed that, during JJA, models' representation of the present-day climatological atmospheric circulation over North America is closely linked to their projections of 21st century precipitation trends over the southwestern United States. However, internal variability remains the dominant factor in explaining the variance in summertime precipitation trends among model simulations in the southeastern and midwestern United States, consistent with the results of Lehner et al. (2020). Overall, these results suggest that 21st century summertime precipitation trends for North America may be able to be better constrained (such as by improving models' representation of the present-day climatological circulation), whereas large internal variability in precipitation trends during winter months would make tightly constraining these trends considerably more challenging.

3.3b Extreme Temperature and Precipitation

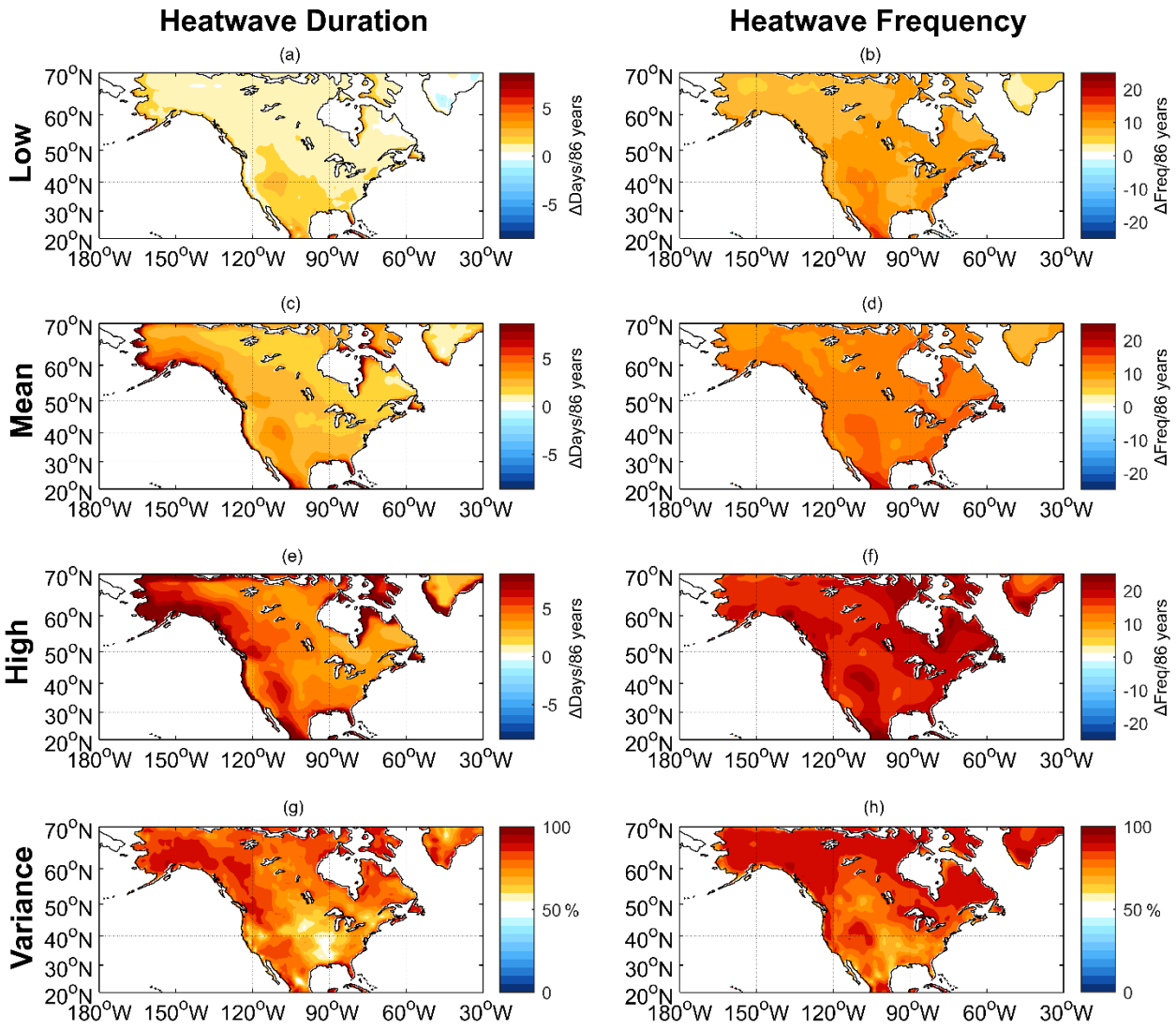

Figure 3.3 Same as Fig. 3.1, but for annual average heatwave duration (left column) and annual average heatwave frequency (events per year; right column) for a stationary climatology based on the first 30 years of each simulation's daily maximum near-surface temperature. Note that maritime grid points are excluded from this analysis.

We now repeat the results from Figs. 3.1–2, but for metrics of extreme temperature and precipitation. Figure 3.3 shows the trend in annual average heatwave duration (left column) and annual heatwave frequency (right column), where heatwaves are defined relative to a stationary

climatology of daily near-surface maximum temperature from the first 30 years of each model simulation (2015–2044). Note that, because heatwaves are defined relative to a stationary climate, maritime points trend towards a perpetual heatwave by the end of the century (Plecha and Soares 2020), leading to large trends in annual average heatwave duration. To focus on terrestrial heatwaves, we exclude maritime points from these maps, although their influence can be seen near the coasts, particularly in places like Florida and Alaska.

Relative to a stationary climatology, the average duration and frequency of heatwaves is projected to increase throughout North America in virtually all simulations (Fig. 3.3). The range in trends across model simulations is largest in western North America for heatwave duration and in Canada and Alaska for heatwave frequency (see also Fig. 3.S3). While inter-model differences still predominantly determine the range in trends in heatwave duration and frequency across model simulations, internal variability plays a larger role in the heatwave trends compared to the seasonal-mean temperature trends (compare Figs. 3.1g and 3.1h to Figs. 3.3g and 3.3h). Interestingly, if a centered-moving climatology is considered in place of a stationary climatology to define heatwaves, there is little-to-no trend in the average duration and frequency of heatwaves, with almost all variability in the trends across model simulations being the result of internal variability (Fig. 3.S4), a result consistent with Maher et al. (2021). This suggests that the increase in heatwave frequency and duration shown in Fig. 3.3 is because the background climate is warming, rather than because of a change in the character of the heatwaves themselves.

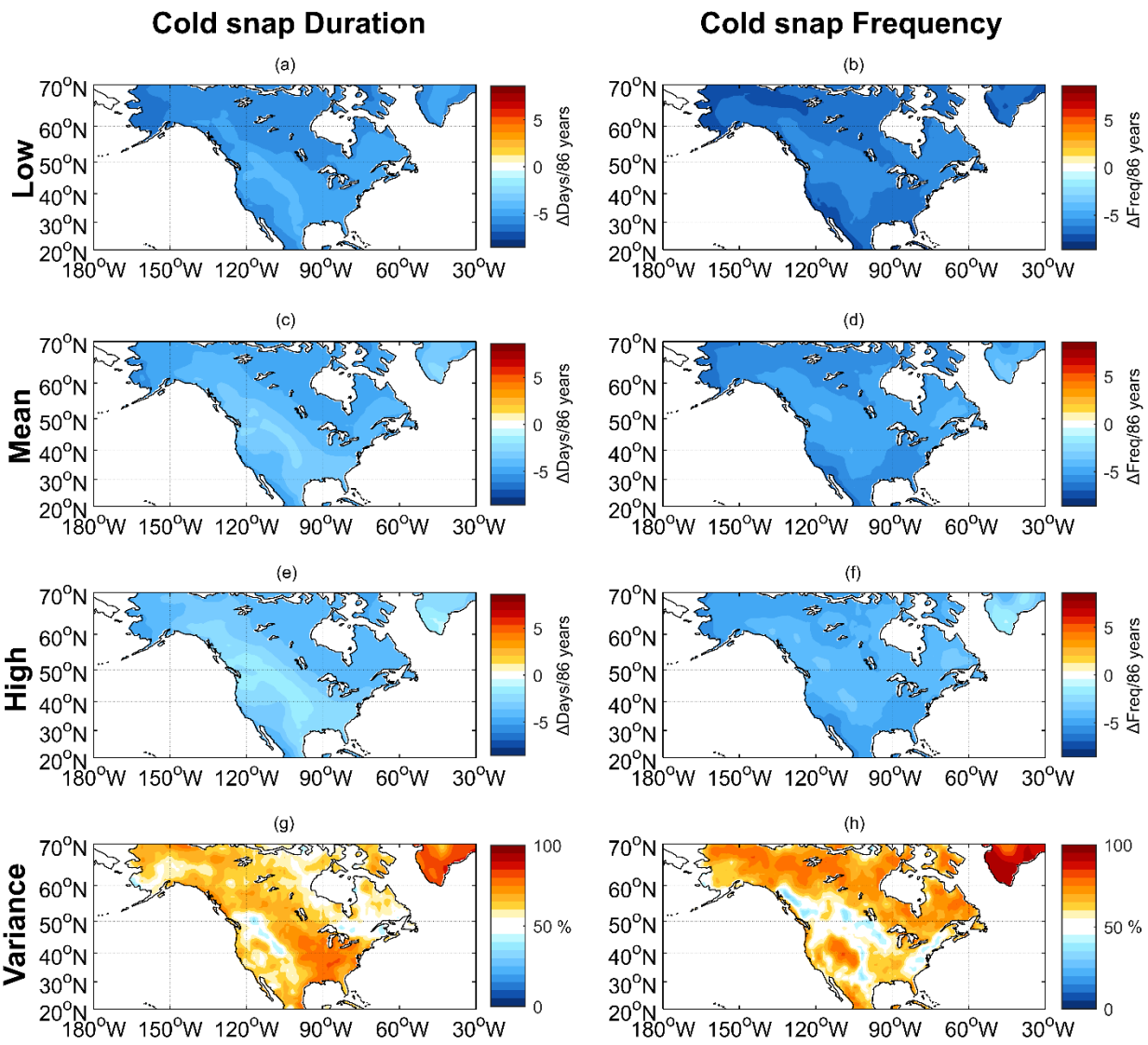

Figure 3.4 Same as Fig. 3.3, but for average annual cold snap duration (left column) and average annual cold snap frequency (right column). Note that maritime grid points are excluded from this analysis.

Figure 3.4 shows the trend in annual average cold snap duration (left column) and annual cold snap frequency (right column), where cold snaps are defined relative to a stationary climatology of daily near-surface minimum temperature from the first 30 years of each model simulation (2015–2044). The average duration and frequency of cold snaps is projected to decrease throughout North America in all simulations. The range in cold snap duration trends

across model simulations is largest over the United States and western Canada, whereas the range in cold snap frequency trends is similar over most regions of North America (see also Fig. 3.S5). As with the heatwave trends, the range in the trends in cold snap duration and frequency across model simulations is generally dominated by inter-model differences, but internal variability plays a greater role in the trends than for the seasonal-mean temperature (compare Figs. 3.1g and 3.1h to Figs. 3.4g and 3.4h). Furthermore, relative to the heatwave trends, internal variability generally plays a greater role in the cold snap trends, except over portions of the eastern United States (compare Figs. 3.3g and 3.3h to Figs. 3.4g and 3.4h). Finally, as for the heatwave trends, if a centered moving climatology is used to define cold snaps, there is little-to-no trend in cold snap duration or frequency, and the range in trends across model simulations is driven almost entirely by internal variability (Fig. 3.S6).

In terms of measures of extreme precipitation, we first show trends in the annual maximum number of consecutive dry days (days with less than 1mm day^{-1} of precipitation). Figure 3.5b shows the multi-model ensemble mean trend in consecutive dry days, where green (brown) shading represents a decrease (increase) in the maximum consecutive dry days. As expected from the seasonal mean wetting at high latitudes and drying in the subtropics (Fig. 3.2), there is a trend toward a reduction in consecutive dry days in the Arctic and an increase in consecutive dry days throughout much of the subtropics (see also Sillmann et al. 2013). However, there is little-to-no multi-model ensemble mean trend in maximum consecutive dry days throughout much of the continental midlatitudes, with the exception being from

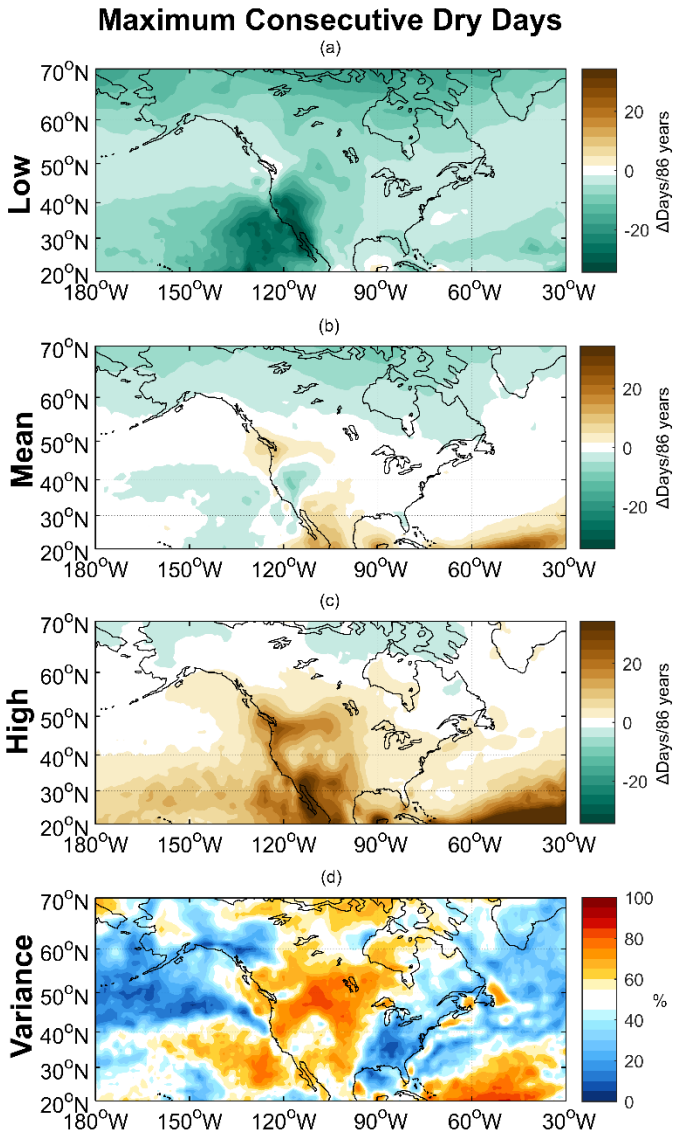

Figure 3.5 Same as Fig. 3.1, but for trends in the annual maximum number of consecutive dry days.

Mexico along the west coast of the United States. This region is also the region with the greatest variance in trends across the multi-model ensemble (Fig. 3.S7), with the mean of the top 20% of model trends at each grid point (Fig. 3.5c) showing large increases in the annual maximum consecutive dry days and the mean of the lowest 20% of model trends at each grid point (Fig. 3.5a) showing large reductions in the maximum consecutive dry days. In this region, the range in

the trends in consecutive dry days across the model simulations is predominantly the result of model-to-model differences (Fig. 3.5d), suggesting that either inter-model differences in ECS or other inter-model physical differences are responsible for the large variance in trends across model simulations. East of the Mississippi River, the range in the trends in consecutive dry days across model simulations is relatively small (compare Fig. 3.5a to 3.5c, see also standard deviation in Fig. 3.S7) and predominantly governed by internal variability (much like the seasonal-mean precipitation trends in Fig. 3.2).

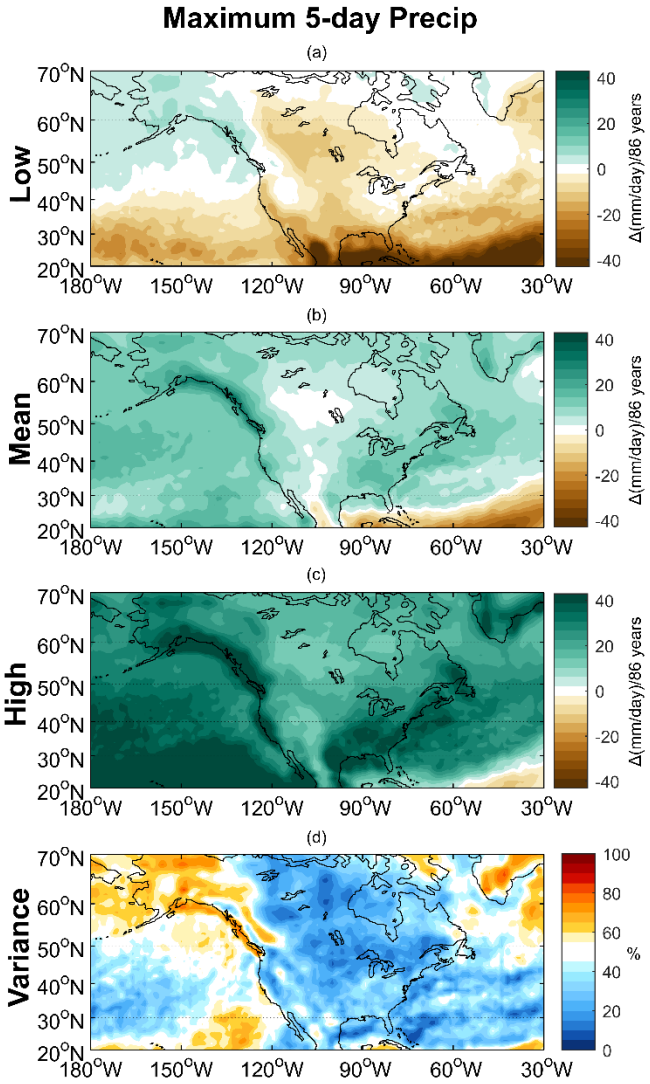

Figure 3.6 Same as Fig. 3.1, but for trends in annual 5-day maximum precipitation.

Figure 3.6 shows the trends in the annual maximum 5-day sum of daily precipitation. Similar to the mean trends in winter precipitation (Fig. 3.2c), in the multi-model ensemble mean, there is an increase in maximum precipitation at mid- and high latitudes and a decrease in maximum precipitation in the subtropics over Mexico and the Atlantic (Fig. 3.6b). However, there is a wide distribution in the trends in maximum precipitation across model simulations, with trends toward an increase or decrease in maximum precipitation possible across most of North America (Figs. 3.6a and 3.6c, see also standard deviation in Fig. 3.S8). The only region where trends toward an increase in maximum 5-day precipitation are consistently positive across model simulations is in Alaska, which is also the only region where the variability in trends across the multi-model ensemble is dominated by inter-model differences as opposed to internal variability (Fig. 3.6d). Along the coastline in the Gulf of Alaska, where the variability in trends is large (Fig. 3.S8), the variability is associated with model-to-model differences not linearly related to GMST (not shown), suggesting that the way in which different models resolve this mountainous coastline may be contributing to the differences in trends.

In contrast to extreme temperature for which differences in trends across model simulations are primarily attributable to inter-model differences (Figs. 3.3-4, bottom row), differences in trends in maximum precipitation across North America are dominated by internal variability (Fig. 3.6d). This suggests that further constraining projections of changes in extreme precipitation will be challenging, as the primary source of uncertainty is internal variability. This is not to say, however, that well-documented increases in extreme precipitation across the United States (e.g., Janssen et al. 2014, 2016) are not related to GMST increases, but that the spread in model projections is more a function of internal variability than inter-model differences.

3.4 Dynamical Drivers of Variability in Mean and Extreme Temperature and Precipitation Trends for North America across CMIP6 Models

In section 3.3, we documented how CMIP6 model simulations produce widely variable 21st century mean and extreme temperature and precipitation trends for North America (even when forced by the same emissions scenario) and attributed this variability to a combination of inter-model differences and internal variability. In this section, we now investigate some of the potential dynamical drivers responsible for this variability in trends across model simulations.

3.4a Identifying the dynamical drivers

To identify relevant dynamical drivers, we first regress the 21st century trends in mean and extreme temperature and precipitation from all model simulations (as documented in section 3.3) against trends in GMST and four common indices of North American climate variability (ENSO, PNA, EP, and NAO) using a multiple linear regression model. Specifically, we fit the 21st century trend in a quantity *X* at each grid point from model simulation *n* as follows:

$$\Delta X(n) = a + b_1 \Delta GMST(n) + b_2 \Delta ENSO(n) + b_3 \Delta PNA(n) + b_4 \Delta EP(n) + b_5 \Delta NAO(n) \quad (3.5)$$

where a and $b_{1\text{-}5}$ are the y-intercept and regression coefficients, respectively. Recall that the GMST trend has been linearly removed from the trends in the other four indices prior to constructing this regression model (see section 2). The top row of Fig. 3.7 illustrates how much of the variance in the trends of three example fields (DJF mean temperature, DJF mean precipitation, and annual consecutive dry days) across model simulations can be captured by this regression model. For brevity, we only discuss this representative sample of fields in the

remainder of this section, with results for the remainder of the fields shown in the supplementary material (Fig. 3.S12-S13).

Based upon this regression model, we can then identify the key drivers responsible for the variability in trends $\Delta X(n)$ across model simulations. Ordinary least squares (OLS) regression models create a linear function of a set of explanatory variables by minimizing the sum of squares between the observed dependent value and those predicted by the linear function (sum of squared errors; SSE). This is mathematically equivalent to maximizing the regression sum of squares (SSR), the squared distance between the predicted dependent variable and the mean observed dependent variable (e.g., Wilks 2006). From this, the coefficient of determination, R^2, is defined as follows:

$$R^2 = 1 - \frac{SSE}{SST} = \frac{SSR}{SST} = \frac{\sum_{i=1}^{n}(\hat{y}_i - \bar{y})^2}{\sum_{i=1}^{n}(y_i - \bar{y})^2} \tag{3.6}$$

where SST is the total sum of squares, y_i is the ith value of the observed dependent variable, $\hat{y}_i$ is the ith value of the predicted dependent variable from the regression, and $\bar{y}$ is the mean of the observed dependent variable.

This means that SSR can be thought of as the amount of the SST that is explained by the OLS regression model. Therefore, increases in SSR from the addition of another independent variable into the regression model are the additional SST explained by the addition of that variable, also known as the extra sum of squares (Draper and Smith 1998). For example, for a multiple linear regression model with two predictors (x_1 and x_2), the increase in R^2 from the addition of the second predictor, x_2, is calculated as follows:

$$R^2_{(x_2|x_1)} = \frac{SSR_{(x_1,x_2)}}{SST} - \frac{SSR_{(x_1)}}{SST} \tag{3.7}$$

where $R^2_{(x_2|x_1)}$ is the increase in R^2 in the regression model including x_2 given that x_1 was previously included in the model, $SSR_{(x_1,x_2)}$ is the regression sum of squares for the regression

model containing both x_1 and x_2, and $SSR_{(x_1)}$ is the regression sum of squares for the regression model containing only x_1. Through this method, we can isolate the dynamical drivers that play a key role in driving the variance in the mean and extreme temperature and precipitation trends. Additionally, because the extra sum of squares is calculated through the addition of a predictor compared to the regression model including all but that predictor, the added value of each predictor is from the variability in that predictor that is not covariable with the other predictors.

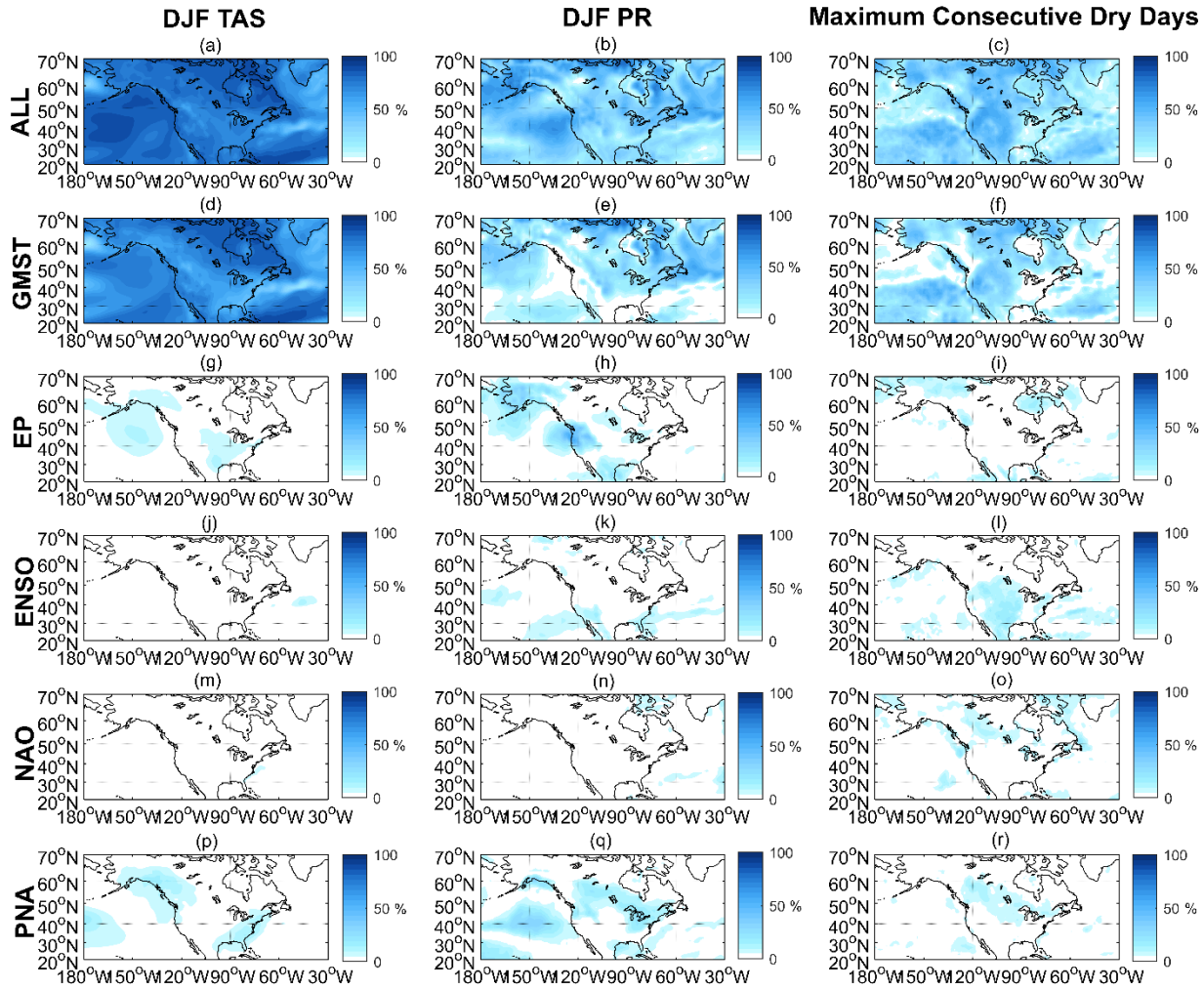

Figure 3.7 (top row) R^2 from multiple linear regression model (eq. 3.5) predicting trends in DJF mean temperature (left column), DJF mean precipitation (middle column), and annual maximum consecutive dry days (right column). (rows 2-6) Extra R^2 gained from the addition of a single index compared to a multiple linear regression model that does not include that single index.

In the second through sixth rows of Fig. 3.7, we show the added R^2 provided by each dynamical driver into the multiple linear regression model (Eq. 3.5). To calculate the added R^2 value for a particular dynamical driver, we compare the R^2 value from a regression model with all five predictors to that of a regression model with only four predictors (i.e., without that one particular dynamical driver). As in the top row of Fig. 3.7, results are shown for three example fields, with the remainder of the fields shown in the supplementary material (Figs. 3.S12-S13).

The left column of Fig. 3.7 shows the R^2 values for the multiple linear regression model in explaining the variance in the DJF monthly mean surface temperature trends across model simulations. Recall from Fig. 3.1g that the variance in surface temperature trends across model simulations is almost entirely due to model-to-model differences (likely due to differences in ECS among models), with internal variability explaining more of the variance in the Pacific Northwest and American Southeast in a pattern reminiscent of the PNA. Figure 3.7 confirms that variability in model trends in GMST do in fact explain the majority of variability in North American DJF mean surface temperature trends (Fig. 3.7d) and, as expected, the dynamical driver that explains the second-most variability in DJF temperature trends in the Pacific Northwest and Southeast is the PNA (Fig. 3.7p). Consistent with results from previous studies (e.g., Deser et al. 2014), the majority of this variance explained by the PNA is due to internal variability, rather than model-to-model differences that are independent of GMST trends (Fig. 3.S9).

The middle column of Fig. 3.7 shows the R^2 values for the multiple linear regression model in explaining the variance in the DJF monthly mean precipitation trends across model simulations. Note that the regression model captures less of the total variance in the trends across model simulations for precipitation than for temperature (Fig. 3.7b compared with 3.7a).

Variability in model trends in GMST explain the majority of variability in DJF mean precipitation trends at higher latitudes (Fig. 3.7e; see also Fig. 3.2g). However, as described in SG21, trends in GMST play little role in driving variability in DJF mean precipitation trends over the western United States, with the variability of this region being more driven by modeled trends in EP (Fig. 3.7h) and ENSO (Fig. 3.7k). We find that internal variability in EP trends and model-to-model differences in ENSO trends are the primary drivers of the variability of precipitation trends in this region (Fig. 3.S10). Therefore, reducing inter-model differences in how ENSO responds to anthropogenic forcing over the 21st century may be helpful in reducing uncertainty in future wintertime precipitation trends in the western United States, but some uncertainty will always exist due to internal variability (such as future trends in EP and, to a lesser extent, PNA).

Finally, the right column of Fig. 3.7 shows the R^2 values for the multiple linear regression model in explaining the variance in the trends in maximum annual consecutive dry days across model simulations. Here, we find that, for the western United States (the region that has the largest variance in trends across model simulations; Fig. 3.5), the primary drivers of the variance in the consecutive dry day trends are GMST (Fig. 3.7f) and ENSO (Fig. 3.7l). As for seasonal precipitation trends, the majority of the variance explained by ENSO is due to model-to-model differences that are independent of GMST trends (Fig. 3.S11), rather than internal variability. This result is consistent with model-to-model differences explaining the majority of the variance in trends in consecutive dry days across model simulations over the western United States (Fig. 3.5d).

3.4b Constructing Storylines

To illustrate the results from Fig. 3.7, we can now construct storylines that outline the range of plausible outcomes, as simulated across CMIP6 models. Following prior work (Zappa and Shepherd 2017; SG21), we estimate the combined influence of two dynamical drivers on trends in mean and extreme temperature and precipitation as follows. For a trend in variable *X* influenced by dynamical drivers y_1 and y_2, four storylines can be constructed based on combinations of low (20th percentile across the model ensemble) and high (80th percentile across the model ensemble) trends in the dynamical drivers. For example, a "high y_1, high y_2" storyline would be calculated as follows:

$$\Delta X = \Delta X_{mean} + \alpha_{y_1}\left(\Delta y_{1_{80}} - \Delta y_{1_{mean}}\right) + \alpha_{y_2}\left(\Delta y_{2_{80}} - \Delta y_{2_{mean}}\right) \quad (3.8)$$

where α_{y_1} is the slope of the linear regression of the trend in *X* at a particular grid point onto the trend in y_1, $\Delta y_{1_{80}}$ is the 80th percentile y_1 trend across the model ensemble, and $\Delta y_{1_{mean}}$ is the mean of the trend in y_1 across all members within the ensemble.

As a demonstration, we first show a set of storylines for 21st century trends in DJF mean surface temperature across North America. As we have shown previously (Fig. 3.7), the two dynamical drivers that play the largest role in explaining the variability in DJF mean surface temperature trends across North America are trends in GMST and the PNA. We further showed that, for the PNA, it is the internal variability of the modeled PNA trends that explains a larger portion of variability in modeled DJF temperature trends, as opposed to model-to-model differences (Fig. 3.S9). To that end, we construct storylines using two dynamical drivers, GMST trends and the internal variability component of PNA trends.

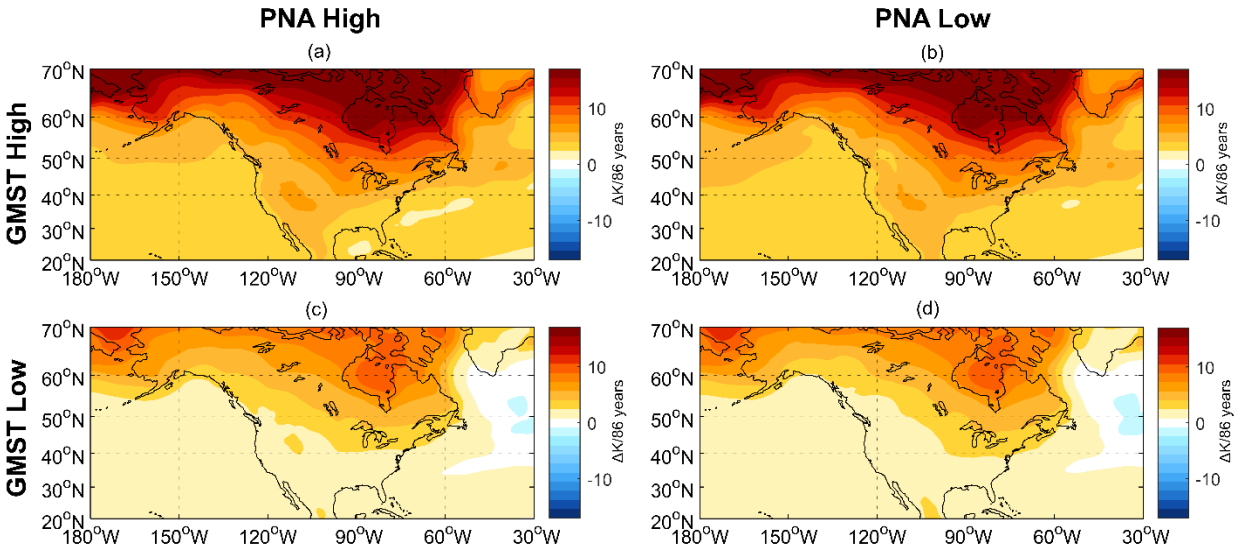

Figure 3.8 Storylines for DJF mean temperature trends, spanning the CMIP6 model phase space of possible global mean surface temperature trends and trends due to internal variability in the PNA.

Figure 3.8 shows the four storylines constructed from the two dynamical drivers. The rows and columns can be thought of as representative of the domain covered by storylines, with the top (bottom) row showing storylines constructed with the high (low) trend in GMST and the left (right) column showing storylines constructed with the high (low) trend in the PNA pattern. As one may expect from Fig. 3.7, much of the variability in DJF temperature trends across model simulations is explained by GMST trends (compare top and bottom rows of Fig. 3.8). Models that have higher GMST trends tend to have much larger warming trends across North America, particularly in high latitudes as a result of Arctic amplification. As this variability in trends across model simulations is closely related to model climate sensitivity, it could presumably be narrowed with constraints on ECS. Although CMIP6 models contain a larger spread in ECS when compared to CMIP5 models (Zelinka et al. 2020), extreme values of ECS are thought to be unlikely as a result of observational constraints (Sherwood et al. 2020; McCoy et al. 2022). However, the variability across the phase space in the modeled PNA trends (compare left and

right columns of Fig. 3.8) is much more difficult to constrain, as it is the result of internal variability within the models. Consequently, projections of DJF warming for regions where differences between the PNA-high and PNA-low storylines are non-negligible (such as the Pacific Northwest) will remain more uncertain, even with strong constraints on ECS.

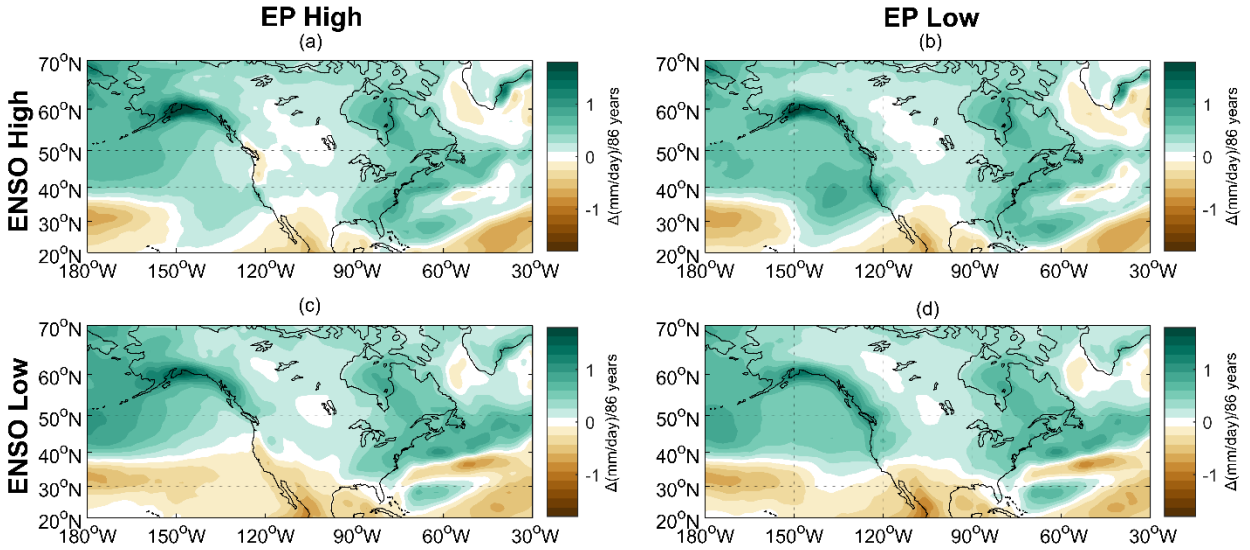

Figure 3.9 Storylines for DJF mean precipitation trends spanning the CMIP6 model phase space of possible residual forced trends in ENSO and trends due to internal variability in EP.

We next show a set of storylines for 21st century trends in DJF mean precipitation across North America in Fig. 3.9. Because the dynamical drivers associated with variability in winter-time precipitation trends vary across different regions of the continent (Fig. 3.7), we focus here, for example's sake, on the two physical drivers most relevant for the trends in the western United States: inter-model differences in ENSO trends and internal variability in the EP trends (see Fig. 3.S10). In Fig. 3.9, all four storylines have similar broad patterns of projected DJF precipitation changes, with wetting in the high latitudes and drying in the subtropics. However, on closer inspection, the storylines differ in some key respects. First, while wetting is expected along the Alaskan coast in all four storylines, the magnitude of the wetting is increased in EP-high

storylines. Additionally, EP-low storylines have broad wetting across the Pacific Northwest and Northern California, while EP-high storylines have either drying trends or trends that are less than the ensemble mean (compare with Fig. 3.2c).

The result in Fig. 3.9 is very similar to Fig. 7 of SG21 but differs in that SG21 only creates storylines based on dynamical drivers and does not decompose them into components due to model-to-model differences and internal variability. The advantage of our approach here is that it informs whether aspects of the storylines are potentially constrainable (i.e., the result of model-to-model differences) or not constrainable (i.e., the result of internal variability). In Fig. 3.9, because these storylines are constructed with the model-to-model differences in ENSO, variability within the storylines across the phase space of ENSO trends (top vs. bottom row) is presumably constrainable. For a region such as Southern California, this suggests that were an ENSO-high storyline to be 'correct,' they could likely expect wetter winters in the future (Fig. 3.9, top row), while if an ENSO-low storyline were 'correct', a small drying trend in wintertime

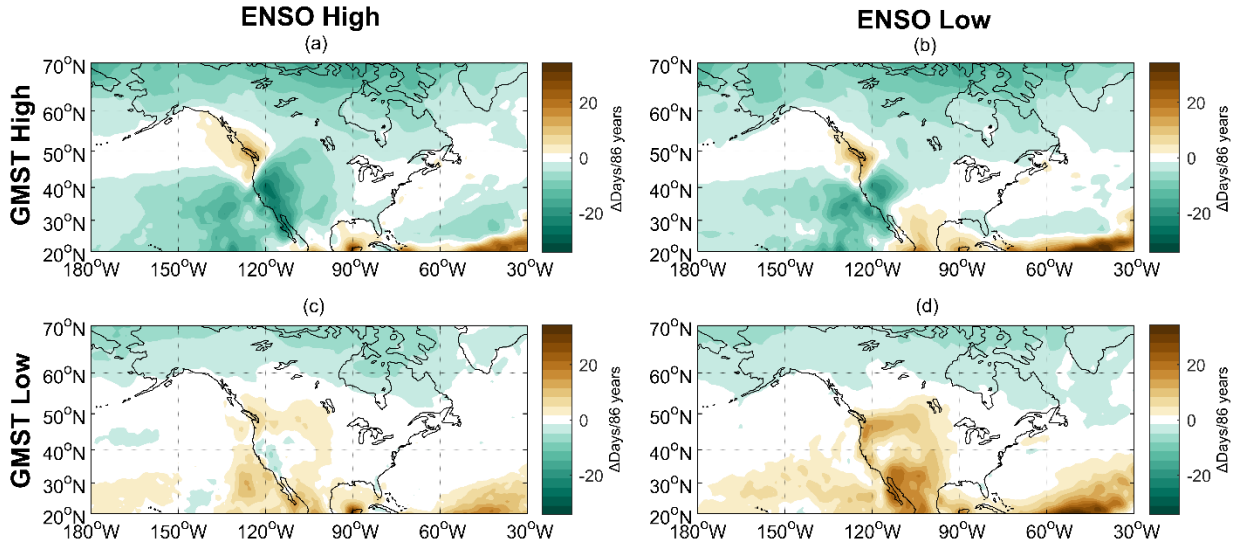

Figure 3.10 Storylines for annual maximum consecutive dry day trends spanning the CMIP6 model phase space of possible global mean surface temperature trends and residual forced trends in ENSO.

precipitation or little-to-no trend would be expected. As future precipitation trends in some regions of North America are closely tied to the models' present-day climatological atmospheric circulation (Grise 2022), reducing the model ensemble to better represent the current climate may also help to constrain which of these storylines are more plausible than others.

Lastly, we construct a set of storylines for 21st century trends in annual maximum consecutive dry days across North America in Fig. 3.10. Here, the two dynamical drivers used to construct the storylines are GMST trends and model-to-model differences in ENSO trends (Fig. 3.7; Fig. 3.S11). In this figure, the most notable differences among storylines occur in the western United States (see also Fig. 3.5). In this region, models that have high trends in GMST and ENSO experience a reduction in annual maximum consecutive dry days over the course of the 21st century (Fig. 3.10a). While the size of the ENSO trend does play a role in the magnitude of the change in annual consecutive dry days over the 21st century (Fig. 3.10, left vs. right column), the sign of the change is determined predominantly by the GMST trend (Fig. 3.10, top vs. bottom row). Note that, because both dynamical drivers on this figure are associated with model-to-model differences in future trends, internal variability is a not a leading factor in the storylines shown in Fig. 3.10. Consequently, the range in storylines in consecutive dry day trends illustrated in Fig. 3.10 may be able to be significantly narrowed with constraints on ECS and if there are any significant future constraints on the model response of ENSO to anthropogenic forcing.

To illustrate how the range in storylines may be able to be narrowed with constraints on ECS, in Fig. 3.11, we repeat the analysis from Fig. 3.10, but only with models that have ECS within the observationally constrained range (2.13-4.12K) found by recent studies (Sherwood et al. 2020; McCoy et al. 2022). In this set of storylines, as a result of the removal of unreasonably

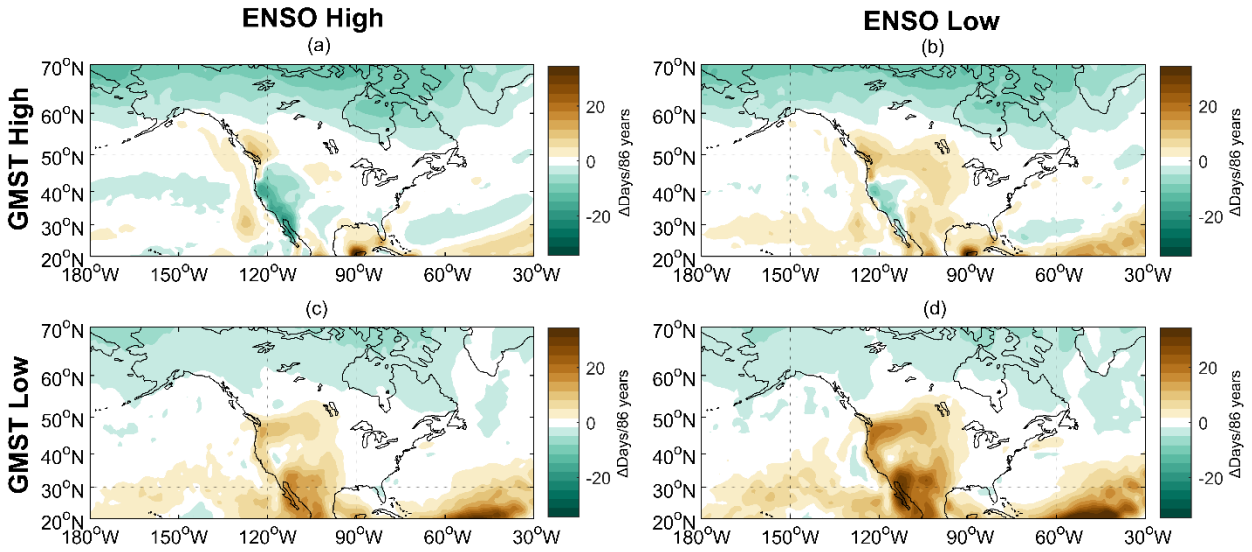

Figure 3.11 Same as Fig. 3.10, but for a constrained set of models based on the likely range of ECS given observational constraints from McCoy et al. (2022). Model values of ECS are taken from Meehl et al. (2020).

high ECS models, decreasing trends in annual maximum consecutive dry days are greatly reduced in the high GMST trend storylines (compare top row of Fig. 3.11 with top row of Fig. 3.10).

3.5 Conclusions

Projections of 21st century trends in mean and extreme temperature and precipitation for North America vary widely across CMIP6 models, even if they are forced by identical anthropogenic emissions. Hence, examining only the multi-model mean future projection obscures large uncertainties in future regional climate. In this chapter, we not only examine the multi-model mean trends under a moderate-to-high future emissions scenario (SSP3-7.0), but also the spread in trends across model simulations for a range of variables quantifying mean and extreme temperature and precipitation over North America: monthly-mean temperature and precipitation, heatwave and cold snap frequency and duration, annual maximum consecutive dry

days, and annual maximum 5-day cumulative precipitation. We attribute the spread in trends across model simulations to either model-to-model differences, which can presumably be reduced if models are improved, or internal variability, for which the uncertainty is largely irreducible. While the range in regional mean temperature trends across model simulations is largely due to model-to-model differences in ECS (Figs. 3.1g, 3.7d), internal variability plays a relatively greater role in the future trends of extreme temperature (bottom row of Figs. 3.3–3.4). Furthermore, while model-to-model differences primarily govern the spread in mean and extreme temperature trends across model simulations, the spread in mean and extreme precipitation trends is dominated by internal variability in many regions (bottom row of Figs. 3.2, 3.5, and 3.6).

We then seek to understand the physical drivers responsible for the spread in mean and extreme temperature and precipitation trends across the CMIP6 model simulations. Key drivers identified include model-to-model differences in GMST warming (i.e., climate sensitivity), model-to-model differences in the response of ENSO to anthropogenic forcing, and the future evolution of modes of internal variability (such as the PNA and EP teleconnection patterns). The most important drivers are GMST warming and the PNA for winter-time mean temperature trends in the Pacific Northwest and American Southeast (Fig. 3.7, left; Fig. 3.8), ENSO and EP for western North American mean precipitation trends in winter (Fig. 3.7, middle; Fig. 3.9), and GMST warming and ENSO for extreme drying trends across southwestern North America (Fig. 3.7, right; Fig. 3.10). Although internal variability will always introduce a level of uncertainty into future projections that cannot be reduced, the spread in CMIP6 projections attributable to model-to-model differences is presumably reducible. As an example, we show how existing observational constraints on ECS can be used to reduce the spread in plausible future trends in

extreme precipitation over the American West (Fig. 3.11). If similar observational constraints were established for the response of ENSO to anthropogenic forcing, they could similarly be used to further constrain model projections.

One caveat to this study is that it assumes that the models' internal variability is representative of the actual internal variability present in the observed climate. While CMIP6 single model initial condition ensembles have been shown to adequately estimate the internal variability in GMST (Suarez-Gutierrez et al. 2021), some models have biases in their representation of internal variability at regional scales. For example, one commonly used single model initial condition ensemble is known to overestimate the internal variability in regional temperature and precipitation trends over western North America (McKinnon and Deser 2018; Deser et al. 2020).

The results of this chapter illustrate that regional climate prediction using the current generation of climate models is complicated by uncertainties arising from both model-to-model differences and internal variability, with model-to-model differences playing a greater role for some variables (such as mean and extreme temperature) and in some regions (such as the western United States). Identifying variables, regions, and seasons for which the spread in future trends across model simulations is dominated by model-to-model differences (such as is done here) is a useful first step that can help to prioritize areas of focus where the range in model projections can potentially be narrowed with future model improvements. Additional work is needed to better understand the drivers responsible for model-to-model differences in future trends and to establish any potential observational constraints for these processes.

3.6 Supplemental Information

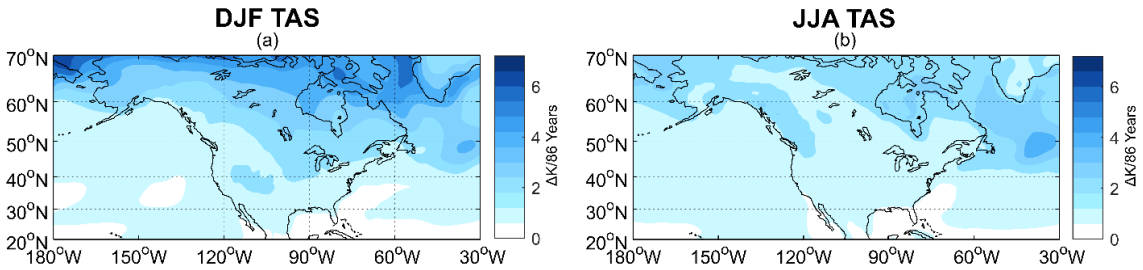

Figure 3.S1. Standard deviation in trends of monthly-mean near-surface air temperature (TAS) for DJF (a) and JJA (b).

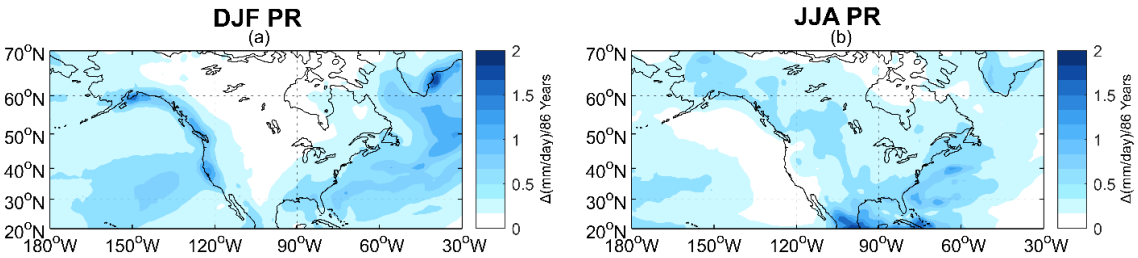

Figure 3.S2. Same as Fig. 3.S1 but for monthly-mean precipitation (PR).

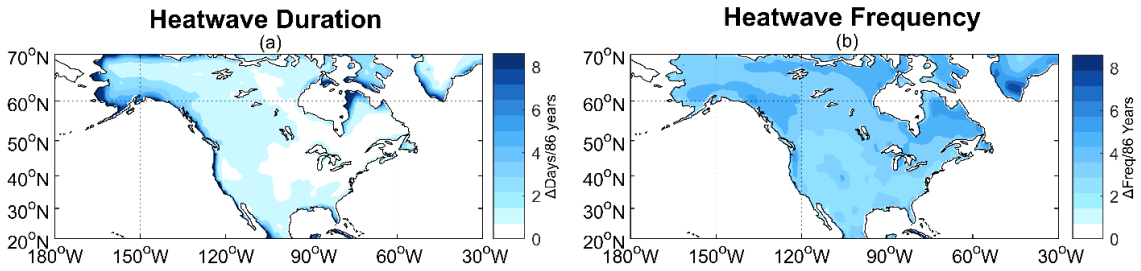

Figure 3.S3. Same as Fig. 3.S1 but for standard deviation in model trends in annual average heatwave duration (a) and annual heatwave frequency (b). Note that maritime grid points are excluded.

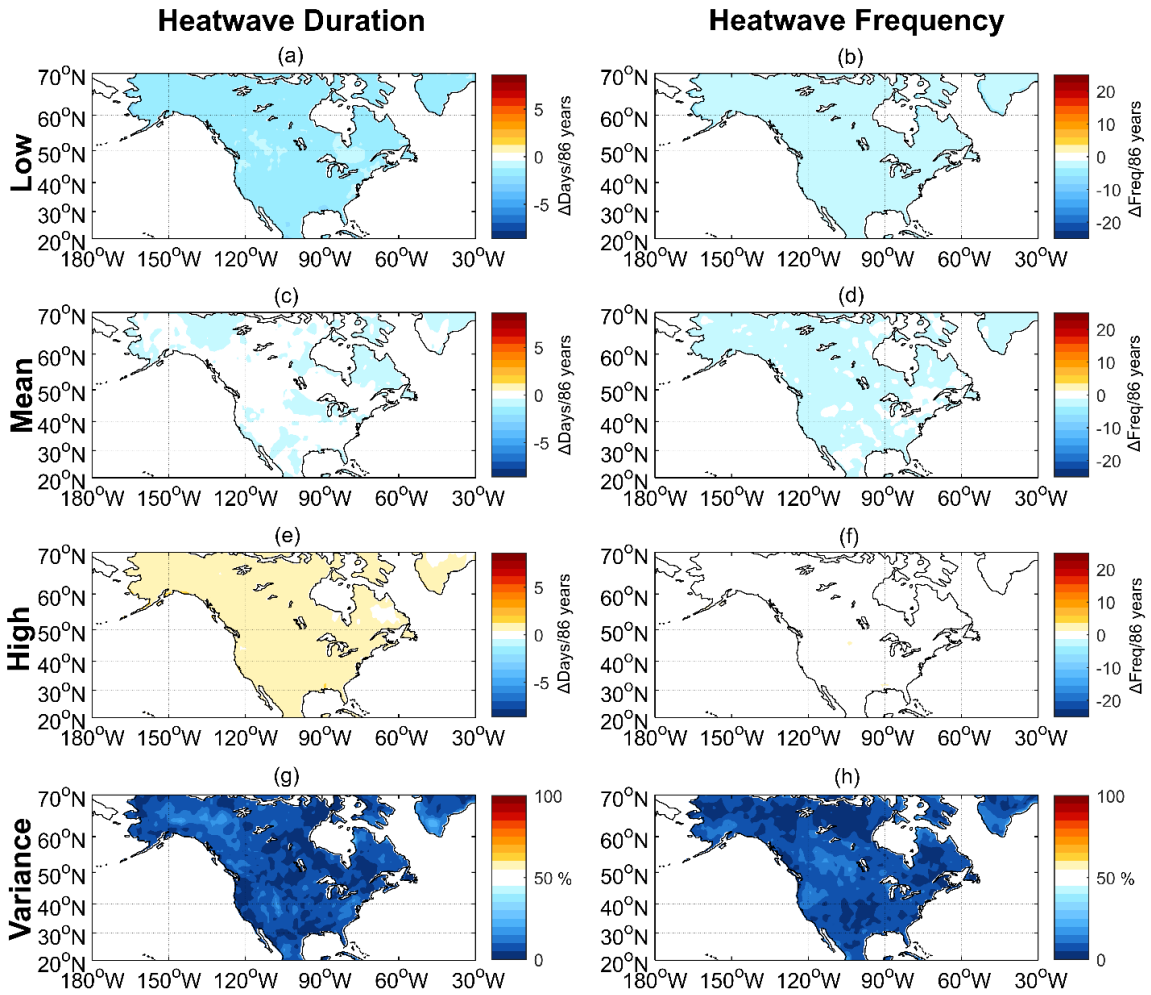

Figure 3.S4. Trends in annual average heatwave duration (left column) and annual heatwave frequency (right column) for a centered, moving climatology of daily maximum temperature. (c) and (d) show the multi-model ensemble mean trends in heatwave duration and frequency. (a) and (b) show the mean of bottom 20% of modeled trends in heatwave duration and frequency. (e) and (f) show the same as (a) and (b) but for the top 20% of modeled trends. (g) and (h) show the proportion of the variability in the modeled trends that is due to inter-model differences. Note that maritime grid points are excluded.

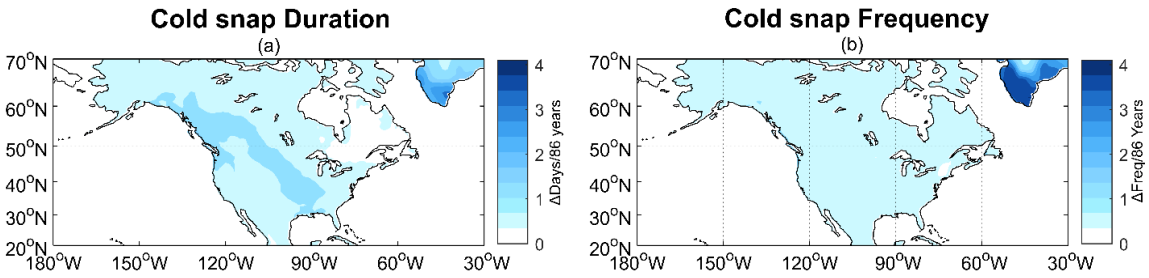

Figure 3.S5. Same as Fig. 3.S3 but for standard deviation in trends in annual average cold snap duration (a) and annual cold snap frequency (b).

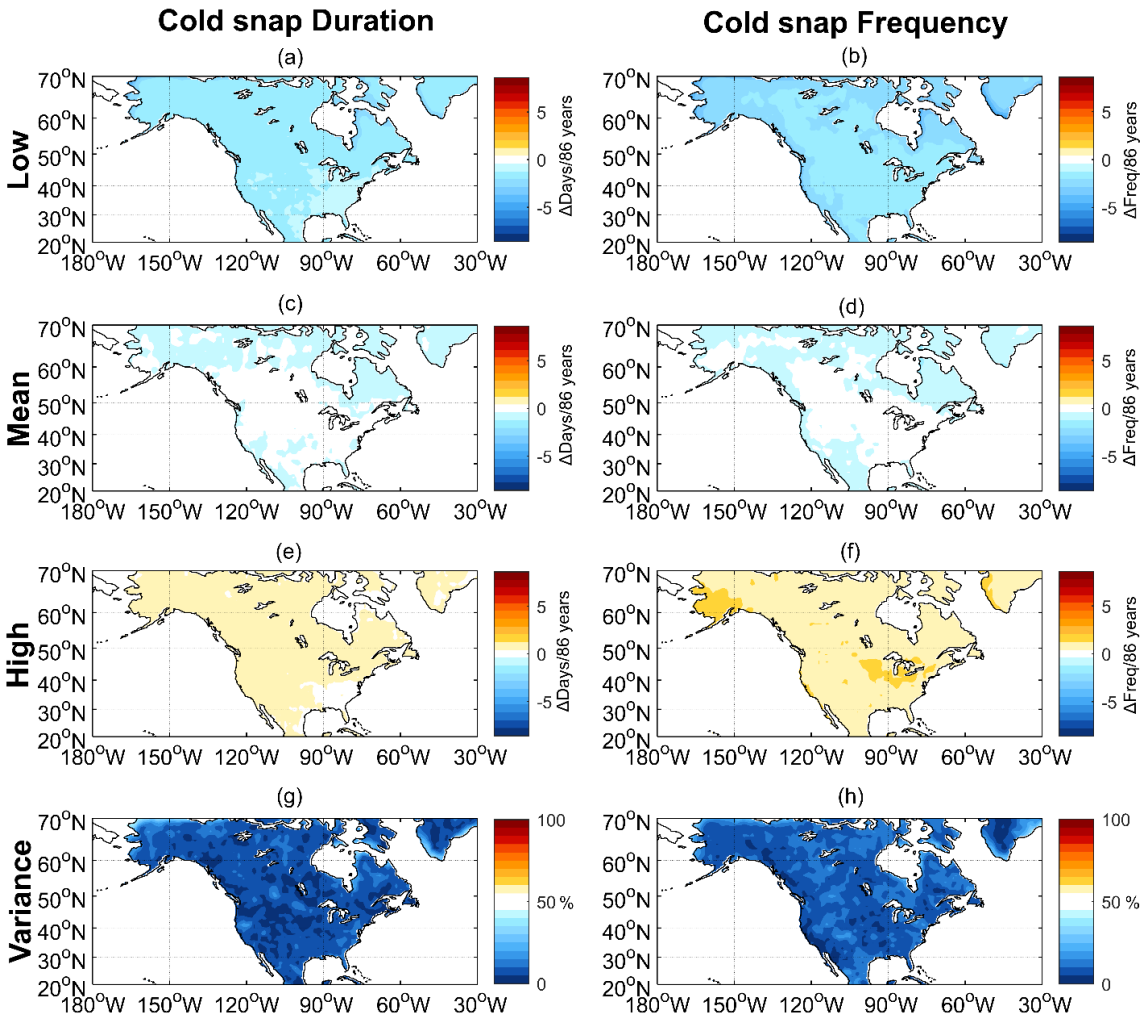

Figure 3.S6. Same as Fig. 3.S4 but for average annual cold snap duration (left column) and average annual cold snap frequency (right column).

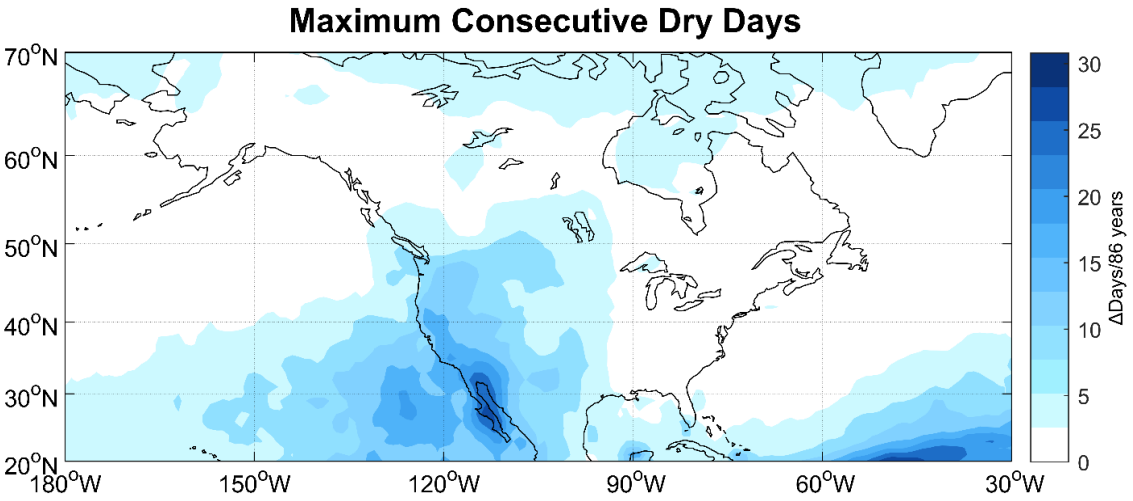

Figure 3.S7. Same as Fig. 3.S1, but for standard deviation in trends in annual maximum number of consecutive dry days.

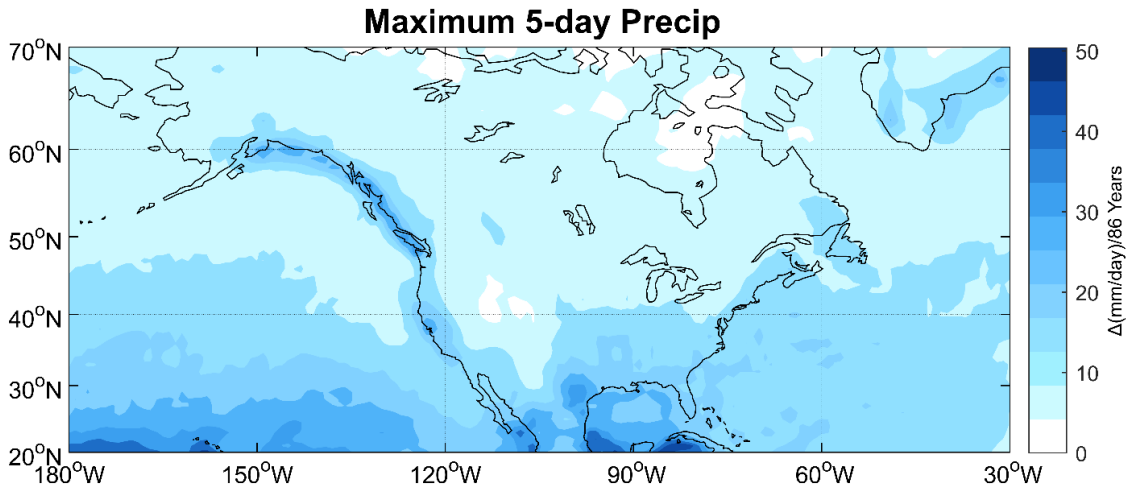

Figure 3.S8. Same as Fig. 3.S1, but for standard deviation in trends in annual maximum 5-day precipitation.

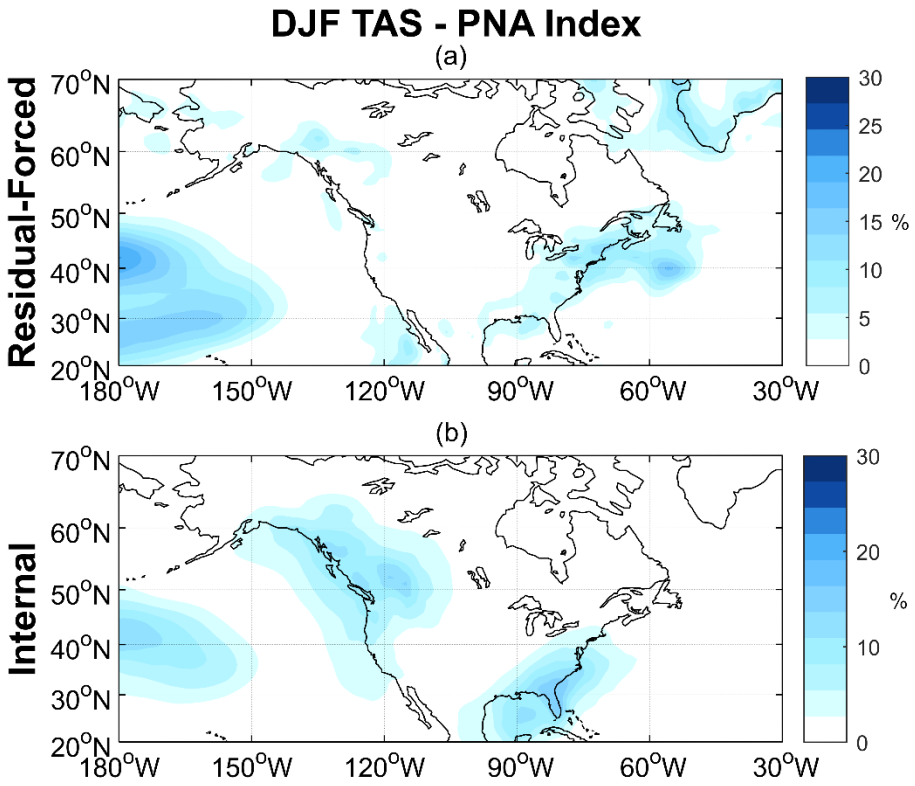

Figure 3.S9. Variance in mean DJF TAS trends explained by (a) residual forced trends in PNA (i.e., model-to-model differences independent of global-mean surface temperature warming, as calculated from equation 2) and (b) PNA trends due to internal variability (as calculated from equation 3). Note that the color bar scale is different from that in Fig. 3.7.

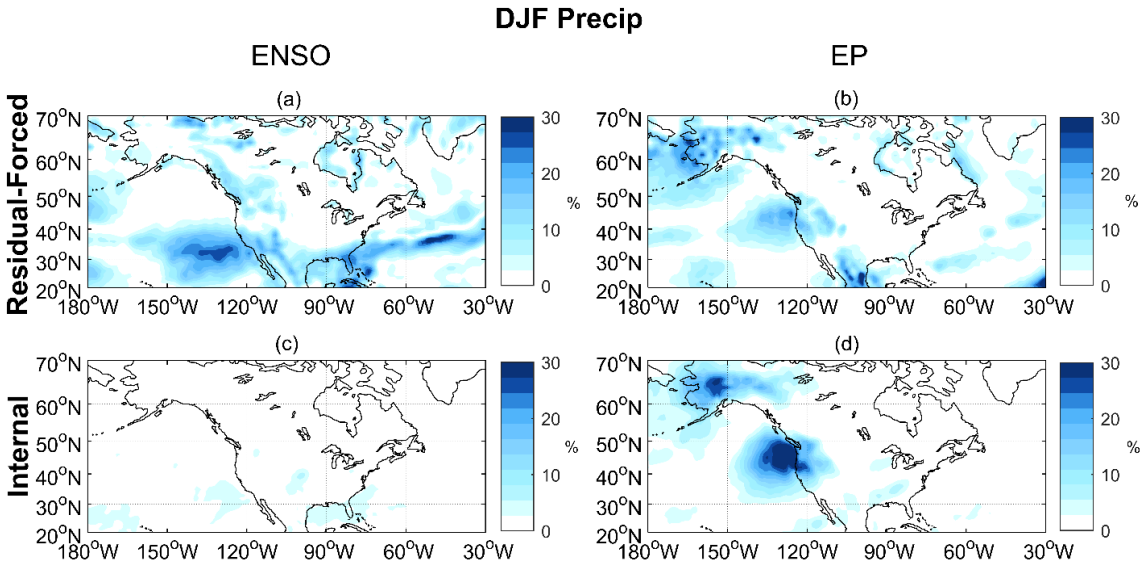

Figure 3.S10. As in Fig. 3.S9, but for variance in DJF mean precipitation trends explained by (top row) residual forced trends (model-to-model) and (bottom row) internal variability in (left column) ENSO and (right column) EP.

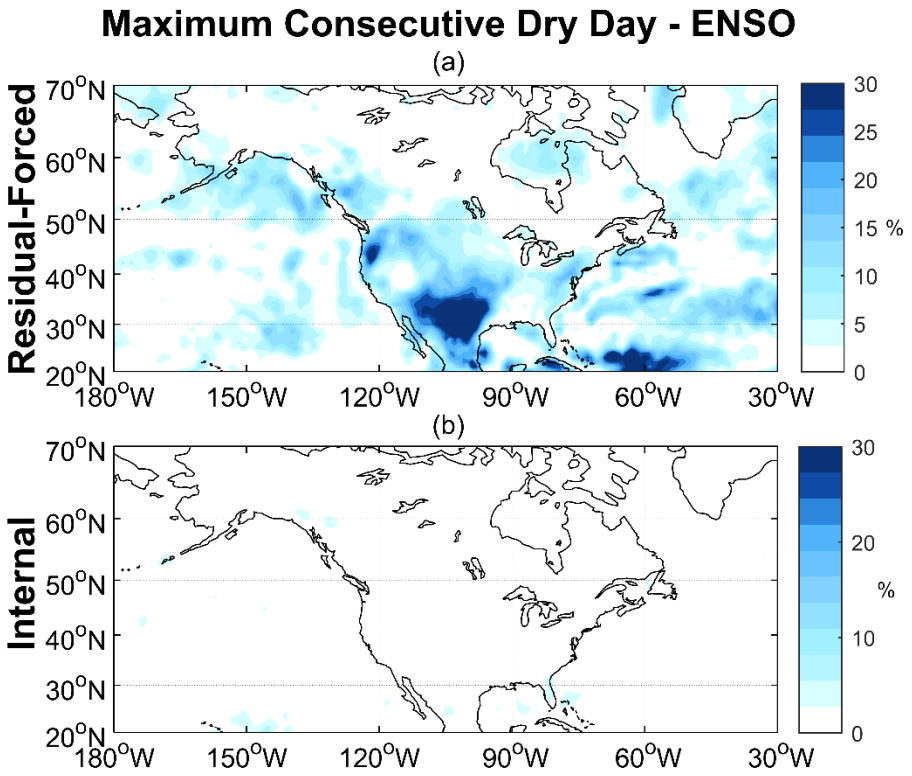

Figure 3.S11. As in Fig. 3.S9, but for variance explained in annual maximum dry consecutive day trends by ENSO.

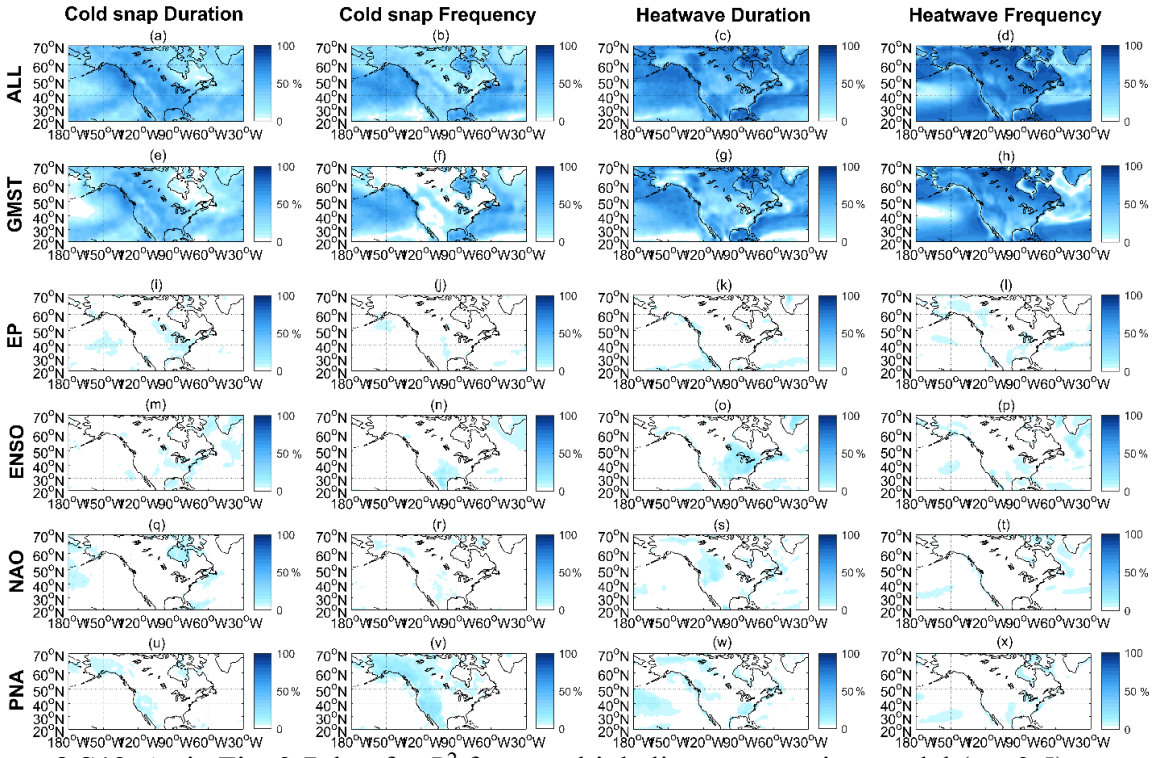

Figure 3.S12. As in Fig. 3.7, but for R^2 from multiple linear regression model (eq. 3.5) predicting trends in various heatwave and cold snap variables.

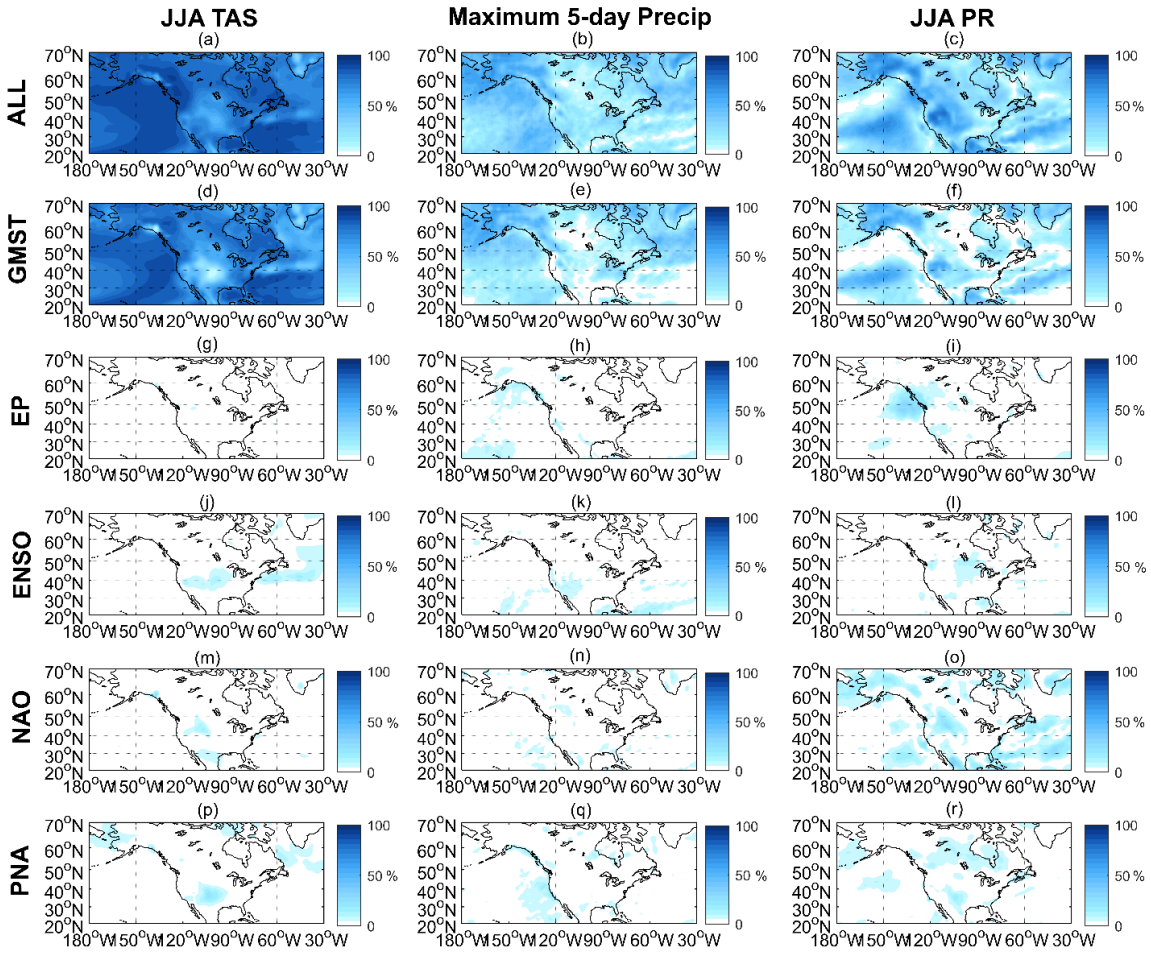

Figure 3.S13. As in Fig. 3.7, but for R^2 from multiple linear regression model (eq. 3.5) predicting trends in JJA mean temperature trends (left column), maximum 5 day precipitation trends (middle column), and JJA mean precipitation trends (right column).

CMIP6 Model	Dataset Reference	Daily	# of Ensemble Members	Monthly	# of Ensemble members
ACCESS-CM2	Dix et al. (2019)	X	5	X	5
ACCESS-ESM1-5	Ziehn et al. (2019)	X	40	X	40
AWI-CM-1-1-MR	Semmler et al. (2019)	X	5	X	5
CNRM-CM6-1	Voldoire (2019)			X	6
CNRM-ESM2-1	Seferian (2019)			X	5
CanESM5	Swart et al. (2019)	X	50	X	50
EC-Earth3	EC-Earth (2019a)			X	6
Ec-Earth3-Veg	EC-Earth (2019b)			X	6
FGOALS-g3	Li (2019)	X	5	X	5
GISS-E2-1-G	NASA/GISS (2020a)			X	27
GISS-E2-1-H	NASA/GISS (2020b)			X	6
INM-CM5-0	Volodin et al. (2019)	X	5	X	5
IPSL-CM6A-LR	Boucher et al. (2019)	X	11	X	11
MIROC-ES2L	Tachiiri et al. (2019)	X	10	X	10
MPI-ESM1-2-HR	Schupfner et al. (2019)	X	10	X	10
MPI-ESM1-2-LR	Wieners et al. (2019)	X	30	X	30
MRI-ESM2-0	Yukimoto et al. (2019)	X	5	X	5
UKESM1-0-LL	Good et al. (2019)	X	16	X	16

Table 3.S1. List of CMIP6 models used in this study.

Chapter 4: Changes to the statistical moments of the Seasonal Distribution of Temperature Across North America

4.1 Introduction

Future changes in mean and extreme temperature as a result of anthropogenic climate change have the potential to greatly impact lives and property, thus projecting these changes remains a key focus of the global climate science community. In response to increased emissions of greenhouse gases (GHGs), climate models agree that near-surface air temperatures tend to increase the most over land (e.g. Sutton et al. 2007; Byrne and O'Gorman 2013) and high latitudes ("Arctic Amplification"; Holland and Bitz 2003; Pithan and Mauritsen 2014). At local scales, however, projections in future temperature trends are more uncertain, and are influenced by internal variability within the climate system (e.g. Deser et al. 2014; Kelleher et al. 2023, hereafter KGS).

In terms of extreme temperature trends, the frequency and intensity of extreme hot temperature events has increased in recent decades, while the frequency and intensity of cold events has decreased, trends that models project to continue with the continued increased emission of GHGs across the 21st century both globally and regionally (Silmman et al. 2013; Seneviratne et al. 2021) as well as over North America (Peterson et al. 2013; Wuebbles et al. 2014; KGS).

In order to document a range of plausible future trends and the role of internal variability in North American mean and extreme temperature and precipitation trends, KGS recently analyzed model output from an ensemble of climate models from phase 6 of the Coupled Model Intercomparison Project (CMIP6; Eyring et al. 2016). Consistent with previous work, they found an increasing trend in both heatwave duration and frequency across North America projected for

the 21st century (see Fig. 1a-h, reproduced from Fig. 3 of KGS). They additionally found that the variability in these projected trends across models was primarily driven by model-to-model differences in the level of global warming across models, suggesting that models that warm more globally have a greater increase in regional heatwave intensity and frequency.

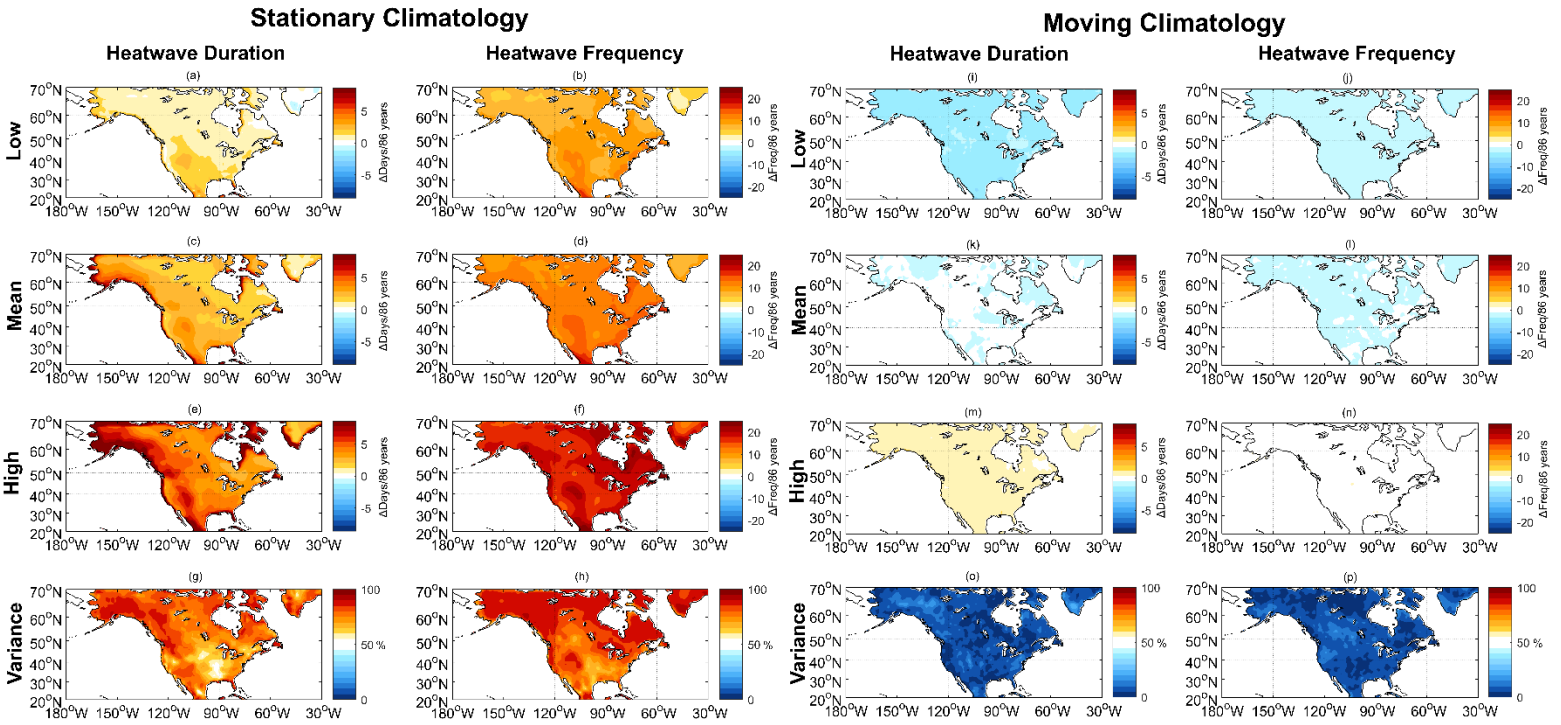

Figure 4.1 2015-2100 trends in heatwave duration and frequency for models under the SSP3-7.0 scenario from CMIP6. The second row shows the mean ensemble trend. Rows 1 and 3 show the mean of the bottom 20% and top 20% respectively of modeled heatwave duration and frequency trends. The fourth row shows the proportion of variability that is attributed to inter-model differences (as in KGS). The two leftmost columns show the trends for a stationary temperature climatology from the first thirty years of each simulation (2015-2044), while the two rightmost columns show the trends for a centered-moving temperature climatology.

This result however, in Fig. 4.1a-h, is based on heatwaves defined with a stationary climate from the first 30 years of each model simulation (2015-2044). KGS found that, if the definition of a heatwave were to be allowed to change with the changing climate using a centered-moving climatology, there was little-to-no trend in the average duration or frequency of heatwaves (Fig.

4.1i-p, reproduced from Fig. S4 of KGS). Additionally, they found that any variability in the projected moving-climatology heatwave trends across models was the result of internal variability, suggesting that the rate of global warming within the model is not related to changes in the character of regional heatwaves, and that the changes in regional heatwaves shown in Fig. 4.1a-h are simply the result of the background climate warming. Similar results were found for projected decreases in cold snap events with global warming (Figs. 4 and S6 from KGS). These results raise questions about the nature of changing temperatures as a result of climate change. Is climate change leading to changes in both the daily mean and distribution of temperature, or is there only a shift in the mean?

There has been a large amount of work focused on changes in the distribution of temperature, particularly for temperatures during the summer season over Europe. Following the extreme European heat wave of 2003, Schar et al. (2004) found that, for the event to occur, an increase in both the variance and mean of the summertime temperature field near Switzerland (near the center of the 2003 heatwave) was required. Other studies, however, were unable to find significant increases in variance (e.g. Acero et al. 2014 for the Iberian Peninsula), and trends in Italian summer temperatures were found to be consistent with a shift across all percentiles (Simolo et al. 2010). It thus appears that changes in summer temperature distributions across the Northern Hemisphere midlatitudes vary regionally (Cavanaugh and Shen 2014; McKinnon et al. 2016).

In the winter season, however, it is well understood that temperature variance is projected to decrease in the Northern Hemisphere midlatitudes as a result of GHG-forced climate change. This is primarily caused by a reduction in the equator-to-pole temperature gradient driven by Arctic amplification (Screen 2014; Schneider et al. 2015; Tamarin-Brodsky et al. 2020). This

reduction in the equator-to-pole temperature gradient acts to decrease the meridional advection. Because synoptic temperature variability is primarily driven by advection, this reduction in meridional advection reduces the temperature fluctuations, particularly in mid to high latitudes (Screen 2014; Schneider et al. 2015).

Recent work has also highlighted the importance of skewness for correctly capturing temperature distributions and their changes as a result of climate change (e.g. Garfinkel and Harnik 2017; Linz et al. 2018; Tamarin-Brodsky et al. 2019, 2020). Two main mechanisms have been proposed that describe how temperature skewness can be driven dynamically as a result of meridional advection. The first mechanism, important over the midlatitude storm track regions, is driven by nonlinear meridional thermal advection by anomalous cyclone-anticyclone pairs that are responsible for equatorward (poleward) movement of cold (warm) anomalies (Garfinkel and Harnik 2017; Linz et al. 2018; Tamarin-Brodsky et al. 2019). The second mechanism, more important in the Northern Hemisphere due to the large temperature gradients driven by the abundance of continents, is driven by linear meridional advection of temperature anomalies generated by spatially asymmetric background temperature gradients (Tamarin-Brodsky et al. 2020). As a result of Arctic amplification, cold anomalies advected from the Arctic weaken more than warm anomalies advected from the tropics leading to an increase in skewness over much of the Northern Hemisphere during winter (Gao et al. 2015; Tamarin-Brodsky et al. 2020).

The purpose of this work is to explore changes in the seasonal distributions of temperature and its higher statistical moments across North America using output from an ensemble of CMIP6 models. From this, we will be able to determine what changes, if any, are occurring within the models' seasonal temperature distributions and if these changes are consistent with current understanding. Further, because we are using a model ensemble, we will

be able to decompose the variability in the temperature distribution trends to being either forced (i.e. driven by global temperature changes or other model physical differences) or internal (variability present in the climate system in the absence of forcing) variability. This chapter is organized as follows. Section 4.2 describes the data and methods used in this study. Section 4.3 reviews the range of projected changes in the seasonal temperature distributions' statistical moments and assesses the relative roles of model uncertainty (forced variability) versus internal variability in the future trends. Section 4.4 concludes with a summary and discussion of our results.

4.2 Data and Methods

Data for this study is sourced from global climate model output from CMIP6 (Eyring et al. 2016) under the SSP3-7.0 future emissions scenario (2015-2100). This scenario is a medium-to-high GHG emissions, high aerosol pathway constructed to reach a future radiative forcing of 7.0 W m^{-2} greater than pre-industrial levels by the year 2100. Following KGS, we use this emissions scenario as it was requested to have the largest number of ensemble members per model (O'Neill et al. 2016). For this study we use all SSP3-7.0 ensemble members from models with at least five ensemble members and the availability of daily timescale temperature data, leading to a total of 192 simulations across 12 models (see list of all models in Table 4.S1).

We consider three statistical moments of daily seasonal temperature distributions in this study. First, we consider variance, the second-order moment of the distribution represented in this study as the standard deviation. Second, we consider skewness, the third-order statistical moment of the distribution. Last, we consider kurtosis, the fourth-order moment of the distribution. Fig. 4.2 shows how changes in each moment of the distribution act to change the

underlying distribution. In Fig. 4.2a, a normal distribution with a mean of 0 and a standard deviation 1 (black curve, consistent across Figs. 4.2a-d) is plotted. A change in the mean of the distribution represents a simple shift of the entire distribution, as shown by the blue (decreased mean) and red (increased mean) curves. Fig. 4.2b shows the same, but for changes in only the standard deviation of the distribution. In this case, the distribution remains centered on 0, but the width of the distribution decreases for the blue curve, leading to a sharper peak in the blue curve, and vice-versa for the red curve.

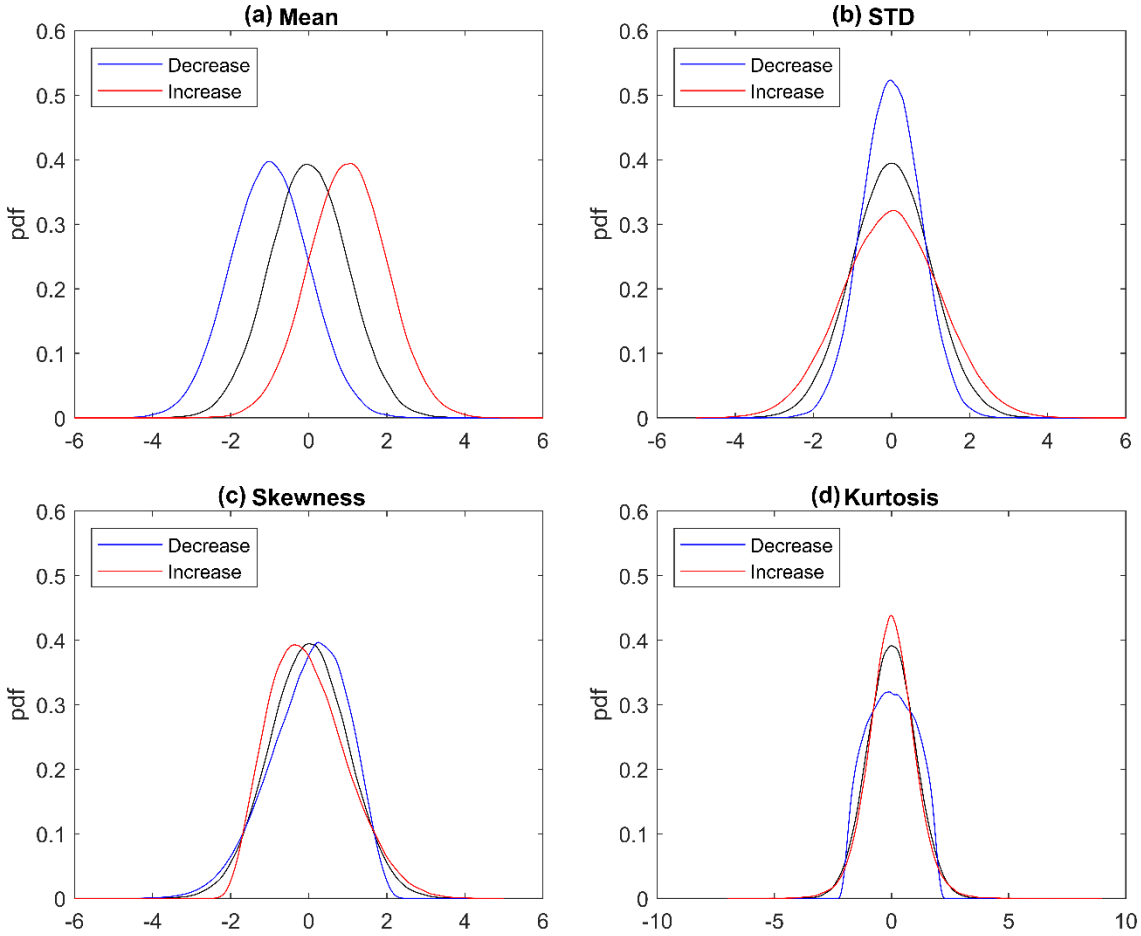

Figure 4.2 Schematics of PDFs with differing (a) mean, (b) standard deviation, (c) skewness, and (d) kurtosis. The black curve in each panel represents a randomly generated normal distribution with a mean of 0 and standard

deviation of 1. The blue (red) curve in each panel represents the same distribution but with only a decrease (increase) of the statistical moment in question.

Fig. 4.2c shows the same exercise but for changes in the skewness of the distribution. Skewness in the distribution refers to the symmetry of points around the mean of the distribution. A zero skewness, as shown by the black curve, means that the positive and negative tails are symmetric around the mean. An increase in skewness, as shown by the red curve, implies that the positive tail is longer than the negative tail (so called "right-tailed" distributions) and the opposite is true for negative skewness distributions (so called "left-tailed" distributions, blue curve on Fig. 4.2c). Lastly, Fig. 4.2d shows the same but for changes in the kurtosis of the distribution. Kurtosis is indicative of the "extremity" of the distribution, or more simply how much of the distribution lies within the tails. A normal distribution has a kurtosis of exactly 3 (black curve), so kurtosis is often described instead as excess kurtosis by subtracting 3 from the calculated kurtosis. Distributions with positive excess kurtosis will have more of the distribution around both the means and the tails (Fig. 4.2d, red curve), while distributions with negative excess kurtosis have less of the distribution at the tails and more of the distribution evenly spread close to the mean of the distribution, assuming that there is no skewness within the distribution. Figs. 4.2c and 4.2d demonstrate that the distribution of extreme events within the seasonal temperature distribution is not solely reliant on changes to either the mean or the standard deviation of the distribution. This suggests that, while there may not be a change in the standard deviation of the seasonal temperature distribution, as is found during the summer across some of the Northern Hemisphere midlatitudes, there may still be observable changes in the rate of occurrence of extreme events.

To calculate these statistical moments in the CMIP6 models, we first isolate the summer (JJA) and winter (DJF) days from the rest of the data at each grid point. We then split the data into individual seasons (i.e., the first DJF of each climate model denotes the first winter for each model) and calculate each moment for each individual season. We then find the trend in each moment for each model for wintertime and summertime. After calculating the 21st century trends in each of the statistical moments across North America, we decompose the variability in the trends into forced and internal variability following the method of Schmidt and Grise (2021; see also KGS). Forced variability captures variability among model-to-model responses to the same external forcing (i.e., model uncertainty). Internal variability refers to the variability present in the climate system in the absence of external forcing. Internal variability is known to play a significant role in modeled mean temperature trends across North America, particularly in the Pacific Northwest and American Southeast (Deser et al. 2014), and thus may also play a role in shaping how the seasonal temperature distribution is projected to change across models.

4.3 Projected Changes in the Seasonal Temperature Distributions across CMIP6 Models

In this section, we document the range of 21st century trends in three statistical moments of seasonal near-surface air temperature distributions: standard deviation, skewness, and kurtosis. We further document the roles of model uncertainty versus internal variability within these trends. This analysis first allows us to note the range in trends for the statistical moments and whether climate models agree on the signs of future trends. Second, by partitioning the variance following the method of Schmidt and Grise (2021), we can determine if the range of

future distribution changes is due to model-to-model differences, such as the rate of global warming (climate sensitivity) of the model, or due to internal variability.

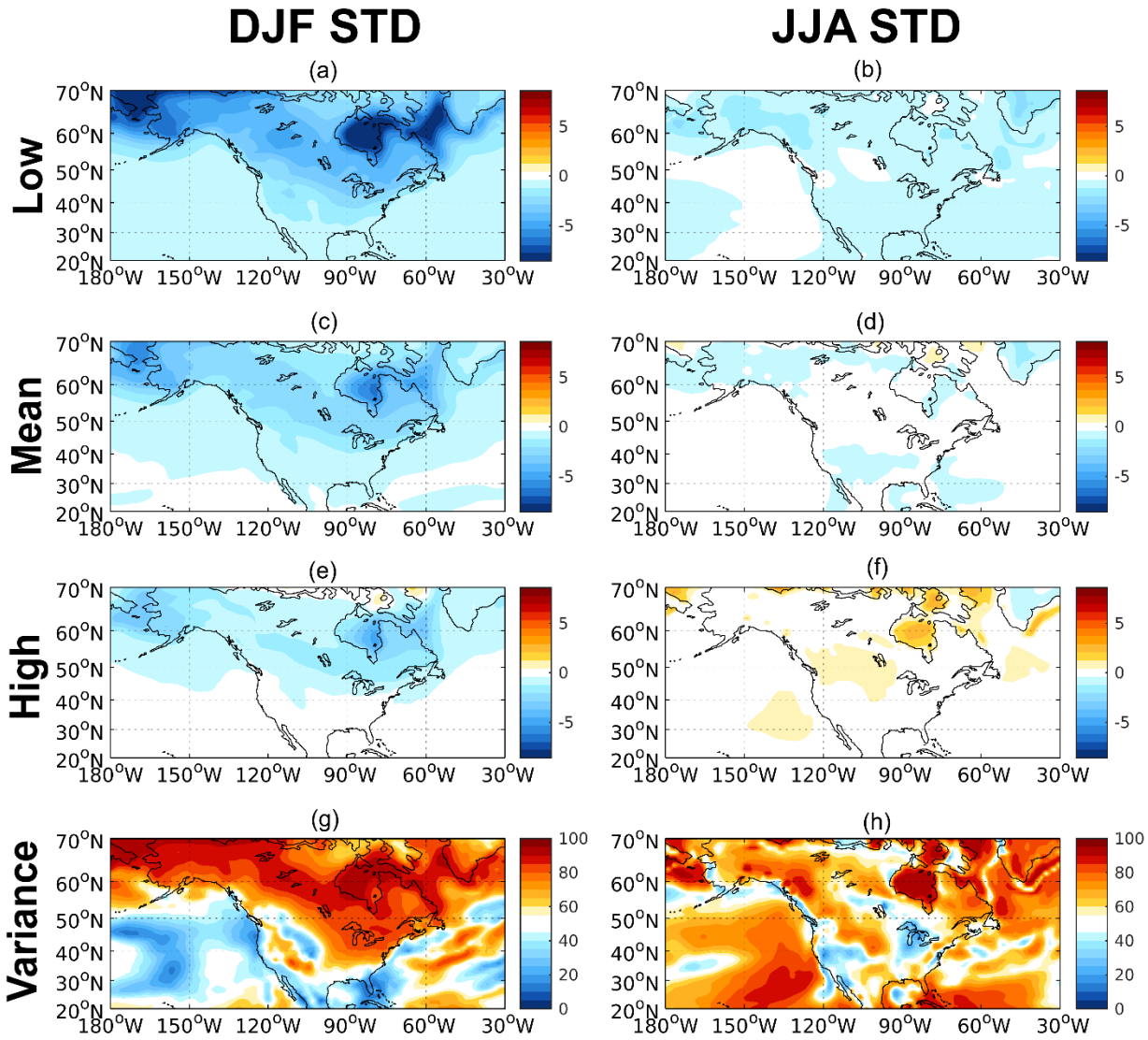

Figure 4.3 2015-2100 trends in DJF (left column) and JJA (right column) seasonal standard deviation in near-surface air temperature (TAS) for models under the SSP3-7.0 scenario from CMIP6. (c) and (d) show the multi-model ensemble mean seasonal TAS standard deviation trends. (a) and (b) show the mean of the bottom 20% of modeled seasonal TAS standard deviation trends. (e) and (f) show the same as (a) and (b) but for the top 20% of modeled trends. (g) and (h) show the proportion of the variability in the modeled trends that is due to inter-model differences.

Figs. 4.3c and 4.3d show the multi-model ensemble mean trend in seasonal daily mean temperature standard deviation over the 2015-2100 period for the SSP3-7.0 experiment for DJF and JJA, respectively. In DJF (Fig. 4.3c), as expected from prior research (Screen 2014; Schneider et al. 2015; Tamarin-Brodsky et al. 2020), there is a reduction in the standard deviation of daily temperature that is particularly pronounced at high latitudes. In JJA (Fig. 4.3d), changes in the standard deviation of daily temperature are much less pronounced, with little to no change in standard deviation projected in the multi-model ensemble mean through much of North America. This is consistent with the results of McKinnon et al. (2016) who found that, after analyzing observed weather stations to estimate temperature distribution changes during summer, most of the probability density function (PDF) changes could be explained by a shift in the mean and changes in the remaining variability were small.

To represent the range of potential trends in standard deviation, we show the mean of the 0^{th}-20^{th} percentile of trends from individual model simulations (Figs. 4.3a-4.3b) and the mean of the 80^{th}-100^{th} percentile of trends from individual model simulations (Figs. 4.3e-4.3f) on a grid point by grid point basis. Because these panels are constructed for each grid point, they should *not* be seen as physical possibilities as each grid point may be represented by a different subset of models and should instead be considered to represent the amount of variability present across the multi-model ensemble.

For winter seasonal temperature standard deviation (Figs. 4.3a, 4.3e), the distribution in the trends across the multi-model ensemble is primarily located at high latitudes, presumably related to the degree of Arctic Amplification present within the models. To confirm this, we correlate the DJF standard deviation trends across models to a simple measure of Arctic amplification, the ratio of the Arctic (>67°N) warming trend and the global mean warming trend.

We find that there is a moderate negative correlation between the two in North America (Fig. 4.4), suggesting that models with a greater degree of Arctic amplification have a larger reduction in DJF daily temperature standard deviation. Additionally, the sign of the change in standard deviation across North America largely does not change, suggesting that models across the multi-model ensemble agree that the standard deviation of temperature will decrease across

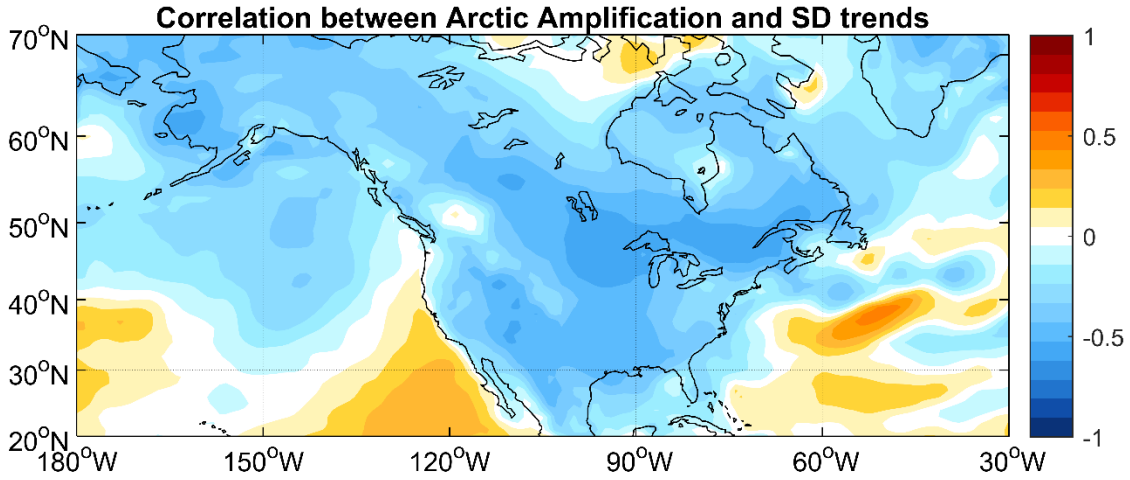

Figure 4.4 Correlation coefficient between modeled DJF temperature standard deviation trends and the degree of Arctic amplification present. The degree of Arctic amplification is defined as the ratio between the 21st century rate of Arctic (>67°N) warming and the 21st century rate of global-mean warming.

North America during the 21st century. For summer standard deviation (Figs. 4.3b, 4.3f) the range across models is smaller than that of the winter months, but the sign of the trend in standard deviation changes across much of North America suggesting that models disagree about the future change in the summer temperature distribution.

Figs 4.3g and 4.3h show the proportion of the variance in standard deviation trends across model simulations that can be attributed to model-to-model differences after decomposing the variability following the method of Schmidt and Grise (2021). Because the combination of the variance from inter-model differences and intra-model differences (internal variability) adds up

to 100% by construction, a grid point that is colored red can be thought of as a location where model-to-model differences explain the majority of the variability across model simulations, and a grid point that is colored blue is a location where internal variability is the primary source of variability. In DJF, at high latitudes, variability in the model trends is dominated by forced variability. This result is consistent with the expectation that a weakened equator-to-pole temperature gradient drives the reduction in the standard deviation of temperature (Screen 2014; Schneider et al. 2015) as models that warm more will have a larger reduction in the equator-to-pole temperature gradient (see also Fig. 4.4). In North America, internal variability plays a larger role in the Pacific Northwest and southeastern United States, two regions where a common mode of climate variability called the Pacific North American (PNA) pattern is important in driving wintertime temperature variability (Leathers et al. 1991; Deser et al. 2014). In JJA, as with DJF, the majority of the variability across much of North America is the result of model-to-model differences, though not as much as in the DJF high latitudes. However, unlike DJF, the variability in JJA is more associated with the forced variability that does not scale linearly with temperature (supplemental Fig. 4.S1). This suggests that much of the 'forced' variability comes from model differences in physical parametrizations rather than from model climate sensitivity.

In Fig. 4.5 we repeat the analysis from Fig. 4.3, but for the DJF and JJA trends in seasonal temperature skewness. Skewness trends in DJF in the multi-model ensemble mean (Fig. 4.5c) are characterized by a broad increase in skewness at North American midlatitudes (roughly just south of the border between Canada and the United States) and reductions in skewness at higher latitudes. Variability in modeled trends (Figs. 4.5a and 4.5e) is largely related to how pronounced these features are, as the 'low' skewness models at each grid point exhibit a large reduction in the skewness at high latitudes and the 'high' skewness models at each grid point

exhibit a large increase in skewness in a band at midlatitudes. As noted by Tamarin-Brodsky et al. (2020), the increase in skewness at midlatitudes is likely the result of the weakening of background equator-to-pole temperature gradients, decreasing the meridional advection of cold anomalies from the arctic and thus increasing the skewness. While skewness changes may also be related to the shifting of the midlatitude jet (and its related storm tracks) as a result of climate change, shifting the anomalous cyclone-anticyclone pairs responsible for the meridional

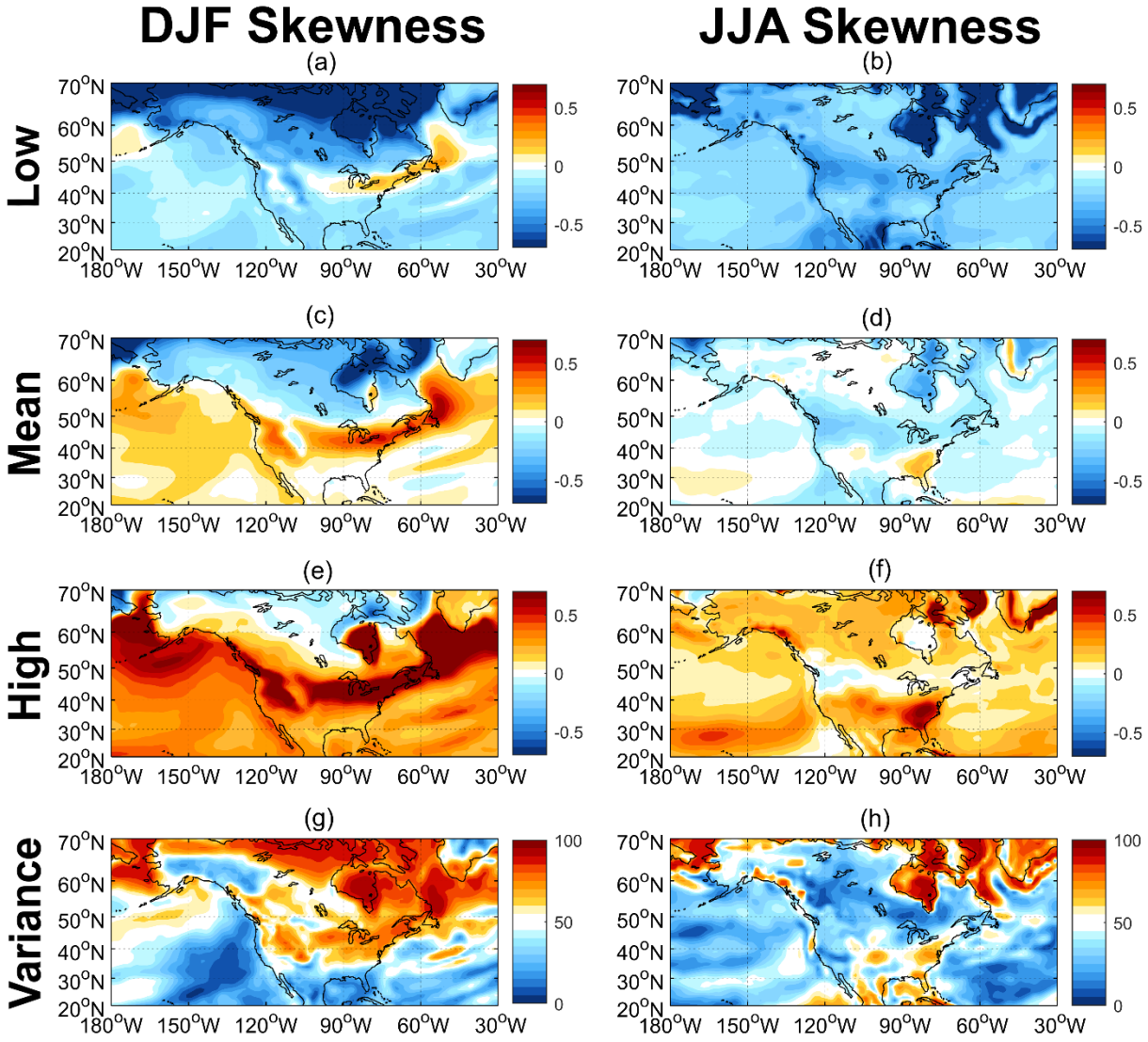

Figure 4.5 Same as Fig. 4.3, but for trends in seasonal temperature skewness.

advection of cold and warm anomalies (Garfinkel and Harnik 2017; Linz et al. 2018; Tamarin-Brodsky et al. 2019), this is unlikely over North America as the midlatitude jet is not projected to shift much poleward in CMIP6 models in this region (Harvey et al. 2020). Instead, this increase in skewness may be associated with changes in winter-time snow extent, which has been shown to be associated with temperature variability and extremes in North America (Diro et al. 2018). As with standard deviation, much of the variability across model skewness trends is the result of forced variability at high latitudes (Fig. 4.5g), consistent with the reduction of the meridional temperature gradient driven by Arctic amplification being related to the increase in skewness at midlatitudes (not shown). Equatorward of the region influenced by the midlatitude jet, however, variability in the skewness trends is largely the result of internal variability.

Unlike DJF, the multi-model ensemble mean skewness trends in JJA are relatively small and negative throughout much of North America (Fig. 4.5d). Additionally, the sign of the skewness trend varies across model simulations throughout the entirety of the study region (compare Figs. 4.5b and 4.5f) and internal variability is the primary driver of variability in the skewness trends across models (Fig. 4.5h). This is expected for two reasons. First, the fact that Arctic amplification is much more pronounced in the winter than the summer, means that the equator-to-pole temperature gradient is not altered as much in summer as it is in winter, leading to smaller changes in variance. Second, the synoptic scale systems that generate skewness in midlatitude temperatures are not as prevalent during Northern Hemisphere summer as they are during Northern Hemisphere winter. In other words, the two main mechanisms outlined in

Tamarin-Brodsky et al. (2022) to produce temperature skewness dynamically are not as important during Northern Hemisphere summer than they are in winter.

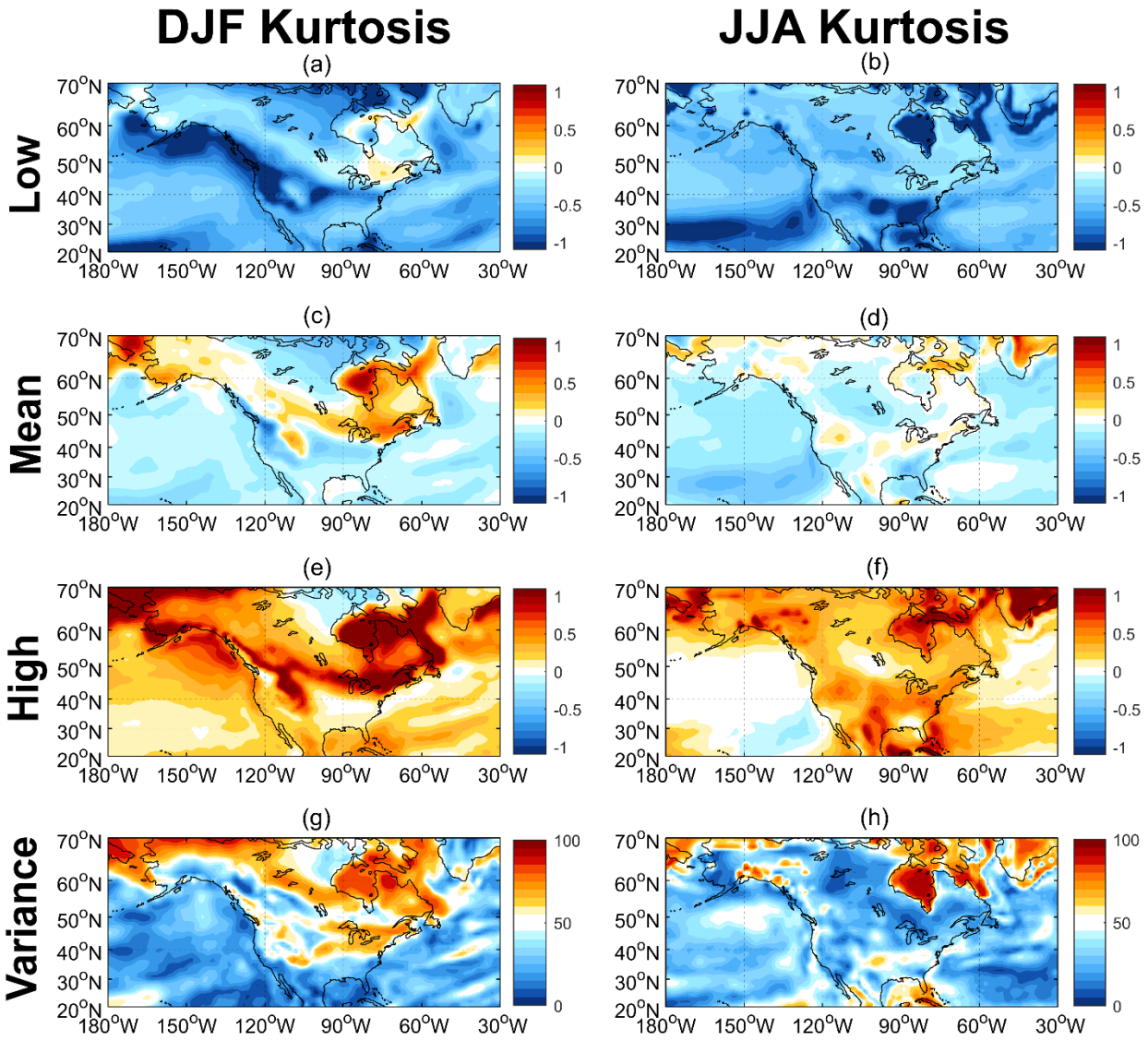

Figure 4.6 Same as Fig. 4.3, but for seasonal temperature kurtosis.

In Fig. 4.6 we document the modeled trends in the kurtosis of seasonal temperatures. As with skewness, we find that DJF kurtosis in the multi-model ensemble mean is defined by a well-defined band of increasing kurtosis at North American midlatitudes with decreasing kurtosis poleward of the band (Fig. 4.6c). Unlike skewness, however, there is a moderate reduction of

kurtosis equatorward of this band. Variability in the kurtosis trends is, as with skewness, defined by the strength of these features, with the 'low' kurtosis models exhibiting strong reductions in kurtosis (Fig. 4.6a) and the 'high' kurtosis models having a well-defined strong band of kurtosis increases (Fig. 4.6e). While internal variability is more important to describing the variability of modeled temperature kurtosis trends than that of skewness trends (compare Figs. 4.5g and 4.6g), the overall shape is largely consistent with that of the temperature skewness trends. The similarities to skewness trends are more apparent with the JJA kurtosis trends (compare right columns of Figs. 4.5 and 4.6), with the patterns largely mirroring those of the skewness trends. The similarities between the modeled kurtosis trends and skewness trends are consistent with the results of Tamarin-Brodsky et al. (2022), who found that kurtosis changes in near-surface temperature are largely predicted by the skewness changes.

4.4 Conclusions

While research largely focuses on the changes in near-surface mean temperature as a result of anthropogenic climate change, potential changes to the seasonal distribution of temperature are also important to understand in the context of changes in extreme temperature events. Previous work (KGS) identified that increases in heatwave frequency and duration were only found across CMIP6 models under a moderate-to-high future emissions scenario (SSP3-7.0) if the climatology that defines heatwaves was based on a stationary climate. Instead, if a centered-moving climatology was used to define the heatwaves, little-to-no change in heatwave frequency or occurrence was present, and the variability in the trends was dominated by internal variability (Fig. 4.1, adapted from KGS). Motivated by those results, this study explores the projected changes in the distribution of seasonal daily mean temperatures, including the higher

statistical moments of the distribution of standard deviation (to represent variance), skewness, and kurtosis. We additionally attribute the spread in trends across model simulations to either model-to-model differences (so-called 'forced' variability) and internal variability.

For the DJF daily temperature distribution, consistent with prior studies (Screen 2014; Schneider et al. 2015; Tamarin-Brodsky et al. 2020), we find a projected reduction in the standard deviation of temperature over the 21st century, particularly at high latitudes (left column of Fig. 4.3), and find that these trends are associated with the degree of Arctic amplification present within each model ensemble member (Fig. 4.4). The majority of variability across models in this region was the result of model-to-model differences (Fig. 4.3g), largely associated with variations in climate sensitivity across models (Fig. 4.S1). This suggests that were the climate sensitivity of models to be further constrained (as in recent studies by Sherwood et al. 2020 and McCoy et al. 2022), one could further reduce the variability in projections of standard deviation changes across Northern America during the winter.

Consistent with the mechanisms outlined in Tamarin-Brodsky et al. (2022), there is an increase in skewness across a band of North America (Fig. 4.5c) as Arctic amplification leads to a reduction in the equator-to-pole temperature gradient over the 21st century. This suggests that not only is the distribution tightening as a result of a decrease in variance, the distribution is also becoming right-tailed in nature (Fig. 4.2). It appears thus that the warm anomalies of the winter season remain into the future in this region, with a reduction only in the cold anomalies. The variability in skewness across models in this region is also predominantly driven by model-to-model variability (Fig. 4.5g), as models with higher climate sensitivities undergo a greater reduction in the meridional temperature gradient. Trends in the kurtosis for DJF temperature are largely in line with trends in skewness (Fig. 4.6; left column), consistent with the findings of

Tamarin-Brodsky et al. (2022) that kurtosis changes are largely predicted by changes in skewness. This leads to an increase in kurtosis along a latitude band in North America that is well co-located with the band of increased skewness. Recall from Fig. 4.2d that increases in kurtosis lead to the distribution becoming more peaked at the center while increasing the tails of the distribution. While at first glance this would suggest that the increase in kurtosis in this region should lead to an increased frequency in both cold and warm extremes, it is important to note that the idealized changes to the tails are dependent on no change in skewness. As noted in Fig. 4.1c of Tamarin-Brodsky et al. (2022), increases in kurtosis in conjunction with increases in skewness can have fewer negative extremes than those of a normal distribution. This means that the trend towards fewer cold extremes and increases in warm extremes is consistent with the increase in kurtosis across this latitude band as it is acting in conjunction with an increase in skewness in this region.

For the daily temperature distribution in summer (JJA), the multi-model ensemble mean exhibits relatively small changes in standard deviation, skewness, and kurtosis (compare left and right columns of Figs. 4.3, 4.5, and 4.6). Consistent with the lack of influence from Arctic amplification during Northern Hemisphere summer, as well as the weaker influence from midlatitude jet driven synoptic weather systems, there is not much change in the standard deviation of surface temperature in summer, especially when compared to winter. Further, these results are consistent with the results of McKinnon et al. (2016) who find that the changes in summertime temperature distributions can be largely explained by a simple shift in the mean of the distribution, rather than changes to higher order statistical moments. Previous research (e.g. Schar et al. 2004; Simolo et al. 2010; Acero et al. 2014), however, suggests that these results may be based on the region of study, so further work is needed to demonstrate whether the lack

of changes across the JJA statistical moments and the importance of internal variability is dependent on the region of study.

4.5 Supplemental Information

CMIP6 Model	Dataset Reference	# of Ensemble Members
ACCESS-CM2	Dix et al. (2019)	5
ACCESS-ESM1-5	Ziehn et al. (2019)	40
AWI-CM-1-1-MR	Semmler et al. (2019)	5
CanESM5	Swart et al. (2019)	50
FGOALS-g3	Li (2019)	5
INM-CM5-0	Volodin et al. (2019)	5
IPSL-CM6A-LR	Boucher et al. (2019)	11
MIROC-ES2L	Tachiiri et al. (2019)	10
MPI-ESM1-2-HR	Schupfner et al. (2019)	10
MPI-ESM1-2-LR	Wieners et al. (2019)	30
MRI-ESM2-0	Yukimoto et al. (2019)	5
UKESM1-0-LL	Good et al. (2019)	16

Table 4.S1. List of CMIP6 models used in this study.

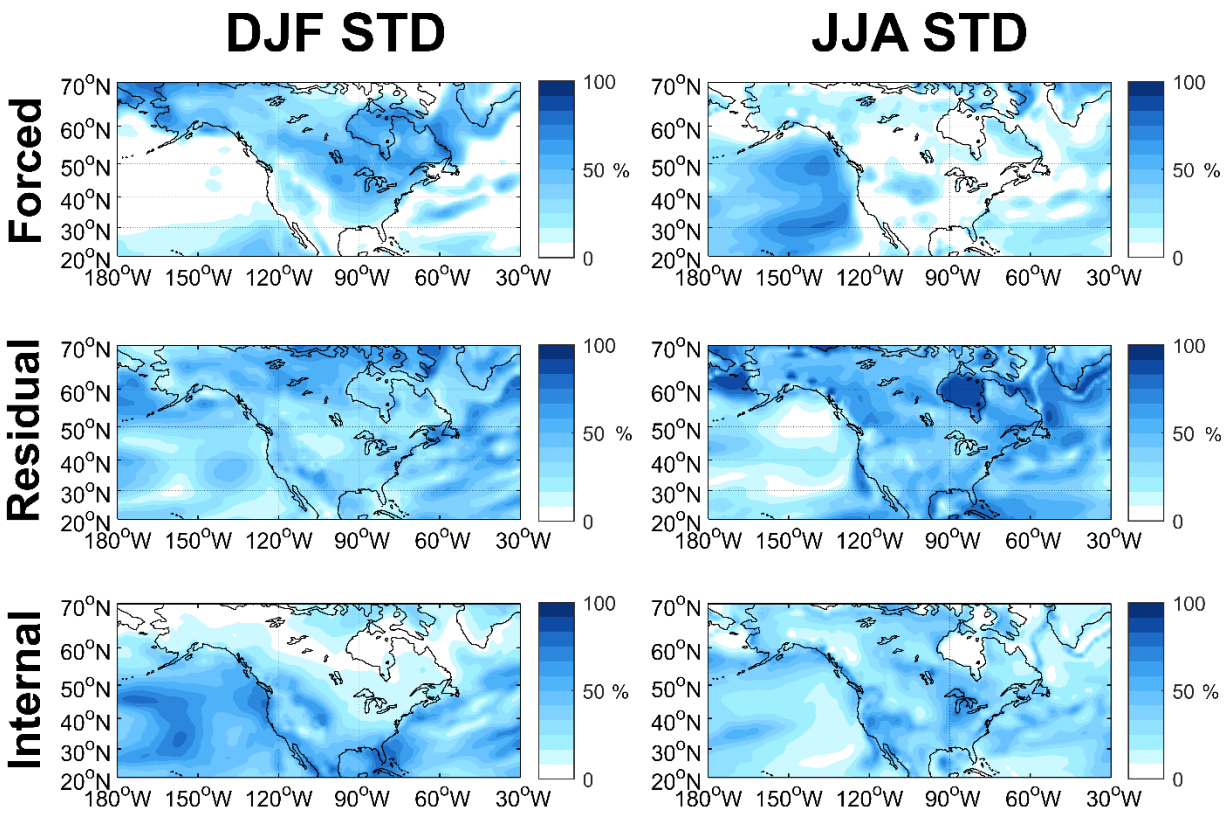

Figure 4.S1. Decomposed DJF (left column) and JJA (right column) variability across model trends in seasonal temperature standard deviation following the method of Schmidt and Grise (2021). The top row represents the percentage of variability that is associated with linear changes in global mean temperature, the middle row represents the 'residual' forced variability (forced variability that does not scale linearly with the global mean temperature), and the bottom row represents the component of the variability driven by internal variability.

Chapter 5: Summary and Conclusions

While climate models have improved across generations, uncertainty in future projections remains an obstacle to policymakers and stakeholders planning for the future. Two areas of remaining uncertainty are the role of cloud feedbacks in the climate system as a result of climate change and the role of internal variability within the climate system.

In Chapter 2, I show that the differing shortwave CRE response to a poleward shift in the midlatitude jet or Hadley cell extent is caused by the shortwave CRE sensitivity to dynamical cloud-controlling factors being a function of latitude. At the latitude at which Hadley cell dynamics are affected for a change in the Hadley cell extent shift, changes in mid-tropospheric vertical velocity are more associated with shortwave CRE changes, leading to a net shortwave cloud radiative warming effect in midlatitudes. Conversely, the dynamical changes associated with a poleward jet shift occur further poleward in a regime where the sensitivities of SWCRE to changes in vertical velocity and EIS effectively balance, leading to a near-net zero change in shortwave CRE in midlatitudes with a poleward jet shift (Figs. 2.1-3). Further, I show that the reason that models by in large fail to recreate the differing shortwave CRE responses is because the models tend to have jet dynamics that occur anomalously equatorward (Fig. 2.4), in a region where the effects of vertical velocity dominate over EIS. This leads to the models creating nearly identical shortwave CRE responses to both poleward jet and Hadley cell extent shifts. These results suggest that future work should focus on understanding the biases in the GCMs' mean state dynamics, as the results in Chapter 2 provide a cautionary example of how applying observational sensitivities of cloud properties to cloud-controlling factors with changes in those cloud-controlling factors from GCMs using a multiple linear regression model, as is commonly done (e.g., Klein et al. 2017).

In Chapter 3, I explore trends in North American mean and extreme temperature and precipitation and the role of internal variability in the trends. By decomposing the variability into model-to-model variability and internal variability, I construct storylines with "constrainable" (i.e., model-to-model) and "not constrainable" (internal variability) axes. I demonstrate that, using constraints on ECS from previous research (McCoy et al. 2022), the storylines of future maximum dry consecutive days are better constrained (Fig. 3.11). Future work could thus focus on improving constraints for the other physical drivers that are not related to internal variability. Additionally, as this work was on done for one SSP, it could be repeated for other SSPs with differing GHG and aerosol forcings.

As much of the variability in extreme temperature and mean and extreme precipitation is not solely related to the level of warming within the models, the recent practice of the IPCC and other governmental climate assessments of using epochs of these models to identify the climate at different warming levels (e.g., James et al. 2017; Tebaldi and Knutti 2018) might be problematic in some instances. Future work should focus on whether or this method is appropriate for determining future projections of climate change.

Lastly, in Chapter 4, I show that, consistent with previous results, over the 21st century, models project a reduction in variance and an increase in skewness of the North American winter daily temperature distribution due to decreased cold advection from high latitude as a result of Arctic amplification. These changes are for the entire season, however, so future work could focus on whether there is any change in the day-to-day changes in temperature, such as temperature swings driven by frontal passages. Changes in the summer temperature distribution, however, are shown to be best approximated with a shift in the mean alone. Future work should

identify whether these results for summer are the result of the region of study, and whether other regions do contain changes in their higher statistical moments.

Acknowledgements

I would like to thank my committee members Kevin Grise, Robert Davis, Todd Scanlon, and Ed Murphy, as well as external collaborator (and former lab mate) Daniel Schmidt. I would also like to thank the various anonymous reviewers who have helped to strengthen this dissertation. This dissertation was supported by the National Science Foundation under Grant No. AGS-1752900, and NOAA's Climate Program Office's Modeling, Analysis, Predictions, and Projections program (grants NA19OAR4310293 and NA21OAR4310476). I acknowledge the World Climate Research Programme, which coordinated and promoted CMIP6, and thank the climate modeling groups for producing and making available their model output, the Earth System Grid Federation (ESGF) for archiving the data and providing access, and the multiple funding agencies who support CMIP6 and ESGF.

References

Acero, F. J., García, J. A., Gallego, M. C., Parey, S., & Dacunha-Castelle, D. (2014). Trends in summer extreme temperatures over the Iberian Peninsula using nonurban station data. *Journal of Geophysical Research: Atmospheres*, *119*(1), 39–53. https://doi.org/10.1002/2013JD020590

Adam, O., Grise, K. M., Staten, P., Simpson, I. R., Davis, S. M., Davis, N. A., et al. (2018). The TropD software package (v1): standardized methods for calculating tropical-width diagnostics. *Geoscientific Model Development*, *11*(10), 4339–4357. https://doi.org/10.5194/gmd-11-4339-2018

Andrews, T., Gregory, J. M., Webb, M. J., & Taylor, K. E. (2012). Forcing, feedbacks and climate sensitivity in CMIP5 coupled atmosphere-ocean climate models. *Geophysical Research Letters*, *39*(9). https://doi.org/10.1029/2012GL051607

Barnes, E. A., & Polvani, L. (2013). Response of the Midlatitude Jets, and of Their Variability, to Increased Greenhouse Gases in the CMIP5 Models. *Journal of Climate*, *26*(18), 7117–7135. https://doi.org/10.1175/JCLI-D-12-00536.1

Bellomo, K., Angeloni, M., Corti, S., & von Hardenberg, J. (2021). Future climate change shaped by inter-model differences in Atlantic meridional overturning circulation response. *Nature Communications*, *12*(1), 3659. https://doi.org/10.1038/s41467-021-24015-w

Bender, F. A.-M., Ramanathan, V., & Tselioudis, G. (2012). Changes in extratropical storm track cloudiness 1983–2008: observational support for a poleward shift. *Climate Dynamics*, *38*(9), 2037–2053. https://doi.org/10.1007/s00382-011-1065-6

Bony, S., Stevens, B., Frierson, D. M. W., Jakob, C., Kageyama, M., Pincus, R., et al. (2015). Clouds, circulation and climate sensitivity. *Nature Geoscience*, *8*(4), 261–268. https://doi.org/10.1038/ngeo2398

Boucher, O., D. Randall, P. Artaxo, C. Bretherton, G. Feingold, P. Forster, V.-M. Kerminen, Y. Kondo, H. Liao, U. Lohmann, P. Rasch, S.K. Satheesh, S. Sherwood, B. Stevens and X.Y. Zhang, 2013: Clouds and Aerosols. In: Climate Change 2013: The Physical Science Basis. Contribution of Working Group I to the Fifth Assessment Report of the Intergovernmental Panel on Climate Change [Stocker, T.F., D. Qin, G.-K. Plattner, M. Tignor, S.K. Allen, J. Boschung, A. Nauels, Y. Xia, V. Bex and P.M. Midgley (eds.)]. Cambridge University Press, Cambridge, United Kingdom and New York, NY, USA.

Booth, J. F., Naud, C. M., & Del Genio, A. D. (2013). Diagnosing Warm Frontal Cloud Formation in a GCM: A Novel Approach Using Conditional Subsetting. *Journal of Climate*, *26*(16), 5827–5845. https://doi.org/10.1175/JCLI-D-12-00637.1

Boucher, O., Denvil, S., Levavasseur, G., Cozic, A., Caubel, A., Foujols, M.-A., et al. (2019). IPSL IPSL-CM6A-LR model output prepared for CMIP6 ScenarioMIP [Data set]. Earth System Grid Federation. https://doi.org/10.22033/ESGF/CMIP6.1532

Bretherton, C. S., & Wyant, M. C. (1997). Moisture Transport, Lower-Tropospheric Stability, and Decoupling of Cloud-Topped Boundary Layers. *Journal of the Atmospheric Sciences*, *54*(1), 148–167. https://doi.org/10.1175/1520-0469(1997)054<0148:MTLTSA>2.0.CO;2

Byrne, M. P., & O'Gorman, P. A. (2013). Link between land-ocean warming contrast and surface relative humidities in simulations with coupled climate models. *Geophysical Research Letters*, *40*(19), 5223–5227. https://doi.org/10.1002/grl.50971

Cavanaugh, N. R., & Shen, S. S. P. (2014). Northern Hemisphere Climatology and Trends of Statistical Moments Documented from GHCN-Daily Surface Air Temperature Station Data from 1950 to 2010. *Journal of Climate*, *27*(14), 5396–5410. https://doi.org/10.1175/JCLI-D-13-00470.1

Ceppi, P., & Hartmann, D. L. (2015). Connections Between Clouds, Radiation, and Midlatitude Dynamics: a Review. *Current Climate Change Reports*, *1*(2), 94–102. https://doi.org/10.1007/s40641-015-0010-x

Ceppi, P., Hwang, Y.-T., Frierson, D. M. W., & Hartmann, D. L. (2012). Southern Hemisphere jet latitude biases in CMIP5 models linked to shortwave cloud forcing. *Geophysical Research Letters*, *39*(19), L19708. https://doi.org/10.1029/2012GL053115

Ceppi, P., Zelinka, M. D., & Hartmann, D. L. (2014). The response of the Southern Hemispheric eddy-driven jet to future changes in shortwave radiation in CMIP5. *Geophysical Research Letters*, *41*(9), 3244–3250. https://doi.org/10.1002/2014GL060043

Ceppi, P., Hartmann, D. L., & Webb, M. J. (2016). Mechanisms of the Negative Shortwave Cloud Feedback in Middle to High Latitudes. *Journal of Climate*, *29*(1), 139–157. https://doi.org/10.1175/JCLI-D-15-0327.1

Christensen, M. W., Carrió, G. G., Stephens, G. L., & Cotton, W. R. (2013). Radiative Impacts of Free-Tropospheric Clouds on the Properties of Marine Stratocumulus. *Journal of the Atmospheric Sciences*, *70*(10), 3102–3118. https://doi.org/10.1175/JAS-D-12-0287.1

Deser, C., Lehner, F., Rodgers, K. B., Ault, T., Delworth, T. L., DiNezio, P. N., et al. (2020). Insights from Earth system model initial-condition large ensembles and future prospects. *Nature Climate Change*, *10*(4), 277–286. https://doi.org/10.1038/s41558-020-0731-2

Deser, Clara, Phillips, A., Bourdette, V., & Teng, H. (2012). Uncertainty in climate change projections: the role of internal variability. *Climate Dynamics*, *38*(3), 527–546. https://doi.org/10.1007/s00382-010-0977-x

Deser, Clara, Phillips, A. S., Alexander, M. A., & Smoliak, B. V. (2014). Projecting North American Climate over the Next 50 Years: Uncertainty due to Internal Variability. *Journal of Climate*, *27*(6), 2271–2296. https://doi.org/10.1175/JCLI-D-13-00451.1

Diro, G. T., Sushama, L., & Huziy, O. (2018). Snow-atmosphere coupling and its impact on temperature variability and extremes over North America. *Climate Dynamics*, *50*(7), 2993–3007. https://doi.org/10.1007/s00382-017-3788-5

Dix, M., Bi, D., Dobrohotoff, P., Fiedler, R., Harman, I., Law, R., et al. (2019). CSIRO-ARCCSS ACCESS-CM2 model output prepared for CMIP6 ScenarioMIP [Data set]. Earth System Grid Federation. https://doi.org/10.22033/ESGF/CMIP6.2285

Draper, N. R., & Smith, H. (1998). Extra Sums of Squares and Tests for Several Parameters Being Zero. In *Applied Regression Analysis* (pp. 149–177). John Wiley & Sons, Ltd. https://doi.org/10.1002/9781118625590.ch6

EC-Earth Consortium (EC-Earth). (2019a). EC-Earth-Consortium EC-Earth3 model output prepared for CMIP6 ScenarioMIP [Data set]. Earth System Grid Federation. https://doi.org/10.22033/ESGF/CMIP6.251

EC-Earth Consortium (EC-Earth). (2019b). EC-Earth-Consortium EC-Earth3-Veg model output prepared for CMIP6 ScenarioMIP [Data set]. Earth System Grid Federation. https://doi.org/10.22033/ESGF/CMIP6.727

Eyring, V., Bony, S., Meehl, G. A., Senior, C. A., Stevens, B., Stouffer, R. J., & Taylor, K. E. (2016). Overview of the Coupled Model Intercomparison Project Phase 6 (CMIP6)

experimental design and organization. *Geoscientific Model Development*, *9*(5), 1937–1958. https://doi.org/10.5194/gmd-9-1937-2016

Fischer, E. M., Beyerle, U., & Knutti, R. (2013). Robust spatially aggregated projections of climate extremes. *Nature Climate Change*, *3*(12), 1033–1038. https://doi.org/10.1038/nclimate2051

Fischer, E. M., Sedláček, J., Hawkins, E., & Knutti, R. (2014). Models agree on forced response pattern of precipitation and temperature extremes. *Geophysical Research Letters*, *41*(23), 8554–8562. https://doi.org/10.1002/2014GL062018

Forster, P. M., Andrews, T., Good, P., Gregory, J. M., Jackson, L. S., & Zelinka, M. (2013). Evaluating adjusted forcing and model spread for historical and future scenarios in the CMIP5 generation of climate models. *Journal of Geophysical Research: Atmospheres*, *118*(3), 1139–1150. https://doi.org/10.1002/jgrd.50174

Frey, W. R., & Kay, J. E. (2017). The influence of extratropical cloud phase and amount feedbacks on climate sensitivity. *Climate Dynamics*, 1–20. https://doi.org/10.1007/s00382-017-3796-5

Gao, Y., Leung, L. R., Lu, J., & Masato, G. (2015). Persistent cold air outbreaks over North America in a warming climate. *Environmental Research Letters*, *10*(4), 044001. https://doi.org/10.1088/1748-9326/10/4/044001

Garfinkel, C. I., & Harnik, N. (2017). The Non-Gaussianity and Spatial Asymmetry of Temperature Extremes Relative to the Storm Track: The Role of Horizontal Advection. *Journal of Climate*, *30*(2), 445–464. https://doi.org/10.1175/JCLI-D-15-0806.1

Georgakakos, K. P., & Bras, R. L. (1984). A hydrologically useful station precipitation model: 1. Formulation. *Water Resources Research*, *20*(11), 1585–1596. https://doi.org/10.1029/WR020i011p01585

Gillett, N. P., & Thompson, D. W. J. (2003). Simulation of Recent Southern Hemisphere Climate Change. *Science*, *302*(5643), 273–275. https://doi.org/10.1126/science.1087440

Giorgi, F., & Bi, X. (2009). Time of emergence (TOE) of GHG-forced precipitation change hot-spots. *Geophysical Research Letters*, *36*(6). https://doi.org/10.1029/2009GL037593

Good, P., Sellar, A., Tang, Y., Rumbold, S., Ellis, R., Kelley, D., et al. (2019). MOHC UKESM1.0-LL model output prepared for CMIP6 ScenarioMIP [Data set]. Earth System Grid Federation. https://doi.org/10.22033/ESGF/CMIP6.1567

Gordon, N. D., & Klein, S. A. (2014). Low-cloud optical depth feedback in climate models. *Journal of Geophysical Research: Atmospheres*, *119*(10), 6052–6065. https://doi.org/10.1002/2013JD021052

Gordon, N. D., Norris, J. R., Weaver, C. P., & Klein, S. A. (2005). Cluster analysis of cloud regimes and characteristic dynamics of midlatitude synoptic systems in observations and a model. *Journal of Geophysical Research: Atmospheres*, *110*(D15). https://doi.org/10.1029/2004JD005027

Govekar, P. D., Jakob, C., & Catto, J. (2014). The relationship between clouds and dynamics in Southern Hemisphere extratropical cyclones in the real world and a climate model. *Journal of Geophysical Research: Atmospheres*, *119*(11), 6609–6628. https://doi.org/10.1002/2013JD020699

Grise, K. M. (n.d.). Atmospheric circulation constraints on 21st century seasonal precipitation storylines for the southwestern United States. *Geophysical Research Letters*, *n/a*(n/a), e2022GL099443. https://doi.org/10.1029/2022GL099443

Grise, K. M., & Kelleher, M. K. (2021). Midlatitude Cloud Radiative Effect Sensitivity to Cloud Controlling Factors in Observations and Models: Relationship with Southern Hemisphere Jet Shifts and Climate Sensitivity. *Journal of Climate*, *34*(14), 5869–5886. https://doi.org/10.1175/JCLI-D-20-0986.1

Grise, K. M., & Medeiros, B. (2016). Understanding the Varied Influence of Midlatitude Jet Position on Clouds and Cloud Radiative Effects in Observations and Global Climate Models. *Journal of Climate*, *29*(24), 9005–9025. https://doi.org/10.1175/JCLI-D-16-0295.1

Grise, K. M., & Polvani, L. M. (2014). Southern Hemisphere Cloud–Dynamics Biases in CMIP5 Models and Their Implications for Climate Projections. *Journal of Climate*, *27*(15), 6074–6092. https://doi.org/10.1175/JCLI-D-14-00113.1

Grise, K. M., Polvani, L. M., Tselioudis, G., Wu, Y., & Zelinka, M. D. (2013). The ozone hole indirect effect: Cloud-radiative anomalies accompanying the poleward shift of the eddy-driven jet in the Southern Hemisphere. *Geophysical Research Letters*, *40*(14), 3688–3692. https://doi.org/10.1002/grl.50675

Hartmann, D. L. (2016). Tropical anvil clouds and climate sensitivity. *Proceedings of the National Academy of Sciences*, *113*(32), 8897–8899. https://doi.org/10.1073/pnas.1610455113

Harvey, B. J., Cook, P., Shaffrey, L. C., & Schiemann, R. (2020). The Response of the Northern Hemisphere Storm Tracks and Jet Streams to Climate Change in the CMIP3, CMIP5, and

CMIP6 Climate Models. *Journal of Geophysical Research: Atmospheres*, *125*(23), e2020JD032701. https://doi.org/10.1029/2020JD032701

Hawkins, E., & Sutton, R. (2009). The Potential to Narrow Uncertainty in Regional Climate Predictions. *Bulletin of the American Meteorological Society*, *90*(8), 1095–1108. https://doi.org/10.1175/2009BAMS2607.1

Held, I. M., & Soden, B. J. (2006). Robust Responses of the Hydrological Cycle to Global Warming. *Journal of Climate*, *19*(21), 5686–5699. https://doi.org/10.1175/JCLI3990.1

Hersbach, H., Bell, B., Berrisford, P., Hirahara, S., Horányi, A., Muñoz-Sabater, J., et al. (2020). The ERA5 global reanalysis. *Quarterly Journal of the Royal Meteorological Society*, *146*(730), 1999–2049. https://doi.org/10.1002/qj.3803

Holland, M. M., & Bitz, C. M. (2003). Polar amplification of climate change in coupled models. *Climate Dynamics*, *21*(3), 221–232. https://doi.org/10.1007/s00382-003-0332-6

Hurrell, J. W. (1995). Decadal Trends in the North Atlantic Oscillation: Regional Temperatures and Precipitation. *Science*, *269*(5224), 676–679. https://doi.org/10.1126/science.269.5224.676

Hurrell, J. W., Kushnir, Y., Ottersen, G., & Visbeck, M. (2003). An Overview of the North Atlantic Oscillation. In *The North Atlantic Oscillation: Climatic Significance and Environmental Impact* (pp. 1–35). American Geophysical Union (AGU). https://doi.org/10.1029/134GM01

Hwang, Y.-T., & Frierson, D. M. W. (2013). Link between the double-Intertropical Convergence Zone problem and cloud biases over the Southern Ocean. *Proceedings of the National Academy of Sciences*, *110*(13), 4935–4940. https://doi.org/10.1073/pnas.1213302110

James, R., Washington, R., Schleussner, C.-F., Rogelj, J., & Conway, D. (2017). Characterizing half-a-degree difference: a review of methods for identifying regional climate responses to global warming targets. *WIREs Climate Change*, *8*(2), e457. https://doi.org/10.1002/wcc.457

Janssen, E., Sriver, R. L., Wuebbles, D. J., & Kunkel, K. E. (2016). Seasonal and regional variations in extreme precipitation event frequency using CMIP5. *Geophysical Research Letters*, *43*(10), 5385–5393. https://doi.org/10.1002/2016GL069151

Janssen, Emily, Wuebbles, D. J., Kunkel, K. E., Olsen, S. C., & Goodman, A. (2014). Observational- and model-based trends and projections of extreme precipitation over the contiguous United States. *Earth's Future*, *2*(2), 99–113. https://doi.org/10.1002/2013EF000185

Kang, S. M., & Polvani, L. M. (2011). The Interannual Relationship between the Latitude of the Eddy-Driven Jet and the Edge of the Hadley Cell. *Journal of Climate*, *24*(2), 563–568. https://doi.org/10.1175/2010JCLI4077.1

Kelleher, M. K., & Grise, K. M. (2019). Examining Southern Ocean Cloud Controlling Factors on Daily Time Scales and Their Connections to Midlatitude Weather Systems. *Journal of Climate*, *32*(16), 5145–5160. https://doi.org/10.1175/JCLI-D-18-0840.1

Kelleher, M. K., Grise, K. M., & Schmidt, D. F. (2023). Variability in Projected North American Mean and Extreme Temperature and Precipitation Trends for the 21st Century: Model-To-Model Differences Versus Internal Variability. *Earth's Future*, *11*(3), e2022EF003161. https://doi.org/10.1029/2022EF003161

Klein, S. A., & Hartmann, D. L. (1993). The Seasonal Cycle of Low Stratiform Clouds. *Journal of Climate*, *6*(8), 1587–1606. https://doi.org/10.1175/1520-0442(1993)006<1587:TSCOLS>2.0.CO;2

Klein, S. A., Hall, A., Norris, J. R., & Pincus, R. (2017). Low-Cloud Feedbacks from Cloud-Controlling Factors: A Review. *Surveys in Geophysics*, *38*(6), 1307–1329. https://doi.org/10.1007/s10712-017-9433-3

Kunkel, K. E., Karl, T. R., Easterling, D. R., Redmond, K., Young, J., Yin, X., & Hennon, P. (2013). Probable maximum precipitation and climate change. *Geophysical Research Letters*, *40*(7), 1402–1408. https://doi.org/10.1002/grl.50334

Kushner, P. J., Held, I. M., & Delworth, T. L. (2001). Southern Hemisphere Atmospheric Circulation Response to Global Warming. *Journal of Climate*, *14*(10), 2238–2249. https://doi.org/10.1175/1520-0442(2001)014<0001:SHACRT>2.0.CO;2

Lau, N.-C., & Crane, M. W. (1995). A Satellite View of the Synoptic-Scale Organization of Cloud Properties in Midlatitude and Tropical Circulation Systems. *Monthly Weather Review*, *123*(7), 1984–2006. https://doi.org/10.1175/1520-0493(1995)123<1984:ASVOTS>2.0.CO;2

Lau, N.-C., & Crane, M. W. (1997). Comparing Satellite and Surface Observations of Cloud Patterns in Synoptic-Scale Circulation Systems. *Monthly Weather Review*, *125*(12), 3172–3189. https://doi.org/10.1175/1520-0493(1997)125<3172:CSASOO>2.0.CO;2

Leathers, D. J., Yarnal, B., & Palecki, M. A. (1991). The Pacific/North American Teleconnection Pattern and United States Climate. Part I: Regional Temperature and Precipitation Associations. *Journal of Climate*, *4*(5), 517–528. https://doi.org/10.1175/1520-0442(1991)004<0517:TPATPA>2.0.CO;2

Lehner, F., Deser, C., Maher, N., Marotzke, J., Fischer, E. M., Brunner, L., et al. (2020). Partitioning climate projection uncertainty with multiple large ensembles and CMIP5/6. *Earth System Dynamics*, *11*(2), 491–508. https://doi.org/10.5194/esd-11-491-2020

Li, C., Zwiers, F., Zhang, X., Li, G., Sun, Y., & Wehner, M. (2021). Changes in Annual Extremes of Daily Temperature and Precipitation in CMIP6 Models. *Journal of Climate*, *34*(9), 3441–3460. https://doi.org/10.1175/JCLI-D-19-1013.1

Li, L. (2019). CAS FGOALS-g3 model output prepared for CMIP6 ScenarioMIP [Data set]. Earth System Grid Federation. https://doi.org/10.22033/ESGF/CMIP6.2056

Li, Y., Thompson, D. W. J., Stephens, G. L., & Bony, S. (2014). A global survey of the instantaneous linkages between cloud vertical structure and large-scale climate. *Journal of Geophysical Research: Atmospheres*, *119*(7), 3770–3792. https://doi.org/10.1002/2013JD020669

Li, Y., Thompson, D. W. J., Huang, Y., & Zhang, M. (2014). Observed linkages between the northern annular mode/North Atlantic Oscillation, cloud incidence, and cloud radiative forcing. *Geophysical Research Letters*, *41*(5), 1681–1688. https://doi.org/10.1002/2013GL059113

Linz, M., Chen, G., Zhang, B., & Zhang, P. (2020). A Framework for Understanding How Dynamics Shape Temperature Distributions. *Geophysical Research Letters*, *47*(4), e2019GL085684. https://doi.org/10.1029/2019GL085684

Lipat, B. R., Tselioudis, G., Grise, K. M., & Polvani, L. M. (2017). CMIP5 models' shortwave cloud radiative response and climate sensitivity linked to the climatological Hadley cell extent. *Geophysical Research Letters*, *44*(11), 5739–5748. https://doi.org/10.1002/2017GL073151

Lipat, B. R., Voigt, A., Tselioudis, G., & Polvani, L. M. (2018). Model Uncertainty in Cloud–Circulation Coupling, and Cloud-Radiative Response to Increasing CO2, Linked to Biases in Climatological Circulation. *Journal of Climate*, *31*(24), 10013–10020. https://doi.org/10.1175/JCLI-D-17-0665.1

Loeb, N. G., Doelling, D. R., Wang, H., Su, W., Nguyen, C., Corbett, J. G., et al. (2017). Clouds and the Earth's Radiant Energy System (CERES) Energy Balanced and Filled (EBAF) Top-of-Atmosphere (TOA) Edition-4.0 Data Product. *Journal of Climate*, *31*(2), 895–918. https://doi.org/10.1175/JCLI-D-17-0208.1

Lorenz, E. N. (1963). Deterministic Nonperiodic Flow. *Journal of the Atmospheric Sciences*, *20*(2), 130–141. https://doi.org/10.1175/1520-0469(1963)020<0130:DNF>2.0.CO;2

Lu, J., Vecchi, G. A., & Reichler, T. (2007). Expansion of the Hadley cell under global warming. *Geophysical Research Letters*, *34*(6). https://doi.org/10.1029/2006GL028443

Maher, N., Power, S. B., & Marotzke, J. (2021). More accurate quantification of model-to-model agreement in externally forced climatic responses over the coming century. *Nature Communications*, *12*(1), 788. https://doi.org/10.1038/s41467-020-20635-w

McCoy, D. T., Tan, I., Hartmann, D. L., Zelinka, M. D., & Storelvmo, T. (2016). On the relationships among cloud cover, mixed-phase partitioning, and planetary albedo in GCMs. *Journal of Advances in Modeling Earth Systems*, *8*(2), 650–668. https://doi.org/10.1002/2015MS000589

McCoy, D. T., Eastman, R., Hartmann, D. L., & Wood, R. (2017). The Change in Low Cloud Cover in a Warmed Climate Inferred from AIRS, MODIS, and ERA-Interim. *Journal of Climate*, *30*(10), 3609–3620. https://doi.org/10.1175/JCLI-D-15-0734.1

McCoy, D. T., Field, P., Frazer, M. E., Zelinka, M. D., Elsaesser, G. S., Mülmenstädt, J., et al. (2022). Extratropical Shortwave Cloud Feedbacks in the Context of the Global Circulation and Hydrological Cycle. *Geophysical Research Letters*, *49*(8), e2021GL097154. https://doi.org/10.1029/2021GL097154

McKinnon, K. A., & Deser, C. (2018). Internal Variability and Regional Climate Trends in an Observational Large Ensemble. *Journal of Climate*, *31*(17), 6783–6802. https://doi.org/10.1175/JCLI-D-17-0901.1

McKinnon, K. A., Rhines, A., Tingley, M. P., & Huybers, P. (2016). The changing shape of Northern Hemisphere summer temperature distributions. *Journal of Geophysical Research: Atmospheres*, *121*(15), 8849–8868. https://doi.org/10.1002/2016JD025292

Meehl, G. A., Senior, C. A., Eyring, V., Flato, G., Lamarque, J.-F., Stouffer, R. J., et al. (2020). Context for interpreting equilibrium climate sensitivity and transient climate response from the CMIP6 Earth system models. *Science Advances*, *6*(26), eaba1981. https://doi.org/10.1126/sciadv.aba1981

Michaelis, A. C., Willison, J., Lackmann, G. M., & Robinson, W. A. (2017). Changes in Winter North Atlantic Extratropical Cyclones in High-Resolution Regional Pseudo–Global Warming Simulations. *Journal of Climate*, *30*(17), 6905–6925. https://doi.org/10.1175/JCLI-D-16-0697.1

Miyamoto, A., Nakamura, H., & Miyasaka, T. (2018). Influence of the Subtropical High and Storm Track on Low-Cloud Fraction and Its Seasonality over the South Indian Ocean. *Journal of Climate*, *31*(10), 4017–4039. https://doi.org/10.1175/JCLI-D-17-0229.1

Myers, T. A., & Norris, J. R. (2013a). Observational Evidence That Enhanced Subsidence Reduces Subtropical Marine Boundary Layer Cloudiness. *Journal of Climate*, *26*(19), 7507–7524. https://doi.org/10.1175/JCLI-D-12-00736.1

Myers, T. A., & Norris, J. R. (2013b). Observational Evidence That Enhanced Subsidence Reduces Subtropical Marine Boundary Layer Cloudiness. *Journal of Climate*, *26*(19), 7507–7524. https://doi.org/10.1175/JCLI-D-12-00736.1

Myers, T. A., & Norris, J. R. (2014). On the Relationships between Subtropical Clouds and Meteorology in Observations and CMIP3 and CMIP5 Models. *Journal of Climate*, *28*(8), 2945–2967. https://doi.org/10.1175/JCLI-D-14-00475.1

Myers, T. A., & Norris, J. R. (2016). Reducing the uncertainty in subtropical cloud feedback. *Geophysical Research Letters*, *43*(5), 2015GL067416. https://doi.org/10.1002/2015GL067416

NASA/GISS. (2020a). (2020a). NASA-GISS GISS-E2.1G model output prepared for CMIP6 ScenarioMIP [Data set]. Earth System Grid Federation. https://doi.org/10.22033/ESGF/CMIP6.2074

NASA/GISS. (2020a). (2020b). NASA-GISS GISS-E2.1H model output prepared for CMIP6 ScenarioMIP [Data set]. Earth System Grid Federation. https://doi.org/10.22033/ESGF/CMIP6.2080

Naud, C. M., Booth, J. F., & Del Genio, A. D. (2016). The Relationship between Boundary Layer Stability and Cloud Cover in the Post-Cold-Frontal Region. *Journal of Climate*, *29*(22), 8129–8149. https://doi.org/10.1175/JCLI-D-15-0700.1

Nguyen, H., Evans, A., Lucas, C., Smith, I., & Timbal, B. (2013). The Hadley Circulation in Reanalyses: Climatology, Variability, and Change. *Journal of Climate*, *26*(10), 3357–3376. https://doi.org/10.1175/JCLI-D-12-00224.1

Norris, J. R., & Iacobellis, S. F. (2005). North Pacific Cloud Feedbacks Inferred from Synoptic-Scale Dynamic and Thermodynamic Relationships. *Journal of Climate*, *18*(22), 4862–4878. https://doi.org/10.1175/JCLI3558.1

O'Neill, B. C., Tebaldi, C., van Vuuren, D. P., Eyring, V., Friedlingstein, P., Hurtt, G., et al. (2016). The Scenario Model Intercomparison Project (ScenarioMIP) for CMIP6. *Geoscientific Model Development*, *9*(9), 3461–3482. https://doi.org/10.5194/gmd-9-3461-2016

Pascale, S., Lucarini, V., Feng, X., Porporato, A., & ul Hasson, S. (2016). Projected changes of rainfall seasonality and dry spells in a high greenhouse gas emissions scenario. *Climate Dynamics*, *46*(3), 1331–1350. https://doi.org/10.1007/s00382-015-2648-4

Pathmeswaran, C., Sen Gupta, A., Perkins-Kirkpatrick, S. E., & Hart, M. A. (2022). Exploring Potential Links Between Co-occurring Coastal Terrestrial and Marine Heatwaves in Australia. *Frontiers in Climate*, *4*. Retrieved from https://www.frontiersin.org/article/10.3389/fclim.2022.792730

Pendergrass, A. G., Lehner, F., Sanderson, B. M., & Xu, Y. (2015). Does extreme precipitation intensity depend on the emissions scenario? *Geophysical Research Letters*, *42*(20), 8767–8774. https://doi.org/10.1002/2015GL065854

Pendergrass, A. G., Knutti, R., Lehner, F., Deser, C., & Sanderson, B. M. (2017). Precipitation variability increases in a warmer climate. *Scientific Reports*, *7*(1), 17966. https://doi.org/10.1038/s41598-017-17966-y

Perkins, S. E., & Alexander, L. V. (2013). On the Measurement of Heat Waves. *Journal of Climate*, *26*(13), 4500–4517. https://doi.org/10.1175/JCLI-D-12-00383.1

Peterson, T. C., Heim, R. R., Hirsch, R., Kaiser, D. P., Brooks, H., Diffenbaugh, N. S., et al. (2013). Monitoring and Understanding Changes in Heat Waves, Cold Waves, Floods, and Droughts in the United States: State of Knowledge. *Bulletin of the American Meteorological Society*, *94*(6), 821–834. https://doi.org/10.1175/BAMS-D-12-00066.1

Pithan, F., & Mauritsen, T. (2014). Arctic amplification dominated by temperature feedbacks in contemporary climate models. *Nature Geoscience*, *7*(3), 181–184. https://doi.org/10.1038/ngeo2071

Plecha, S. M., & Soares, P. M. M. (2020). Global marine heatwave events using the new CMIP6 multi-model ensemble: from shortcomings in present climate to future projections. *Environmental Research Letters*, *15*(12), 124058. https://doi.org/10.1088/1748-9326/abc847

Polvani, L. M., Waugh, D. W., Correa, G. J. P., & Son, S.-W. (2010). Stratospheric Ozone Depletion: The Main Driver of Twentieth-Century Atmospheric Circulation Changes in the Southern Hemisphere. *Journal of Climate*, *24*(3), 795–812. https://doi.org/10.1175/2010JCLI3772.1

Priestley, M. D. K., & Catto, J. L. (2022). Future changes in the extratropical storm tracks and cyclone intensity, wind speed, and structure. *Weather and Climate Dynamics*, *3*(1), 337–360. https://doi.org/10.5194/wcd-3-337-2022

Qu, X., Hall, A., Klein, S. A., & Caldwell, P. M. (2014). On the spread of changes in marine low cloud cover in climate model simulations of the 21st century. *Climate Dynamics*, *42*(9), 2603–2626. https://doi.org/10.1007/s00382-013-1945-z

Qu, X., Hall, A., Klein, S. A., & DeAngelis, A. M. (2015). Positive tropical marine low-cloud cover feedback inferred from cloud-controlling factors. *Geophysical Research Letters*, *42*(18), 7767–7775. https://doi.org/10.1002/2015GL065627

Schär, C., Vidale, P. L., Lüthi, D., Frei, C., Häberli, C., Liniger, M. A., & Appenzeller, C. (2004). The role of increasing temperature variability in European summer heatwaves. *Nature*, *427*(6972), 332–336. https://doi.org/10.1038/nature02300

Scheff, J., & Frierson, D. (2012). Twenty-First-Century Multimodel Subtropical Precipitation Declines Are Mostly Midlatitude Shifts. *Journal of Climate*, *25*(12), 4330–4347. https://doi.org/10.1175/JCLI-D-11-00393.1

Schmidt, D. F., & Grise, K. M. (2021). Drivers of Twenty-First-Century U.S. Winter Precipitation Trends in CMIP6 Models: A Storyline-Based Approach. *Journal of Climate*, *34*(16), 6875–6889. https://doi.org/10.1175/JCLI-D-21-0080.1

Schneider, T., Bischoff, T., & Płotka, H. (2015). Physics of Changes in Synoptic Midlatitude Temperature Variability. *Journal of Climate*, *28*(6), 2312–2331. https://doi.org/10.1175/JCLI-D-14-00632.1

Schupfner, M., Wieners, K.-H., Wachsmann, F., Steger, C., Bittner, M., Jungclaus, J., et al. (2019). DKRZ MPI-ESM1.2-HR model output prepared for CMIP6 ScenarioMIP [Data set]. Earth System Grid Federation. https://doi.org/10.22033/ESGF/CMIP6.2450

Screen, J. A. (2014). Arctic amplification decreases temperature variance in northern mid- to high-latitudes. *Nature Climate Change*, *4*(7), 577–582. https://doi.org/10.1038/nclimate2268

Seager, R., Naik, N., & Vecchi, G. A. (2010). Thermodynamic and Dynamic Mechanisms for Large-Scale Changes in the Hydrological Cycle in Response to Global Warming. *Journal of Climate*, *23*(17), 4651–4668. https://doi.org/10.1175/2010JCLI3655.1

Seethala, C., Norris, J. R., & Myers, T. A. (2015). How Has Subtropical Stratocumulus and Associated Meteorology Changed since the 1980s? *Journal of Climate*, *28*(21), 8396–8410. https://doi.org/10.1175/JCLI-D-15-0120.1

Seferian, R. (2019). CNRM-CERFACS CNRM-ESM2-1 model output prepared for CMIP6 ScenarioMIP [Data set]. Earth System Grid Federation. https://doi.org/10.22033/ESGF/CMIP6.1395

Seneviratne, S.I., X. Zhang, M. Adnan, W. Badi, C. Dereczynski, A. Di Luca et al. (2021). Weather and Climate Extreme Events in a Changing Climate. In *Climate Change 2021: The Physical Science Basis. Contribution of Working Group I to the Sixth Assessment Report of the Intergovernmental Panel on Climate Change* (pp. 1513–1766) Cambridge, United Kingdom and New York, NY, USA: Cambridge University Press. doi:10.1017/9781009157896.013.

Semmler, T., Danilov, S., Rackow, T., Sidorenko, D., Barbi, D., Hegewald, J., et al. (2019). AWI AWI-CM1.1MR model output prepared for CMIP6 ScenarioMIP [Data set]. Earth System Grid Federation. https://doi.org/10.22033/ESGF/CMIP6.376

Shepherd, T. G. (2019). Storyline approach to the construction of regional climate change information. *Proceedings of the Royal Society A: Mathematical, Physical and Engineering Sciences*, *475*(2225), 20190013. https://doi.org/10.1098/rspa.2019.0013

Shepherd, T. G., Boyd, E., Calel, R. A., Chapman, S. C., Dessai, S., Dima-West, I. M., et al. (2018). Storylines: an alternative approach to representing uncertainty in physical aspects of

climate change. *Climatic Change*, *151*(3), 555–571. https://doi.org/10.1007/s10584-018-2317-9

Sherwood, S. C., Webb, M. J., Annan, J. D., Armour, K. C., Forster, P. M., Hargreaves, J. C., et al. (2020). An Assessment of Earth's Climate Sensitivity Using Multiple Lines of Evidence. *Reviews of Geophysics*, *58*(4), e2019RG000678. https://doi.org/10.1029/2019RG000678

Sillmann, J., Kharin, V. V., Zwiers, F. W., Zhang, X., & Bronaugh, D. (2013). Climate extremes indices in the CMIP5 multimodel ensemble: Part 2. Future climate projections. *Journal of Geophysical Research: Atmospheres*, *118*(6), 2473–2493. https://doi.org/10.1002/jgrd.50188

Simolo, C., Brunetti, M., Maugeri, M., & Nanni, T. (2011). Evolution of extreme temperatures in a warming climate. *Geophysical Research Letters*, *38*(16). https://doi.org/10.1029/2011GL048437

Simpson, I. R., Bacmeister, J., Neale, R. B., Hannay, C., Gettelman, A., Garcia, R. R., et al. (2020). An Evaluation of the Large-Scale Atmospheric Circulation and Its Variability in CESM2 and Other CMIP Models. *Journal of Geophysical Research: Atmospheres*, *125*(13), e2020JD032835. https://doi.org/10.1029/2020JD032835

Sinclair, V. A., Rantanen, M., Haapanala, P., Räisänen, J., & Järvinen, H. (2020). The characteristics and structure of extra-tropical cyclones in a warmer climate. *Weather and Climate Dynamics*, *1*(1), 1–25. https://doi.org/10.5194/wcd-1-1-2020

Suarez-Gutierrez, L., Milinski, S., & Maher, N. (2021). Exploiting large ensembles for a better yet simpler climate model evaluation. *Climate Dynamics*, *57*(9), 2557–2580. https://doi.org/10.1007/s00382-021-05821-w

Sutton, R. T., Dong, B., & Gregory, J. M. (2007). Land/sea warming ratio in response to climate change: IPCC AR4 model results and comparison with observations. *Geophysical Research Letters*, *34*(2). https://doi.org/10.1029/2006GL028164

Swain, D. L., Langenbrunner, B., Neelin, J. D., & Hall, A. (2018). Increasing precipitation volatility in twenty-first-century California. *Nature Climate Change*, *8*(5), 427–433. https://doi.org/10.1038/s41558-018-0140-y

Swart, N. C., Cole, J. N. S., Kharin, V. V., Lazare, M., Scinocca, J. F., Gillett, N. P., et al. (2019). CCCma CanESM5 model output prepared for CMIP6 ScenarioMIP [Data set]. Earth System Grid Federation. https://doi.org/10.22033/ESGF/CMIP6.1317

Tachiiri, K., Abe, M., Hajima, T., Arakawa, O., Suzuki, T., Komuro, Y., et al. (2019). MIROC MIROC-ES2L model output prepared for CMIP6 ScenarioMIP [Data set]. Earth System Grid Federation. https://doi.org/10.22033/ESGF/CMIP6.936

Tamarin-Brodsky, T., Hodges, K., Hoskins, B. J., & Shepherd, T. G. (2019). A Dynamical Perspective on Atmospheric Temperature Variability and Its Response to Climate Change. *Journal of Climate*, *32*(6), 1707–1724. https://doi.org/10.1175/JCLI-D-18-0462.1

Tamarin-Brodsky, T., Hodges, K., Hoskins, B. J., & Shepherd, T. G. (2020). Changes in Northern Hemisphere temperature variability shaped by regional warming patterns. *Nature Geoscience*, *13*(6), 414–421. https://doi.org/10.1038/s41561-020-0576-3

Tamarin-Brodsky, T., Hodges, K., Hoskins, B. J., & Shepherd, T. G. (2022). A Simple Model for Interpreting Temperature Variability and Its Higher-Order Changes. *Journal of Climate*, *35*(1), 387–403. https://doi.org/10.1175/JCLI-D-21-0310.1

Tan, I., Storelvmo, T., & Zelinka, M. D. (2016). Observational constraints on mixed-phase clouds imply higher climate sensitivity. *Science*, *352*(6282), 224–227. https://doi.org/10.1126/science.aad5300

Taylor, K. E., Stouffer, R. J., & Meehl, G. A. (2011). An Overview of CMIP5 and the Experiment Design. *Bulletin of the American Meteorological Society*, *93*(4), 485–498. https://doi.org/10.1175/BAMS-D-11-00094.1

Tebaldi, C., & Knutti, R. (2018). Evaluating the accuracy of climate change pattern emulation for low warming targets. *Environmental Research Letters*, *13*(5), 055006. https://doi.org/10.1088/1748-9326/aabef2

Terai, C. R., Klein, S. A., & Zelinka, M. D. (2016). Constraining the low-cloud optical depth feedback at middle and high latitudes using satellite observations. *Journal of Geophysical Research: Atmospheres*, *121*(16), 9696–9716. https://doi.org/10.1002/2016JD025233

Thompson, D. W. J., & Solomon, S. (2002). Interpretation of Recent Southern Hemisphere Climate Change. *Science*, *296*(5569), 895–899. https://doi.org/10.1126/science.1069270

Thompson, D. W. J., & Wallace, J. M. (2000). Annular Modes in the Extratropical Circulation. Part I: Month-to-Month Variability. *Journal of Climate*, *13*(5), 1000–1016. https://doi.org/10.1175/1520-0442(2000)013<1000:AMITEC>2.0.CO;2

Trenberth, K. E., & Fasullo, J. T. (2010). Simulation of Present-Day and Twenty-First-Century Energy Budgets of the Southern Oceans. *Journal of Climate*, *23*(2), 440–454. https://doi.org/10.1175/2009JCLI3152.1

Tselioudis, G., Rossow, W. B., & Rind, D. (1992). Global Patterns of Cloud Optical Thickness Variation with Temperature. *Journal of Climate*, *5*(12), 1484–1495. https://doi.org/10.1175/1520-0442(1992)005<1484:GPOCOT>2.0.CO;2

Tselioudis, G., Lipat, B. R., Konsta, D., Grise, K. M., & Polvani, L. M. (2016). Midlatitude cloud shifts, their primary link to the Hadley cell, and their diverse radiative effects. *Geophysical Research Letters*, *43*(9), 4594–4601. https://doi.org/10.1002/2016GL068242

Ukkola, A. M., De Kauwe, M. G., Roderick, M. L., Abramowitz, G., & Pitman, A. J. (2020). Robust Future Changes in Meteorological Drought in CMIP6 Projections Despite Uncertainty in Precipitation. *Geophysical Research Letters*, *47*(11), e2020GL087820. https://doi.org/10.1029/2020GL087820

Vial, J., Dufresne, J.-L., & Bony, S. (2013). On the interpretation of inter-model spread in CMIP5 climate sensitivity estimates. *Climate Dynamics*, *41*(11–12), 3339–3362. https://doi.org/10.1007/s00382-013-1725-9

Voldoire, A. (2019). CNRM-CERFACS CNRM-CM6-1 model output prepared for CMIP6 ScenarioMIP [Data set]. Earth System Grid Federation. https://doi.org/10.22033/ESGF/CMIP6.1384

Volodin, E., Mortikov, E., Gritsun, A., Lykossov, V., Galin, V., Diansky, N., et al. (2019). INM INM-CM5-0 model output prepared for CMIP6 ScenarioMIP [Data set]. Earth System Grid Federation. https://doi.org/10.22033/ESGF/CMIP6.12322

Wall, C. J., Hartmann, D. L., & Ma, P.-L. (2017). Instantaneous Linkages between Clouds and Large-Scale Meteorology over the Southern Ocean in Observations and a Climate Model. *Journal of Climate*, *30*(23), 9455–9474. https://doi.org/10.1175/JCLI-D-17-0156.1

Wallace, J. M., & Gutzler, D. S. (1981). Teleconnections in the Geopotential Height Field during the Northern Hemisphere Winter. *Monthly Weather Review*, *109*(4), 784–812. https://doi.org/10.1175/1520-0493(1981)109<0784:TITGHF>2.0.CO;2

Weaver, C. P., & Ramanathan, V. (1997). Relationships between Large-Scale Vertical Velocity, Static Stability, and Cloud Radiative Forcing over Northern Hemisphere Extratropical Oceans. *Journal of Climate*, *10*(11), 2871–2887. https://doi.org/10.1175/1520-0442(1997)010<2871:RBLSVV>2.0.CO;2

Wehner, M. F. (2013). Very extreme seasonal precipitation in the NARCCAP ensemble: model performance and projections. *Climate Dynamics*, *40*(1), 59–80. https://doi.org/10.1007/s00382-012-1393-1

Wieners, K.-H., Giorgetta, M., Jungclaus, J., Reick, C., Esch, M., Bittner, M., et al. (2019). MPI-M MPIESM1.2-LR model output prepared for CMIP6 ScenarioMIP [Data set]. Earth System Grid Federation. https://doi.org/10.22033/ESGF/CMIP6.793

Wilks, D.S. (2006) Statistical Methods in the Atmospheric Sciences. 2nd Edition. London, United Kingdom: Academic Press.

Wood, R. (2012). Stratocumulus Clouds. *Monthly Weather Review*, *140*(8), 2373–2423. https://doi.org/10.1175/MWR-D-11-00121.1

Wood, R., & Bretherton, C. S. (2006). On the Relationship between Stratiform Low Cloud Cover and Lower-Tropospheric Stability. *Journal of Climate*, *19*(24), 6425–6432. https://doi.org/10.1175/JCLI3988.1

Wuebbles, D., Meehl, G., Hayhoe, K., Karl, T. R., Kunkel, K., Santer, B., et al. (2014). CMIP5 Climate Model Analyses: Climate Extremes in the United States. *Bulletin of the American Meteorological Society*, *95*(4), 571–583. https://doi.org/10.1175/BAMS-D-12-00172.1

Yin, J. H. (2005). A consistent poleward shift of the storm tracks in simulations of 21st century climate. *Geophysical Research Letters*, *32*(18), L18701. https://doi.org/10.1029/2005GL023684

Yukimoto, S., Koshiro, T., Kawai, H., Oshima, N., Yoshida, K., Urakawa, S., et al. (2019). MRI MRI-ESM2.0 model output prepared for CMIP6 ScenarioMIP [Data set]. Earth System Grid Federation. https://doi.org/10.22033/ESGF/CMIP6.638

Zappa, G. (2019). Regional Climate Impacts of Future Changes in the Mid–Latitude Atmospheric Circulation: a Storyline View. *Current Climate Change Reports*, *5*(4), 358–371. https://doi.org/10.1007/s40641-019-00146-7

Zappa, G., & Shepherd, T. G. (2017). Storylines of Atmospheric Circulation Change for European Regional Climate Impact Assessment. *Journal of Climate*, *30*(16), 6561–6577. https://doi.org/10.1175/JCLI-D-16-0807.1

Zelinka, M. D., & Hartmann, D. L. (2010). Why is longwave cloud feedback positive? *Journal of Geophysical Research: Atmospheres*, *115*(D16), D16117. https://doi.org/10.1029/2010JD013817

Zelinka, M. D., Klein, S. A., & Hartmann, D. L. (2011). Computing and Partitioning Cloud Feedbacks Using Cloud Property Histograms. Part II: Attribution to Changes in Cloud Amount, Altitude, and Optical Depth. *Journal of Climate*, *25*(11), 3736–3754. https://doi.org/10.1175/JCLI-D-11-00249.1

Zelinka, M. D., Grise, K. M., Klein, S. A., Zhou, C., DeAngelis, A. M., & Christensen, M. W. (2018). Drivers of the Low-Cloud Response to Poleward Jet Shifts in the North Pacific in Observations and Models. *Journal of Climate*, *31*(19), 7925–7947. https://doi.org/10.1175/JCLI-D-18-0114.1

Zelinka, M. D., Myers, T. A., McCoy, D. T., Po-Chedley, S., Caldwell, P. M., Ceppi, P., et al. (2020). Causes of Higher Climate Sensitivity in CMIP6 Models. *Geophysical Research Letters*, *47*(1), e2019GL085782. https://doi.org/10.1029/2019GL085782

Zhou, C., Zelinka, M. D., & Klein, S. A. (2016). Impact of decadal cloud variations on the Earth's energy budget. *Nature Geoscience*, *9*(12), 871–874. https://doi.org/10.1038/ngeo2828

Ziehn, T., Chamberlain, M., Lenton, A., Law, R., Bodman, R., Dix, M., et al. (2019). CSIRO ACCESS-ESM1.5 model output prepared for CMIP6 ScenarioMIP [Data set]. Earth System Grid Federation. https://doi.org/10.22033/ESGF/CMIP6.2291